



UNIVERSIDADE ESTADUAL DE CAMPINAS
Faculdade de Engenharia Elétrica e de Computação

Hever Alcahuaman Villanueva

Optimized Reactive Power Capability of Wind Power Plants with Tap-Changing Transformers

*Capacidade de Potência Reativa Otimizada das Usinas Eólicas
Usando Comutação de Taps dos Transformadores.*

Campinas

2020

Hever Alcahuaman Villanueva

Optimized Reactive Power Capability of Wind Power Plants with Tap-Changing Transformers

***Capacidade de Pôtença Reativa Otimizada das Usinas Eólicas
Usando Comutação de Taps dos Transformadores.***

Dissertation presented to the School of Electrical and Computer Engineering of the University of Campinas in partial fulfillment of the requirements for the degree of Master in Electric Engineering in the area of Electrical Energy.

Dissertação apresentada à Faculdade de Engenharia Elétrica e de Computação da Universidade Estadual de Campinas como parte dos requisitos exigidos para a obtenção do título de Mestre em Engenharia Elétrica, na área de Energia Elétrica

Supervisor: Prof. Dr. Daniel Dotta

Este exemplar corresponde à versão final da tese defendida pelo aluno Hever Alcahuaman Villanueva, e orientada pelo Prof. Dr. Daniel Dotta.

Campinas

2020

Ficha catalográfica
Universidade Estadual de Campinas
Biblioteca da Área de Engenharia e Arquitetura
Rose Meire da Silva - CRB 8/5974

AL16o Alcahuaman Villanueva, Hever, 1992-
Optimized reactive power capability of wind power plants with tap-changing transformers / Hever Alcahuaman Villanueva. – Campinas, SP : [s.n.], 2020.

Orientador: Daniel Dotta.
Dissertação (mestrado) – Universidade Estadual de Campinas, Faculdade de Engenharia Elétrica e de Computação.

1. Potência reativa (Engenharia elétrica). 2. Programação linear inteira mista. 3. Energia eólica. 4. Eletrônica de potência. 5. Fluxo de carga elétrica. I. Dotta, Daniel, 1978-. II. Universidade Estadual de Campinas. Faculdade de Engenharia Elétrica e de Computação. III. Título.

Informações para Biblioteca Digital

Título em outro idioma: Capacidade de potência reativa otimizada das usinas eólicas usando comutação de taps dos transformadores

Palavras-chave em inglês:

Reactive power (Electrical engineering)

Mixed-integer linear programming

Wind power

Power electronics

Electric power Flow

Área de concentração: Energia Elétrica

Titulação: Mestre em Engenharia Elétrica

Banca examinadora:

Daniel Dotta [Orientador]

Tatiana Mariano Lessa de Assis

Luís Fernando Costa Alberto

Data de defesa: 12-08-2020

Programa de Pós-Graduação: Engenharia Elétrica

Identificação e informações acadêmicas do(a) aluno(a)

- ORCID do autor: <https://orcid.org/0000-0003-3508-5369>

- Currículo Lattes do autor: <http://lattes.cnpq.br/1118639633466058>

COMISSÃO JULGADORA - TESE DE MESTRADO

Candidato(a): Hever Alcahuaman Villanueva RA: 228105

Data de defesa: 12 de agosto de 2020

Titulo da Dissertação: "Optimized Reactive Power Capability of Wind Power Plants with Tap-Changing Transformers"

"Capacidade de Pôtença Reativa Otimizada das Usinas Eólicas Usando Comutação de Taps dos Transformadores."

Prof. Dr. Daniel Dotta (Presidente)

Profa. Dra. Tatiana Mariano Lessa de Assis.

Prof. Dr. Luís Fernando Costa Alberto.

A Ata de Defesa, com as respectivas assinaturas dos membros da Comissão Julgadora, encontra-se no SIGA (Sistema de Fluxo de Dissertação/Tese) e na Secretaria de Pós-Graduação da Faculdade de Engenharia Elétrica e de Computação.

... to people who don't define failure as the opposite of success; they define failure as the opposite of trying.

Acknowledgements

First and foremost, I would like to thank God for everything, but especially for all the moments in my life and the lessons I have learned. I am extremely grateful to my mom María Elena, my dad Onésimo, and my brothers Grover, Víctor, Jeny, Jaime and Diana for their love, prayers, caring, support, and sacrifices for educating and preparing me for my future.

I would like to express my deep and sincere gratitude to my advisor, Dr. Daniel Dotta, for giving me the opportunity to allow me to be his master's student and thus fulfill my wishes to increase my knowledge on the electrical sector at one of the best universities in Brazil and in the world. My sincere gratitude to Dr. Marcos J. Rider, who along with my advisor guided me in all the time of research and writing of this thesis.

To my great friends F. Puma, C. Zevallos, P. Sovero, J.W. Cruz, R. Hernandez, S. Constante, E. Alvarez, J. Rodriguez, G. Oré, F. Liederer, G. Sanchez, L.F. Zaravia ,C. Alvarez , E. Rojas, with whom we had memorable moments.

To my dear friend S.J. Benites who, despite the distance and the different time zones, was always available to listen and advise me. I will always be grateful.

To my spoiled friends, S. Pabón and M.E. Cruz, who I consider my little sisters from other countries, thank you for your inexhaustible energy and the beautiful moments on the trips we have made.

Finally, this work was financed by the *Coordenação de Aperfeiçoamento de Pessoal de Nível Superior* - Brasil (CAPES) - Finance Code 001.

“Failure is an option here. If things are not failing, you are not innovating enough ”
(Elon Musk)

Abstract

With the recent advancements in power electronics for wind turbines, wind power plants (WPPs) have become valuable assets for reactive power support of bulk power systems. In this paper, we present a methodology to optimize the WPP's reactive power capability as seen from the point of common coupling (PCC). To this end, the proposed methodology determines the configuration of the tap-changing transformers within the WPP that maximizes the amount of reactive power the WPP can either consume or inject into the network, considering uncertain levels of wind power generation and voltage magnitude at the PCC. The optimized reactive power capability (ORPC) problem is initially formulated as a mixed-integer nonlinear programming (MINLP) model. Then, a set of efficient linearization techniques are used to obtain a mixed-integer linear programming (MILP) model that can be solved via off-the-shelf mathematical programming solvers. The results demonstrate that the proposed MILP model is a scalable, flexible and accurate method to maximize the reactive power capability of WPP as seen from the PCC.

Keywords: Reactive power capability curve, mixed-integer linear programming, optimize reactive power capability, wind power plant.

Resumo

Com os recentes avanços na eletrônica de potência para turbinas eólicas, as usinas eólicas tornaram-se ativos valiosos para o suporte de potência reativa de sistemas elétricos de potência. Neste trabalho, apresentamos uma metodologia para otimizar a capacidade de potência reativa das usinas eólicas do ponto de vista de acoplamento comum. Para esse fim, a metodologia proposta determina a configuração dos transformadores de comutação na usina eólica que maximiza a quantidade de potência reativa que a usina eólica pode consumir ou injetar na rede, considerando níveis incertos de geração de energia eólica e magnitude da tensão no ponto de acoplamento comum. O problema da capacidade de potência reativa otimizada é inicialmente formulado como um modelo de programação não linear inteiro misto. Em seguida, um conjunto de técnicas eficientes de linearização é usado para obter um modelo de programação linear inteiro misto que pode ser resolvido por meio de solucionadores de programação matemática prontos para uso. Os resultados demonstram que o modelo proposto é um método escalável, flexível e preciso para maximizar a capacidade de potência reativa da usina eólica, como visto no ponto de acoplamento comum.

Palavras-chaves: Curva de capacidade de potência reativa, programação linear inteira mista, otimização da capacidade de potência reativa, usina eólica.

List of Figures

Figure 1.1 – Wind energy installed capacity.	18
Figure 1.2 – Wind power plant topology [Source: Adapted from (Ellis; Muljadi, 2008)].	20
Figure 1.3 – a)WPP system comprises seven WT and b)RPC of the (a)	21
Figure 2.1 – Generalized model for branches in an RDN [Source: adapted from (Martin et al., 2018)].	26
Figure 2.2 – Piecewise linearization method for terms P_{ij}^2 and Q_{ij}^2	30
Figure 2.3 – 136-Bus radial distribution system layout.	34
Figure 2.4 – Absolute deviations for the 136-Bus Radial Distribution System.	35
Figure 3.1 – Schematic representation of a Type-4 WT connected to the WPP's collector grid. [Source: adapted from (Sarkar et al., 2019)]	38
Figure 3.2 – Equivalent representation of a WT feeder connected to the WPP's collector grid. [Source: adapted from (Sarkar et al., 2019)]	38
Figure 3.3 – WT power capability curve with limited voltage and current. [Source: adapted from (Sarkar et al., 2019)]	40
Figure 3.4 – Reactive power capability curves for Type-4 WT. [Source: adapted from (Sarkar et al., 2019)]	41
Figure 3.5 – A single WT representation of WPP with aggregated WPP collection system. [Source: adapted from (Sarkar et al., 2019)].	42
Figure 3.6 – Process flow diagram to determine equivalent collector system for a WPP.	43
Figure 3.7 – Flowchart to determine WPP reactive power capability using a detailed model. [Source: from (Sarkar et al., 2019)]	46
Figure 4.1 – WT power capability curve: a) voltage-limited and current-limited capability curve, b) Discrete limits for different levels of wind generation	55
Figure 4.2 – Reactive power capability - voltage at LV side WT transformer limited by voltage and current by the GSC converter.	55
Figure 4.3 – Piecewise linearization function for terms $P_{ij,c}^2$ and $Q_{ij,c}^2$	59
Figure 5.1 – Small WPP system layout with 7 WT feeders.	64
Figure 5.2 – Small WPP system RPC estimation using different methods.	65
Figure 5.3 – Small WPP system RPC using the proposed method evaluated with and without collector system bounds.	67
Figure 5.4 – Burbo Bank WPP system topology.	68
Figure 5.5 – Burbo Bank WPP system reactive power capability estimation using different methods.	69
Figure 5.6 – Burbo Bank WPP system RPC using the proposed method evaluated with and without collector system bounds.	71

Figure 5.7 – Average voltage error percentage for each test system using the detailed model.	72
Figure 5.8 – Small WPP system layout with 7 WT feeders.	76
Figure 5.9 – Small WPP system reactive power capability using the MILP model and an exact AC-PF - Base case.	76
Figure 5.10–Small WPP system reactive power capability using the MILP model and an exact AC-PF - Case I.	77
Figure 5.11–Small WPP system reactive power capability using the MILP model and an exact AC-PF - Case II.	77
Figure 5.12–Small WPP system reactive power capability obtained with the base case, Cases I and II.	78
Figure 5.13–Burbo Bank WPP system topology.	80
Figure 5.14–Burbo bank WPP system reactive power capability using the MILP model and an exact AC-PF - Base case.	81
Figure 5.15–Burbo bank WPP system reactive power capability using the MILP model and an exact AC-PF - Case I.	81
Figure 5.16–Burbo bank WPP system reactive power capability using the MILP model and an exact AC-PF - Case II.	82
Figure 5.17–Burbo bank WPP system reactive power capability obtained with the base case, Cases I and II.	83
Figure B.1 – Equivalent diagram of the collector system connected to a substation of a typical WPP. [Source: adapted from (Muljadi et al., 2006)]	99
Figure B.2 –a) single series daisy-chain b) equivalent representation of circuit (a). [Source: adapted from (Muljadi et al., 2006)]	99
Figure B.3 –a) Parallel connection of three groups of WTs through series impedance Z_1 , Z_2 , Z_3 . b) equivalent representation of circuit (a). [Source: adapted from (Muljadi et al., 2006)]	101
Figure B.4 –a) Parallel series connection of three groups of WTs. b) equivalent representation of circuit (a). [Source: adapted from (Muljadi et al., 2006)]	102
Figure B.5 –Representing the shunt line capacitance of the collector grid within the WPP. [Source: adapted from (Muljadi et al., 2006)]	104
Figure B.6 –a) WT transformer representation within the WPP, b) equivalent representation of circuit (a). [Source: adapted from (Muljadi et al., 2006)]	104

List of Tables

Table 2.1 – Results for the 136-Bus Radial Distribution System	35
Table 4.1 – Modified variables considering the set of scenarios \mathcal{K}	60
Table 4.2 – Computational complexity of the MINLP and the MILP model	61
Table 5.1 – RMSE of calculated reactive power for the small WPP system.	66
Table 5.2 – PADC of plotted reactive power capability for the small WPP system. .	66
Table 5.3 – PADC' of plotted RPC curves for the Small WPP considering collector system bounding using the proposed method.	68
Table 5.4 – RMSE of calculated reactive power for Burbo Bank WPP system. . . .	69
Table 5.5 – PADC of plotted capability curves for Burbo Bank WPP system. . . .	70
Table 5.6 – PADC of plotted RPC curves for the Burbo Bank WPP system consid- ering collector system bounding using the proposed method.	71
Table 5.7 – Time needed to solve the RPC estimation models for each test system. .	72
Table 5.8 – Methods comparison with rating	73
Table 5.9 – Accuracy assessment of the proposed MILP model for the small WPP. .	78
Table 5.10–Assessment of increased reactive power capability for the small WPP . .	79
Table 5.11–Case I/II: Tap-changer positions of the NLTC transformers for the small WPP.	79
Table 5.12–Case II: Tap-changer positions of the main transformer equipped with OLTC for the small WPP.	80
Table 5.13–Accuracy assessment of the proposed MILP model for Burbo Bank WPP.	82
Table 5.14–Assessment of increased reactive power capability for Burbo Bank WPP	83
Table 5.15–Case I/II: Tap-changer positions of the NLTC transformers for Burbo Bank WPP system.	84
Table 5.16–Case II: Tap-changer positions of the main transformer equipped with OLTC for the Burbo Bank WPP system.	84
Table A.1–Bus Data 136-Bus Radial Distribution System	92
Table A.2–Generation Data 136-Bus Radial Distribution System	94
Table A.3–Branch Data 136-Bus Radial Distribution System	94
Table C.1–Parameter of the Type-4 WT Feeder	105
Table C.2–Parameter of Main Transformer	105
Table C.3–Branch Data of the small WPP System	105
Table C.4–Branch Data of Burbo Bank WPP System	106
Table D.1–Coefficients of linear functions calculated using Taylor polynomials. . . .	107

List of abbreviations and acronyms

WPP	Wind Power Plant
WT	Wind Turbine
GSC	Grid Side Converter
MSC	Machine Side Converter
PMSG	Permanent Magnet Synchronous Generator
RDN	Radial Distribution Network
PCC	Point of Common Coupling
SE	Electrical Substation
NLTC	No-Load Tap Changer
OLTC	On-Load Tap Changer
AC	Alternating Current
AC-PF	AC-Power FLOW
AC-OPF	AC-Optimal Power Flow
LP	Linear Programming
NLP	Nonlinear Programming
MILP	Mixed-integer linear programming
MINLP	Mixed-integer nonlinear programming
RPC	Reactive Power Capability
OPRC	Optimized Reactive Power Capability
LV	Low Voltage
HV	High Voltage
RMSE	Root Mean Square Error
PADC	Percent Area Difference Comparison

V_{pcc}	Voltage magnitude at PCC bus.
$V_{\text{LV}}^{\text{SE}}$	Voltage magnitude on the low-voltage side of the main transformer
V_{LV}	Voltage magnitude on the low-voltage side of the WT transformer
STATCOM	Static Synchronous Compensator

Contents

1	INTRODUCTION	18
1.1	Motivation	18
1.2	Literature Review	19
1.3	Problem Statement	19
1.4	Objectives	21
1.5	Contributions	22
1.6	Thesis Outline	22
2	BRANCH-BASED AC OPTIMAL POWER FLOW	24
2.1	Introduction	25
2.2	AC Power Flow Representations	26
2.2.1	General Mathematical Model for Branches	26
2.2.2	General equations of the AC Power Flow Based on Branch Flow	27
2.3	AC Optimal Power Flow Formulation	28
2.3.1	AC-OPF Model Based on Branch Flow	29
2.3.2	Linearization of the AC Optimal Power Flow Based on Branch Flow	30
2.4	Validation	33
2.4.1	Accuracy Criterion	33
2.4.2	136-Bus Radial Distribution System	34
2.5	Comments and Conclusions	35
3	REACTIVE POWER CAPABILITY MODEL OF WPP	36
3.1	Introduction	37
3.2	Reactive Power Capability Model of Type-4 WT	37
3.2.1	Converter Current Limitation	38
3.2.2	Converter Voltage Limitation	39
3.3	WPP Reactive Power Capability Model	41
3.3.1	Scaled WT Model	41
3.3.2	Aggregated WPP Model	42
3.3.2.1	WPP Equivalent Impedance	42
3.3.2.2	WPP Reactive Power Capability	44
3.3.3	WPP Detailed Model	45
3.3.3.1	Algorithm proposed by Sakar et al.,2019	45
3.4	Summary	47

4	OPTIMIZED REACTIVE POWER CAPABILITY OF WIND POWER PLANT	48
4.1	Introduction	51
4.2	Optimized Reactive Power Capability as a Two-Mode Model	51
4.2.1	Formulation of the ORPC's Initial Model	52
4.2.1.1	Transformers Equipped with NLTC	53
4.2.1.2	Main Transformer Equipped with OLTC	54
4.2.1.3	Point of Common Coupling	54
4.3	Linearization of the ORPC's Initial Model	54
4.3.1	Linearization of the Type-4 WT Reactive Power Capability	54
4.3.2	Linearization of the Voltage Magnitude Regulation	56
4.3.3	Linear Approximation of the AC Power Flow	58
4.4	ORPC Model Including Specified Scenarios	59
4.4.1	Proposed MILP Model	60
4.4.1.1	Computational Complexity of the Proposed Models	61
4.4.1.2	Solution Strategy	61
4.5	Final Comments	62
5	SIMULATIONS AND RESULTS	63
5.1	Introduction	63
5.2	Real-time Operation	64
5.2.1	A Small WPP with 7 WTs	64
5.2.1.1	Performance Indexes	65
5.2.1.2	RPC with Bounding	67
5.2.2	Burbo Bank WPP	68
5.2.2.1	Performance Indexes	69
5.2.2.2	RPC with bounding	70
5.2.3	Assessment of the Computational Cost	72
5.2.4	Discussion	73
5.3	Planning Stage	74
5.3.1	Case Studies	75
5.3.2	Assessment Criterion	75
5.3.3	A Small WPP with 7 WTs	76
5.3.3.1	Accuracy Validation	78
5.3.3.2	Performance Validation	78
5.3.3.3	Obtained Tap Settings	79
5.3.4	Burbo bank WPP system	80
5.3.4.1	Accuracy Validation	82
5.3.4.2	Performance Validation	83
5.3.4.3	Obtained Tap Settings	84

5.3.5	Discussion	85
6	CONCLUSIONS AND FUTURE WORKS	86
6.1	Conclusions	86
6.2	Future Works	87
	BIBLIOGRAPHY	88
	Appendices	91
A	– ELECTRICAL DATA FROM RADIAL DISTRIBUTION SYSTEMS	92
A.1	136-Bus Radial Distribution System	92
B	– EQUIVALENT COLLECTOR SYSTEM FOR A WPP	99
B.1	First Step: <i>Connection at the trunk line level</i>	99
B.2	Second Step <i>Connection at the feeder level</i>	100
B.3	Third Step: <i>Connection to the Low-Voltage Side of the Main Trans-</i> <i>former</i>	102
B.4	Fourth Step: <i>Shunt Representation</i>	103
B.5	Fifth Step: <i>WT Transformer Representation</i>	104
C	– ELECTRICAL DATA FROM WPPS	105
C.1	General Information	105
C.2	WPP Systems Information	105
D	– TAYLOR POLYNOMIALS	107

1 Introduction

1.1 Motivation

Nowadays, the growing concern regarding fossil fuel depletion and climate change resulted in ambitious targets of renewable energy integration. Consequently, wind power capacity is continuously increasing into the power system and its contribution to the overall energy supply. Wind power generation is one of the fastest-growing renewable energy sources. Total installed wind-generation capacity onshore and offshore by 2019 was 15.36 GW and 622.7 GW in Brazil and globally respectively (IRENA, 2019). Production of wind power generation doubled between 2009 and 2013, and in 2016 wind energy accounted for 16% of the electricity generated by renewable energy sources. Fig. 1.1 shows the growth of wind energy over the last decade in Brazil and globally.

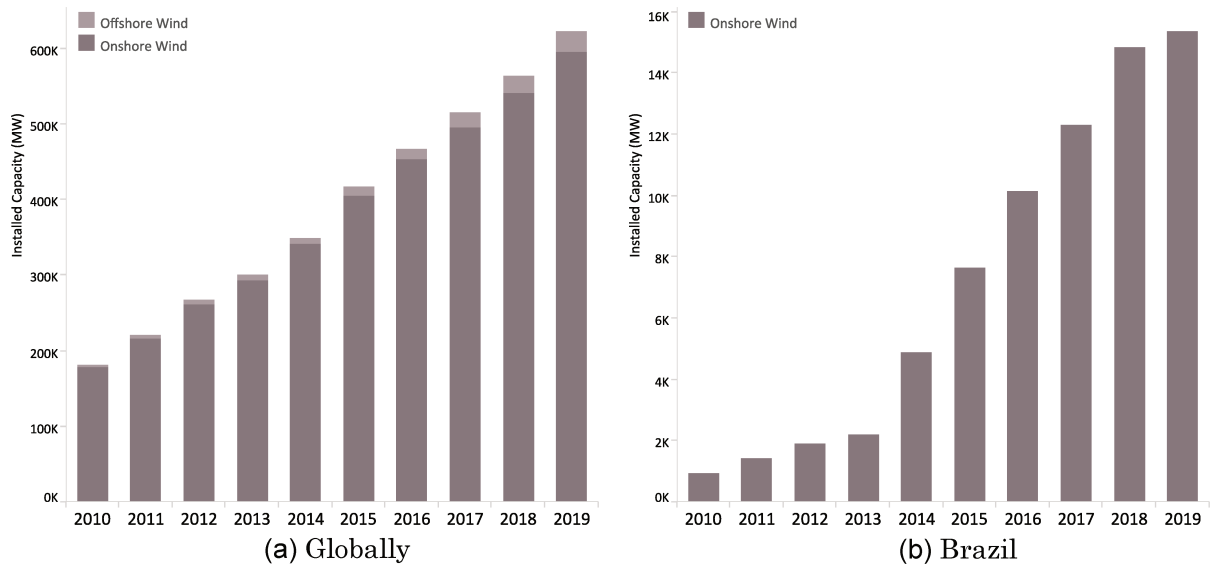


Figure 1.1 – Wind energy installed capacity.

In general, the transition to renewable energy sources integrated in the power system has resulted in the displacement of conventional sources, which have been the primary sources of reactive power/voltage control in conventional power systems. Consequently, wind generation sources are called to contribute with voltage magnitude and frequency support in order to improve power system operation. Thanks to the advances in power electronics for the development of wind turbines, the latter can provide reactive power to the network whether the turbine is producing active power or not (NERC, 2018). Yet, to correctly and safely utilize the capacity of the WPP for voltage regulation, we need to have an accurate estimation of its capability curve.

Differently from synchronous generators, the reactive power capability (RPC) of WPPs must take into account the boundaries of the power electronics converters, the topology of the collectors, and discrete variables such as tap settings and capacitor banks. The correct representation and setting of these parameters have a direct effect on the capacity of the WPP to provide reactive power. It should also be noted that depending on the size of the WPP and the stiffness of the external system, the WPP cannot control the voltage at the PCC bus. In this situation, the WPP can operate with a constant power factor and their capacity of contribution in reactive power is also directly related to the size of the RPC.

1.2 Literature Review

The first articles that addressed the advantages of having reactive power control in WPP used proportional and mathematical optimization techniques to dispatch reactive power from double fed induction machines (DFIM) (Tapia; Tapia; Ostolaza, 2004; de Almeida; Castronuovo; Lopes, 2006; Martinez et al., 2011; Kanna; Singh, 2015). These methods, however, do not optimize the overall reactive power capability of the WPP and they are based on the output power requested by the system operator. Active power losses at the AC network that interconnects the WTs within the WPP can be minimized by controlling the reactive power of the turbines and volt/var devices, such as tap-changing transformers and shunt capacitor banks (ZHANG et al., 2017; Zhang et al., 2016). From the perspective of the WPP owner, minimizing internal losses might be of interest (Martin et al., 2018). However, from the perspective of bulk power systems, WPPs could become valuable assets for reactive power support and long-term voltage stability if WPPs' capability curves are maximized (Camm et al., 2009; Martínez et al., 2011; Sarkar et al., 2019). WPPs capabilities have been calculated by scaling the WT models as in (Konopinski; Vijayan; Ajjarapu, 2009) and (Meegahapola; Littler; Pereraa, 2013), disregarding the internal AC network of the WPP. Detailed models considering GSC parameters and the internal AC network have been developed in (Ullah; Bhattacharya; Thiringer, 2009; Kim et al., 2016; Karbouj; Rather, 2018). The aforementioned methods are not evaluated as optimization problems and they do not include discrete controllers, such as tap-changing transformers and capacitor banks. Furthermore, these methods are restricted to real-time operation and do not take into account different scenarios of wind power generation.

1.3 Problem Statement

Wind power plants (WPPs) are comprised of tens or even hundreds of wind turbines (WTs) that are often interconnected with each other by a medium-voltage collector system, also called a collecting network. Modern utility-scale WTs have nameplate ratings

ranging from 1 MW to 4 MW with terminal voltage of 600 Volts. Step-up transformers or WT transformers allow the connection between the WT terminals and the collecting network operating at 12 kV to 34.5 kV.

The collector system consists of one or several feeders connected together at a collector system station, thus allowing the active and reactive power generation to be channeled to the WPP's collector system station. Unless the collector system station is adjacent to the point of common coupling (PCC), an interconnection transmission line is needed. Reactive compensation devices such as STATCOM or Static Var Systems (SVS) may be installed at the collector system station. The amount and nature of reactive compensation is driven by interconnection requirements and collector system design considerations, including voltage regulation and losses. Fig. 1.2 shows a typical WPP topology

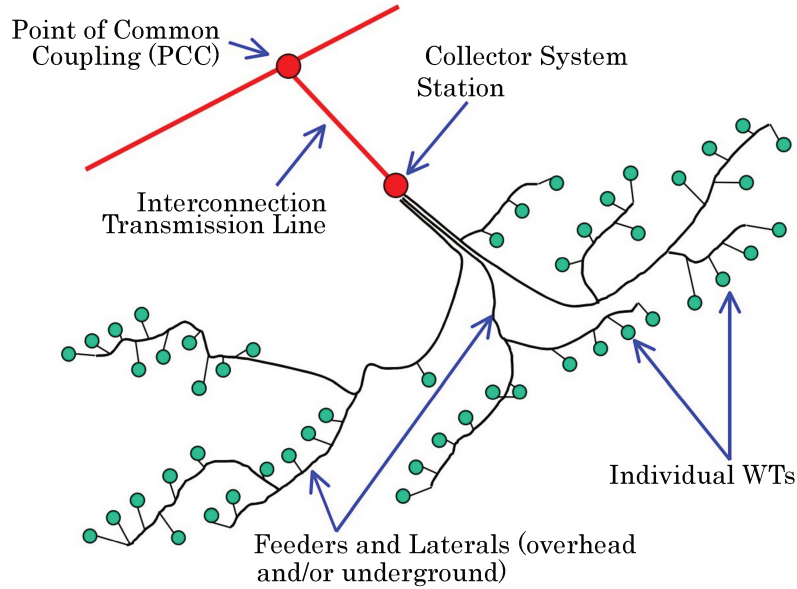


Figure 1.2 – Wind power plant topology [Source: Adapted from (Ellis; Muljadi, 2008)].

The reactive power capability of a WPP, like any other conventional generation power plant, is defined by boundaries within which the power plant can operate safely (Kundur et al., 2004). However, determining the RPC curves in a WPP is challenging because WPPs are composed by WTs scattered in a collecting network. This means that the active and reactive losses due to the collecting network as well as the limits of the electrical devices must be considered. It also should be noted that the majority of transformers in a WPP are no-load tap changers (NLTC). Thus, tap settings cannot be changed in real-time operations. As a result, they must be defined during the planning stage in order to improve the reactive power capability curve.

One dimension of the complexity of this problem is given by the number of possible combinations to find the appropriate values for the discrete variables such as the taps of the transformers. For instance, consider the WPP system illustrated in Fig. 1.3 a,

which is composed by seven WT transformers and one main transformer to connect to the PCC. All the transformers allow five tap-change positions (steps). The level of complexity considering all transformers can be expressed by:

$$\text{Complexity: } N_{\text{step}}^{N_{\text{Transformer}}} = (5)^8 = 390,625 \text{ tapping settings}$$

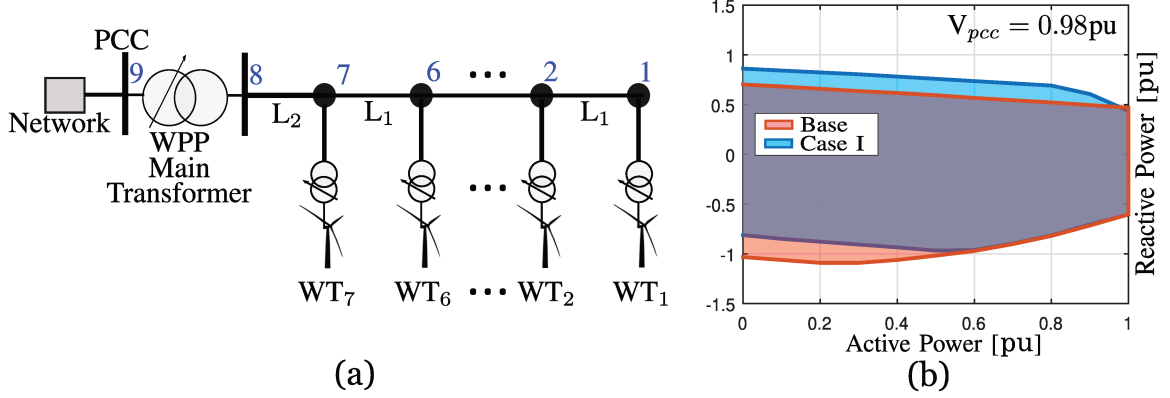


Figure 1.3 – a)WPP system comprises seven WT and b)RPC of the (a)

The effect of the optimal tap setting is shown in Fig. 1.3 b when the voltage at the PCC is equal to 0.98 pu. The red filled curve represents the RPC with a default configuration of the tap-changer, i.e. tap-changer located at position zero (all transformers), the blue filled curve represents the RPC for an specified optimal combination of tap setting. It is clear the improvement in reactive power capability for this particular operating condition. This improvement justifies the importance to correctly specify an optimal tap setting for WPPs.

In the planning stage, the complexity of this problem is hardly increased because we need to take into account the uncertainty related to the wind power generation level at WTs, voltage magnitude level at the PCC and operation mode of the WPP (injection and absorption). As a result, we need to find the optimal combination of 390,625 tapping settings for the different specified scenarios (wind power generation level at WTs, voltage magnitude level at PCC node and operation mode).

Nowadays, in practical studies, this problem is addressed running several power flow cases considering different specified scenarios in order to obtain the optimal tap setting for these conditions. This process results in a hard computational burden, as well as a considerable time spending.

1.4 Objectives

The dissertation's main goal is to propose a methodology to optimize the discrete parameters (taps and capacitor banks) in order to enhance the WPP's reactive power curve. To reach this goal, the following partial objectives are proposed:

- To develop a suitable mathematical model to represent the converter capacity of the wind turbines and the collector network, including the tap-changer and capacitor banks of a Type-4 WT based WPP.
- To explore the linear approximation approach in order to obtain reactive power capability curves in a Type-4 based WPP for real-time operation, considering the collecting system limits and the grid-side-converter limits of the WTs.
- To formulate a method to solve optimized reactive power capability (ORPC) problems in a Type-4 based WPP based on a MILP model, considering discrete controls such as tap-changers, capacitor banks, and different uncertain scenarios (wind power generation and voltage at PCC), to be compared later with the classical methods.

1.5 Contributions

The main contributions of this thesis are explicitly as follow:

1. A new linearization of Type-4 WT reactive power capability curves, considering different scenarios of wind power generation and voltage magnitude at the PCC.
2. A novel, scalable, flexible, and accurate method to solve the RPC problem, with a low computational burden for large WPPs.
3. A novel scalable, flexible and accurate MILP model for solving the ORPC problem, considering NLTC/OLTC transformers and shunt capacitor banks, scenarios, probability of each scenario, operation mode, electrical and operation limits, all in a unique integrated proposed MILP model.

1.6 Thesis Outline

The outline of this thesis is as follows:

In Chapter 2: a review of the AC power flow (AC-PF) formulations is presented in order to show the building of the nonlinear programming (NLP) model of the AC optimal power flow (AC-OPF) based on the Branch Flow model for radial distribution network (RDN) from the mathematical model of the components until their respective NLP model. Subsequently, the linear programming (LP) model of the original NLP model is developed via linearization and approximation techniques.

In Chapter 3: A review of the methods found in the literature to estimate the reactive power capability (RPC) of WPPs are presented in order to show the state of art.

In Chapter 4: The formulation of the proposed MILP model to solve optimized reactive power capability (ORPC) of a Type-4 based WPP is presented in order to show the simplification strategies via linearization and approximation techniques, as seen in the development of the AC optimal power flow based on a Branch Flow model.

In Chapter 5: Simulations and results are presented. The simulations are focused on two aspects: real-time operation and planning stage. Both approaches are validated using two WPP test systems in order to prove the efficiency, accuracy, and performance of the proposed methodology.

Finally, conclusions and future works are addressed in *Chapter 6*.

2 Branch-based AC Optimal Power Flow

Notation

Sets:

\mathcal{B}	Set of nodes (Buses)
\mathcal{L}	Set of circuit (Branches) where $\mathcal{L} \subseteq \mathcal{B} \times \mathcal{B}$

Indexes:

i	Node (Bus "From") $i \in \mathcal{B}$
j	Node (Bus "To") $j \in \mathcal{B}$
ij	Circuit (Branch) $ij \in \mathcal{L}$

Parameters:

B_i^{sh}	Shunt susceptance at bus i
P_i^{g0}	Initial active power generation at bus i
V_i^{g}	Reference voltage magnitude at bus i
B_{ij}^{sh}	Susceptance of branch ij
a_{ij}	Rate of transformer of branch ij
$\bar{I}_{ij}, \bar{S}_{ij}$	Maximum current magnitude and capacity of branch ij .
$m_{ij,y}^s$	Slope of the y^{th} linearization block, for each branch ij and block y .
P_i^d, Q_i^d	Active and reactive power demand at bus i
R_{ij}, X_{ij}	Resistance and reactance of branch ij
Z_{ij}, Y_{ij}	Impedance and Admittance of branch ij
$\underline{V}_i, \bar{V}_i$	Minimum and maximum voltage magnitude at bus i
$\underline{P}_i^g, \bar{P}_i^g$	Minimum and maximum active generation at bus i
$\underline{Q}_i^g, \bar{Q}_i^g$	Minimum and maximum reactive generation at bus i
Y	Number of linearization blocks.
Δ_{ij}^S	Upper limit of each linearization block.

Continuous variables:

$I_{ij}, I_{ij}^{\text{sqr}}$	Magnitude and square value of the current at branch ij .
P_{ij}, Q_{ij}	Active and reactive power flow in the branch ij .
P_i^g, Q_i^g	Active and reactive power generated at node i .
P_{ij}^+, P_{ij}^-	Auxiliary non-negative variable for the linearization of $ P_{ij} $.
Q_{ij}^+, Q_{ij}^-	Auxiliary non-negative variable for the linearization of $ Q_{ij} $.
V_i, V_i^{sqr}	Magnitude and square value of the voltage at bus i .
$\Delta_{ij,y}^P, \Delta_{ij,y}^Q$	Value of the y^{th} linearization block for the active and reactive power flow at branch ij .

2.1 Introduction

The problem in obtaining the optimal parameters of the reactive power capability curve of a WPP can be formulated as an optimal power flow problem. The topology of the collector system is radial as a distribution network system channeling the generation of active and reactive power to the transmission network. Specifically, RDN systems have particular characteristics in relation to high-voltage networks: they present a radial topology, a high relationship between R/X of the branches, which means that there is only one route through the network between the power flow supply source and the consumption nodes of each feeder, i.e. there are no closed routes or loops. This radial characteristic can be explored in the AC-OPF formulation by the branch-flow model that does not explicit use the bus angles variables.

The aim of this chapter is to revise the main concepts involved in the mathematical formulation of the nonlinear branch-flow method to solve the classical OPF problem using non-linear programming (NLP). To reach this goal, the mathematical model of the components of the RDN system such as the transmission lines and transformers will be described. Additionally, linear approximation techniques are presented transforming the NLP problem into a linear programming problem (LP). This linear approximation can find a solution close to the original nonlinear formulation with a less expensive computational burden. To illustrate the performance of the LP approach, a conventional optimal power flow problem (reduction of active power losses) is solved and the results are compared to NLP.

The rest of the chapter is organized as follows: Section 2.2 describes the modeling and formulation of the AC-Power flow. Section 2.3 describes the formulation of the NLP and LP AC-Optimal power flow. Section 2.4 presents the validation of the LP versus NLP model. Finally, Section 2.5 contains the conclusions of the chapter.

2.2 AC Power Flow Representations

The AC power flow (AC-PF) for an RDN system is represented by a set of non-linear equations. The mathematical models of the transmission lines and the transformers are developed to obtain the AC-PF equations. For the AC-PF of an RDN, the following hypotheses are considered (GONÇALVES, 2013; Martin et al., 2018):

- A RDN is balanced, then it can be represented by a single-phase equivalent.
- Active and reactive loads are modeled as constant power.
- It includes a main transformer for the connection between the transmission system and the distribution system
- The susceptance of the branch (B_{ij}^{sh}) is not neglected.

2.2.1 General Mathematical Model for Branches

In this thesis, the collection network is modeled including charging capacitance. Therefore, it is possible to present a generalized scheme for branches in an RDN based on the extended Branch Flow model proposed by (Martin et al., 2018) as shown in the Fig. 2.1. Note that the model considers the variables as voltages (\vec{V}_i, \vec{V}_j) represented in polar form ($\vec{V}_i = V_i \cos(\theta_i) + jV_i \sin(\theta_i)$), current (\vec{I}_{ij}) and three invariant parameters of the transmission line: series resistance R_{ij} , series reactance X_{ij} , and a shunt susceptance B_{ij}^{sh} of the branch ij .

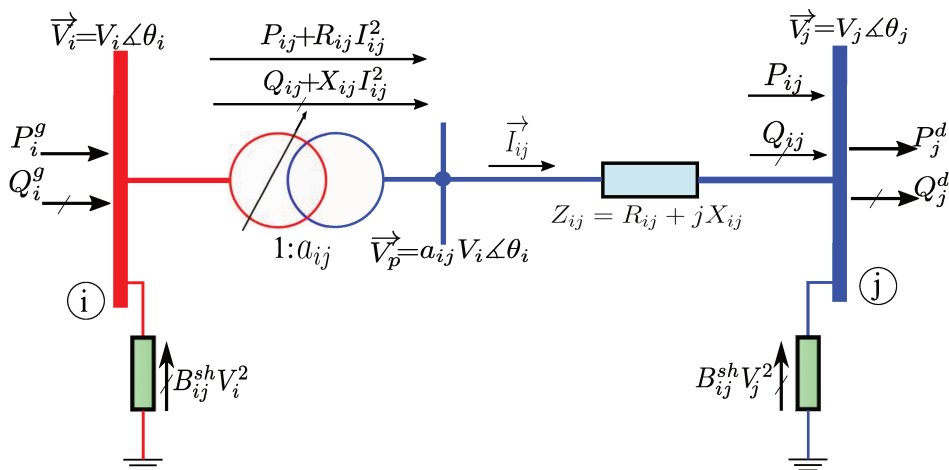


Figure 2.1 – Generalized model for branches in an RDN [Source: adapted from (Martin et al., 2018)].

The voltage drop and the current \vec{I}_{ij} in transmission line are represented by:

$$a_{ij} \vec{V}_i - \vec{V}_j = \vec{I}_{ij} (R_{ij} + jX_{ij}) \quad (2.1)$$

$$\vec{I}_{ij} = \left(\frac{P_{ij} + jQ_{ij}}{\vec{V}_j} \right)^* \quad (2.2)$$

Substituting equation (2.2) in (2.1) we have:

$$(a_{ij}\vec{V}_i - \vec{V}_j) \vec{V}_j^* = (P_{ij} - jQ_{ij})(R_{ij} + jX_{ij}) \quad (2.3)$$

Written the equation (2.3) in a rectangular form:

$$a_{ij}V_iV_j(\cos(\theta_i - \theta_j) + j\sin(\theta_i - \theta_j)) - V_j^2 = (P_{ij} - jQ_{ij})(R_{ij} + jX_{ij}) \quad (2.4)$$

Separating the Equation (2.4) in real and imaginary expressions, we have:

$$a_{ij}V_iV_j\cos(\theta_i - \theta_j) = V_j^2 + (R_{ij}P_{ij} + X_{ij}Q_{ij}) \quad (2.5)$$

$$a_{ij}V_iV_j\sin(\theta_i - \theta_j) = X_{ij}P_{ij} - R_{ij}Q_{ij} \quad (2.6)$$

Adding the squares of (2.5) and (2.6), and using the trigonometric relationships, the following is obtained:

$$a_{ij}^2V_i^2 - 2(R_{ij}P_{ij} + X_{ij}Q_{ij}) - Z_{ij}^2I_{ij}^2 - V_j^2 = 0 \quad (2.7)$$

Where I_{ij}^2 is calculated from Equation (2.2), denoted by:

$$I_{ij}^2 = \frac{P_{ij}^2 + Q_{ij}^2}{V_j^2} \quad (2.8)$$

2.2.2 General equations of the AC Power Flow Based on Branch Flow

The branch-based AC-PF must present a power balance in each node, also known as Kirchhoff's first law. In this way, Equations (2.9) and (2.10) are used to represent the active and reactive power balances, respectively in all nodes of the set \mathcal{B} .

$$P_i^g - P_i^d + \sum_{ji \in \mathcal{L}} P_{ji} - \sum_{ij \in \mathcal{L}} (P_{ij} + R_{ij}I_{ij}^2) = 0 \quad \forall i \in \mathcal{B} \quad (2.9)$$

$$Q_i^g - Q_i^d + \sum_{ji \in \mathcal{L}} (Q_{ji} + B_{ji}^{sh}V_i^2) - \sum_{ij \in \mathcal{L}} (Q_{ij} - B_{ij}^{sh}V_i^2 + X_{ij}I_{ij}^2) + B_i^{sh}V_i^2 = 0 \quad \forall i \in \mathcal{B} \quad (2.10)$$

In addition, the equations for calculating the voltage drop and current magnitude must be evaluated in all branches of the set \mathcal{L} , as shown in Equations (2.11) and (2.12).

$$a_{ij}^2V_i^2 - 2(R_{ij}P_{ij} + X_{ij}Q_{ij}) - Z_{ij}^2I_{ij}^2 - V_j^2 = 0 \quad \forall ij \in \mathcal{L} \quad (2.11)$$

$$V_j^2I_{ij}^2 = P_{ij}^2 + Q_{ij}^2 \quad \forall ij \in \mathcal{L} \quad (2.12)$$

where, Equation (2.11) represents the general voltage drop at branch ij , the value of a_{ij} is equal to 1 when it comes to branches of the RDN, if it is a transformer branch, the

value of a_{ij} depends on the voltage transformation ratio and Equation (2.12) represents the current magnitude calculation at branch ij .

Finally, the Equations (2.13) and (2.14) ensure that the voltage magnitude is constant in PV and Swing Buses as well as the active power is constant for PV buses. Additionally, the node type at bus i is represented by \mathcal{B}_i^T , taking the values of 0, 2 and 3 for PQ, PV and reference bus, respectively.

$$P_i^g = P_i^{g0} \quad \forall i \in \mathcal{B} | \mathcal{B}_i^T = 2 \quad (2.13)$$

$$V_i = V_i^g \quad \forall i \in \mathcal{B} | \mathcal{B}_i^T \neq 0 \quad (2.14)$$

By using iterative methods to solve non-linear systems, such as the Newton-Raphson method, it is possible to obtain the solution of the system of the set of equations formed by expressions (2.9)–(2.14). The solution of this non-linear system determines an unrestricted operating point, commonly called the AC-PF solution, for RDN systems. It is possible to highlight the simplicity of the mathematical formulation based on the Branch Flow model, thus facilitating the construction of the mathematical models that allow optimization problems to be represented in RDN systems.

2.3 AC Optimal Power Flow Formulation

The AC optimal power flow (AC-OPF), as the name implies, combines a specific optimization problem with power flow. Hence, this optimization problem and the power flow are solved simultaneously. The AC-OPF problem can be formulated as:

$$\begin{aligned} & \text{Minimize}_{u,x} && f(x, u) \\ & \text{subject to} && h(x, u) = 0 \\ & && g(x, u) \geq 0 \end{aligned}$$

Where u is the set of decision variables, x the set of dependent variables, f the scalar objective function, h the set of equations for AC-FP of an RDN, and g the set of operational and physical constraints. In practice, the formulation difficulty depends on the type of specific optimization problem to be treated.

The formulation of the AC-PF mentioned in subsection 2.2.2 will be used to obtain the AC-OPF formulation to solve the classical problem, whose application is focused on reducing ohmic losses in an RDN system. This problem has already been dealt with in different research works (GONÇALVES, 2013; DELGADO, 2015), addressing non-linear and linear formulation, obtaining results with good precision using linearization techniques proposed by the mentioned authors. This section aims to present the mathematical formulation describing the approximation and linearization techniques.

2.3.1 AC-OPF Model Based on Branch Flow

The following expressions (2.15)–(2.24) represent the non-linear programming (NLP) model to solve the AC-OPF problem:

Function objective:

$$\min \sum_{ij \in \mathcal{L}} R_{ij} I_{ij}^2 \quad (2.15)$$

Subject to:

$$P_i^g - P_i^d + \sum_{ji \in \mathcal{L}} P_{ji} - \sum_{ij \in \mathcal{L}} (P_{ij} + R_{ij} I_{ij}^2) = 0 \quad \forall i \in \mathcal{B} \quad (2.16)$$

$$Q_i^g - Q_i^d + \sum_{ji \in \mathcal{L}} (Q_{ji} + B_{ji}^{shl} V_i^2) - \sum_{ij \in \mathcal{L}} (Q_{ij} - B_{ij}^{shl} V_i^2 + X_{ij} I_{ij}^2) + B_i^{sh} V_i^2 = 0 \quad \forall i \in \mathcal{B} \quad (2.17)$$

$$a_{ij}^2 V_i^2 - 2(R_{ij} P_{ij} + X_{ij} Q_{ij}) - Z_{ij}^2 I_{ij}^2 - V_j^2 = 0 \quad \forall ij \in \mathcal{L} \quad (2.18)$$

$$V_j^2 I_{ij}^2 = P_{ij}^2 + Q_{ij}^2 \quad \forall ij \in \mathcal{L} \quad (2.19)$$

$$\underline{P}_i^g \leq P_i^g \leq \overline{P}_i^g \quad \forall i \in \mathcal{B} | \mathcal{B}_i^T = 2 \quad (2.20)$$

$$\underline{Q}_i^g \leq Q_i^g \leq \overline{Q}_i^g \quad \forall i \in \mathcal{B} | \mathcal{B}_i^T = 2 \quad (2.21)$$

$$\underline{V}_i^2 \leq V_i^2 \leq \overline{V}_i^2 \quad \forall i \in \mathcal{B} | \mathcal{B}_i^T = 2 \quad (2.22)$$

$$V_i^2 = (V^{nom})^2 \quad \forall i \in \mathcal{B} | \mathcal{B}_i^T = 3 \quad (2.23)$$

$$0 \leq I_{ij}^2 \leq \overline{S}_{ij}^2 / V_j^2 \quad \forall ij \in \mathcal{L} \quad (2.24)$$

The objective function in (2.15) is to minimize the ohmic losses in the branches. For this OPF problem, we assume that there is no control of the bus voltage of the electrical substation, i.e., on the reference bus ($\mathcal{B}_i^T = 3$). Then, the voltage magnitude on the reference bus is considered to be equal to the nominal voltage (V^{nom}), as shown in constraint (2.23). The constraints (2.16) and (2.17) represent the balance of active and reactive power at bus i respectively. The constraint (2.18) represents the general voltage drop at branch ij , where the value of a_{ij} is equal to 1 when it comes to branches of the RDN, and, when it is a transformer branch, the value of a_{ij} depends on the voltage transformer ratio. Constraint (2.12) represents the current magnitude calculation at branch ij . Constraint (2.20)–(2.22) represents the operational limits at generators ($\mathcal{B}_i^T = 2$), and constraint (2.24) represents the loadability limits of the branches in the RDN system.

Note that the formulation for this optimization problem is non-convex and difficult to solve analytically. Besides, the number of equations and the number of variables are not equal, hence there will be no single solution. On the contrary, there will be one or more local solutions, without guaranteeing the optimal global solution. This AC-OPF formulation

can be adequately solved by solvers such as IPOPT (Yoshiaki Kawajir, 2015) or KNITRO (BYRD; NOCEDAL; WALTZ, 2006) in mathematical modeling languages such as AMPL (R. Fourer and D. M. Gay and B. W. Kernighan, 2003) or JuMP (KWON, 2016).

In order to avoid the uncertainty in obtaining the optimal global solution in non-linear formulations, the original formulation must be conveniently transformed using relaxation, approximation, or linearization methodologies, thus guaranteeing an optimal global solution for this new formulation, being this very close to the solution of the original one. In the following subsection, some approximation techniques will be applied to the classical OPF problem, being very useful for the development of this dissertation.

2.3.2 Linearization of the AC Optimal Power Flow Based on Branch Flow

Conveniently, it is possible to make a variable change from the quadratic magnitudes of current and voltage (I_{ij}^2 , V_i^2) shown in Equations (2.15)–(2.24) to linear variables, as shown below:

$$I_{ij}^2 = I_{ij}^{\text{sqr}} \quad \text{and} \quad V_i^2 = V_i^{\text{sqr}}$$

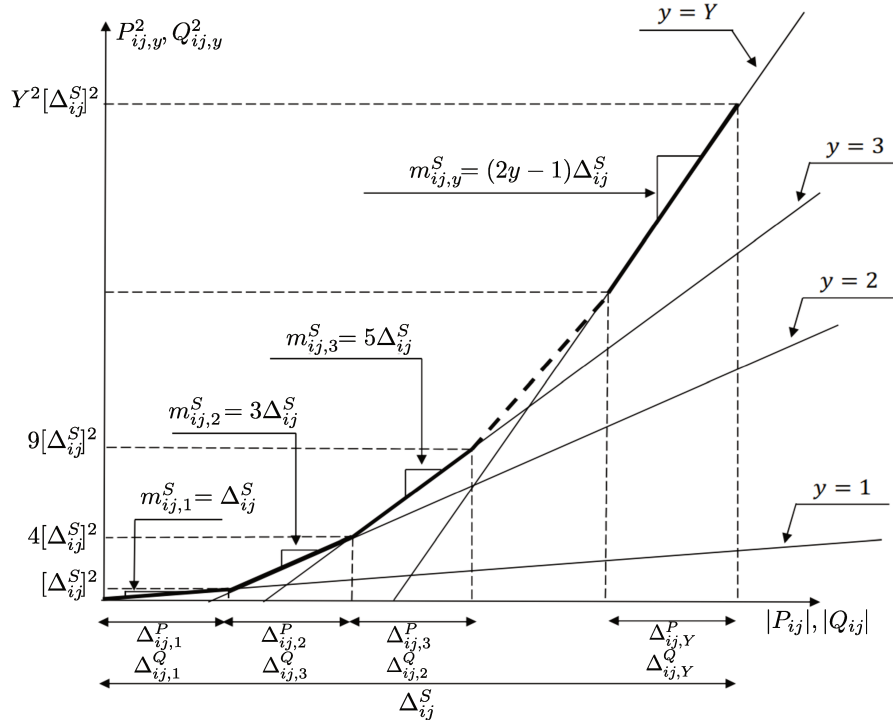


Figure 2.2 – Piecewise linearization method for terms P_{ij}^2 and Q_{ij}^2 .

The constraint (2.19) is of a non-linear nature, the left expression is a product of two decision variables ($V_j^2 I_{ij}^2$), this can be linearized considering the magnitude of nominal voltage (V^{nom}) and variable change, obtaining the following expression:

$$V_j^2 I_{ij}^2 \approx (V^{nom})^2 I_{ij}^{\text{sqr}} \quad (2.25)$$

Continuing with constraint (2.19), the right expression represents a non-linear equation of squared variables ($P_{ij,c}^2$ and $Q_{ij,c}^2$). This can be linearized by the method of piecewise linearization (Lin et al., 2013), which needs auxiliary variables to achieve discretization in blocks, shown in (2.26)–(2.33). Where $\Delta_{ij}^S = \bar{S}_{ij}/Y$ and $m_{ij,y}^s = (2y-1)\Delta_{ij}^S$. The piecewise linearization of the terms P_{ij}^2 and Q_{ij}^2 is illustrated in Fig. 2.2.

$$P_{ij}^2 + Q_{ij}^2 \approx \sum_{y=1}^Y m_{ij,y}^s \Delta_{ij,y}^P + \sum_{y=1}^Y m_{ij,y}^s \Delta_{ij,y}^Q \quad \forall ij \in \mathcal{L} \quad (2.26)$$

$$P_{ij}^+ - P_{ij}^- = P_{ij} \quad \forall ij \in \mathcal{L} \quad (2.27)$$

$$P_{ij}^+ + P_{ij}^- = \sum_{y=1}^Y \Delta_{ij,y}^P \quad \forall ij \in \mathcal{L} \quad (2.28)$$

$$Q_{ij}^+ - Q_{ij}^- = Q_{ij} \quad \forall ij \in \mathcal{L} \quad (2.29)$$

$$Q_{ij}^+ + Q_{ij}^- = \sum_{y=1}^Y \Delta_{ij,y}^Q \quad \forall ij \in \mathcal{L} \quad (2.30)$$

$$P_{ij}^+, P_{ij}^-, Q_{ij}^+, Q_{ij}^- \geq 0 \quad \forall ij \in \mathcal{L} \quad (2.31)$$

$$0 \leq \Delta_{ij,y}^P \leq \Delta_{ij}^S \quad \forall ij \in \mathcal{L}, y \in \{1 \dots Y\} \quad (2.32)$$

$$0 \leq \Delta_{ij,y}^Q \leq \Delta_{ij}^S \quad \forall ij \in \mathcal{L}, y \in \{1 \dots Y\} \quad (2.33)$$

Finally, the constraint (2.24) can be approximated by a linear expression considering the magnitude of nominal voltage (V^{nom}) and change of variable, thus obtaining the maximum current limit for the branches $\bar{S}_{ij}/V^{nom} = \bar{I}_{ij}^2$. Obtaining the following linear inequality:

$$0 \leq I_{ij}^{sqr} \leq \bar{I}_{ij}^2 \quad (2.34)$$

Hence, the following expressions (2.35)–(2.51) represent the linear programming (LP) model to solve the AC-OPF problem:

Function objective:

$$\min \sum_{ij \in \mathcal{L}} R_{ij} I_{ij}^{sqr} \quad (2.35)$$

Subject to:

$$P_i^g - P_i^d + \sum_{ji \in \mathcal{L}} P_{ji} - \sum_{ij \in \mathcal{L}} (P_{ij} + R_{ij} I_{ij}^{sqr}) = 0 \quad \forall i \in \mathcal{B} \quad (2.36)$$

$$Q_i^g - Q_i^d + \sum_{ji \in \mathcal{L}} (Q_{ji} + B_{ji}^{shl} V_i^{sqr}) - \sum_{ij \in \mathcal{L}} (Q_{ij} - B_{ij}^{shl} V_i^{sqr} + X_{ij} I_{ij}^{sqr}) + B_i^{sh} V_i^{sqr} = 0 \quad \forall i \in \mathcal{B} \quad (2.37)$$

$$a_{ij}^2 V_i^{sqr} - 2(R_{ij} P_{ij} + X_{ij} Q_{ij}) - Z_{ij}^2 I_{ij}^{sqr} - V_j^{sqr} = 0 \quad \forall ij \in \mathcal{L} \quad (2.38)$$

$$(V^{nom})^2 I_{ij}^{sqr} = \sum_{y=1}^Y m_{ij,y}^s \Delta_{ij,y}^P + \sum_{y=1}^Y m_{ij,y}^s \Delta_{ij,y}^Q \quad \forall ij \in \mathcal{L} \quad (2.39)$$

$$P_{ij}^+ - P_{ij}^- = P_{ij} \quad \forall ij \in \mathcal{L} \quad (2.40)$$

$$P_{ij}^+ + P_{ij}^- = \sum_{y=1}^Y \Delta_{ij,y}^P \quad \forall ij \in \mathcal{L} \quad (2.41)$$

$$Q_{ij}^+ - Q_{ij}^- = Q_{ij} \quad \forall ij \in \mathcal{L} \quad (2.42)$$

$$Q_{ij}^+ + Q_{ij}^- = \sum_{y=1}^Y \Delta_{ij,y}^Q \quad \forall ij \in \mathcal{L} \quad (2.43)$$

$$P_{ij}^+, P_{ij}^-, Q_{ij}^+, Q_{ij}^- \geq 0 \quad \forall ij \in \mathcal{L} \quad (2.44)$$

$$0 \leq \Delta_{ij,y}^P \leq \Delta_{ij}^S \quad \forall ij \in \mathcal{L}, y \in \{1 \dots Y\} \quad (2.45)$$

$$0 \leq \Delta_{ij,y}^Q \leq \Delta_{ij}^S \quad \forall ij \in \mathcal{L}, y \in \{1 \dots Y\} \quad (2.46)$$

$$\underline{P}_i^g \leq P_i^g \leq \overline{P}_i^g \quad \forall i \in \mathcal{B} | \mathcal{B}_i^T = 2 \quad (2.47)$$

$$\underline{Q}_i^g \leq Q_i^g \leq \overline{Q}_i^g \quad \forall i \in \mathcal{B} | \mathcal{B}_i^T = 2 \quad (2.48)$$

$$\underline{V}_i^2 \leq V_i^{sqr} \leq \overline{V}_i^2 \quad \forall i \in \mathcal{B} | \mathcal{B}_i^T = 2 \quad (2.49)$$

$$0 \leq I_{ij}^{sqr} \leq \overline{I}_{ij}^2 \quad \forall ij \in \mathcal{L} \quad (2.50)$$

$$V_i^{sqr} = (V^{nom})^2 \quad \forall i \in \mathcal{B} | \mathcal{B}_i^T = 3 \quad (2.51)$$

The above formulation is a linear approximation (LP) to solve the AC-OPF problem for an RDN posed in Section 2.3, where the objective function (2.35) is representing ohmic losses in the branches, constraint (2.36) and (2.37) represent the active and reactive power balances at bus i in the system respectively, constraint (2.38) represents the voltage drop at branch ij , constraints (2.39)–(2.46) represent the approximate calculation of current magnitude at branch ij expressed in a linear equation. Constraint (2.47)–(2.50) represents the operational and electrical limits of the RDN system, such as the active and reactive power generation limits of the generators (PV buses) at bus i respectively, the voltage limits at bus i , the loadability limits at branch ij , respectively.

Note that the linear formulation for this optimization problem is convex, thus guaranteeing the optimal solution. This linear formulation AC-OPF, can be adequately solved by solvers such as CPLEX (IBM ILOG, 2009) or IPOPT (Yoshiaki Kawajir, 2015) mathematical modeling languages such as AMPL (R. Fourer and D. M. Gay and B. W. Kernighan, 2003) or JuMP (KWON, 2016).

In the following section, the validation of the linear versus non-linear formulation of the classical OPF problem will be carried out. The difference can be quantified by an accuracy criterion. It is worth mentioning that this is a classic optimization problem addressed by different research papers, and that it is used to validate the different relaxation, approximation, and linearization methodologies.

2.4 Validation

This section presents the comparisons of the results obtained from the AC-OPF problem seen in subsection 2.3.1 being evaluated with the NLP model and the LP model. In order to obtain the precision of the linearization techniques developed in section 2.3.2, considering a number of steps for the LP model of $Y = 50$. The system used has 136 buses and was obtained from (DELGADO, 2015). The electrical data are presented in Appendix A. The models were implemented in Julia Language (version 1.4.0) using its optimization package JuMP (version 0.19) (KWON, 2016), where the formulation of the NLP model was solved with the non-commercial solver IPOPT (version 8.1.0.56, with default settings) (Yoshiaki Kawajir, 2015). And, the formulation of the LP model was solved with the commercial solver CPLEX (version 12.8.0, with default settings) (IBM ILOG, 2009). The simulations were done in a notebook with a 2.20 GHz Intel Core i7-2670 processor and 8 GB of RAM.

2.4.1 Accuracy Criterion

In order to evaluate the precision of the results by the adopted methodology, the accuracy criterion $\xi_V^{(\%)}$ and $\xi_I^{(\%)}$ defined by the expressions (2.52) and (2.53) will be used in this chapter, calculating the percentage of absolute difference of voltage magnitude at node i and current magnitude at branches ij respectively.

$$\xi_V^{(\%)} = \left| \frac{V_i^{\text{NLP}} - V_i^{\text{LP}}}{V_i^{\text{NLP}}} \right| \times 100 \quad \forall i \in \mathcal{B} \quad (2.52)$$

$$\xi_I^{(\%)} = \left| \frac{I_{ij}^{\text{NLP}} - I_{ij}^{\text{LP}}}{I_{ij}^{\text{NLP}}} \right| \times 100 \quad \forall ij \in \mathcal{L} \quad (2.53)$$

Where V_i^{NLP} and I_{ij}^{NLP} are the magnitudes of voltage at node i and current in branch ij respectively and are obtained from the NLP model. In the same way, V_i^{LP} and I_{ij}^{LP} represent the same magnitudes obtained from the LP model. On the other hand, for the terms V_i^{NLP} , I_{ij}^{NLP} and V_i^{LP} , they are directly evaluated as the positive square root of the variables V_i^{sqr} and I_{ij}^{sqr} obtained from the NLP and LP models, as the case may be; however, the term I_{ij}^{LP} must be evaluated with the following expression:

$$I_{ij}^{\text{LP}} = \sqrt{\frac{(P_{ij}^{\text{LP}})^2 + (Q_{ij}^{\text{LP}})^2}{(V_j^{\text{LP}})^2}} \quad \forall ij \in \mathcal{L} \quad (2.54)$$

Where P_{ij}^{LP} and Q_{ij}^{LP} are the magnitudes of active power flow at branch ij and current in branch ij , respectively, and V_j^{LP} is the voltage magnitude at node j , all of them obtained from the LP model.

2.4.2 136-Bus Radial Distribution System

The 136-Bus 33.4kV layout radial distribution system from (DELGADO, 2015) has the topology shown in Fig. 2.3. For demonstration purposes with respect to the OPF problem, 02 generators were added at nodes 88 and 106, whose data of generation limits are presented in Appendix A.

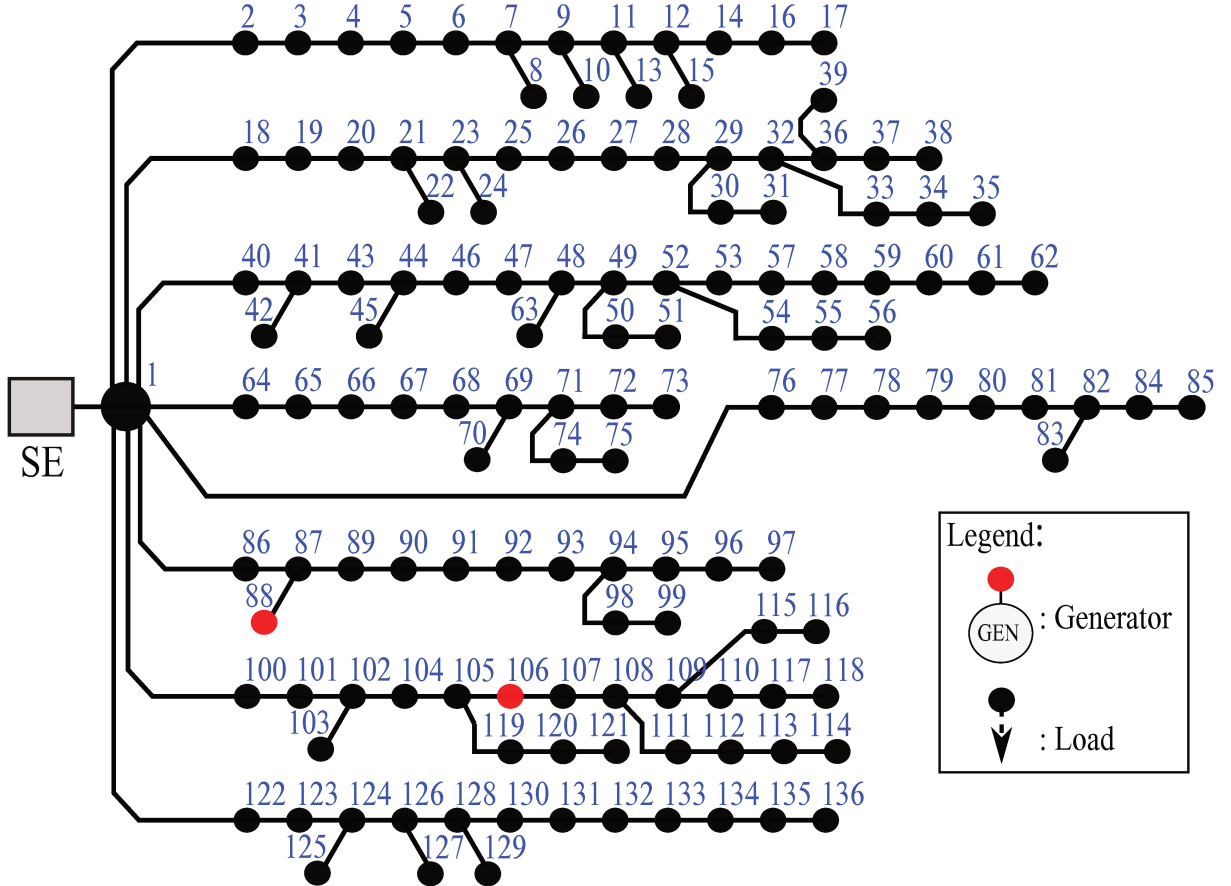


Figure 2.3 – 136-Bus radial distribution system layout.

Fig. 2.4 shows that the percentage of deviations in each variable is small with respect to the one obtained by the NLP model. In Fig. 2.4(a), it can be seen that the percentage deviations are smaller than 0.003% for the voltage magnitude at the buses. In a similar way in Fig. 2.4(b), the percentage deviation of the current magnitude is less than 0.08%.

In Table 2.1, observing the results obtained from the 136-Bus layout RDN system, such as the amount of active and reactive power supplied by the generators, we perceive a small difference in the generator from the reference bus or electrical substation (SE), in addition, the values of the losses for the non-linear exact and the linear approximation model were 136.586 kW and 134.054 kW, respectively.

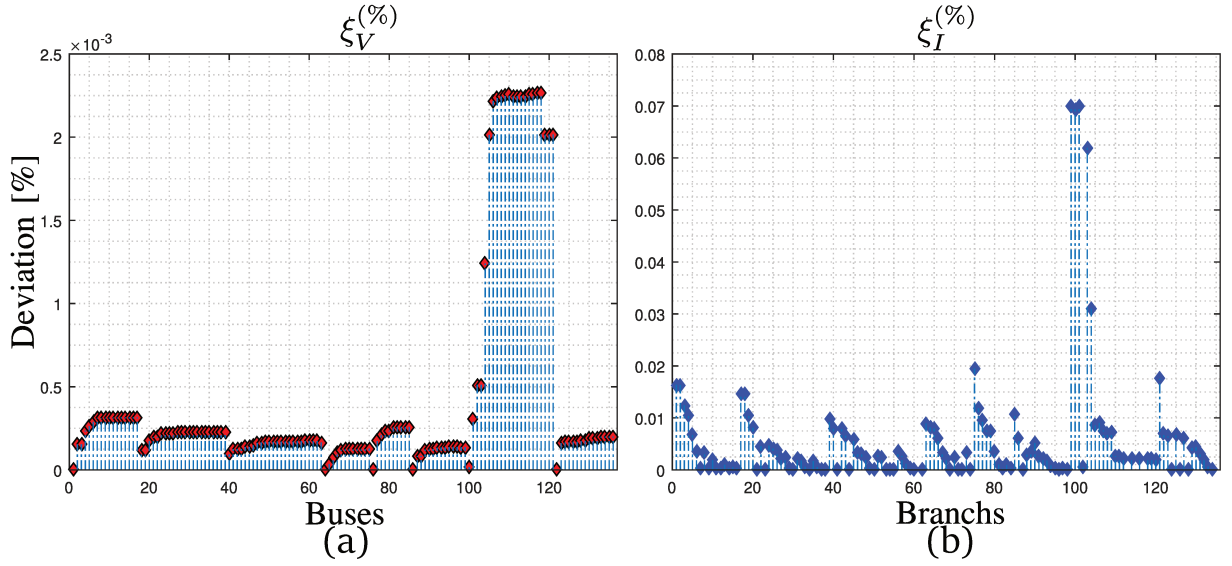


Figure 2.4 – Absolute deviations for the 136-Bus Radial Distribution System.

Table 2.1 – Results for the 136-Bus Radial Distribution System

136-Bus Radial Distribution System	PNL		LP	
Generator production (MW, Mvar)	$P_1^g = 17.449$	$Q_1^g = 7.728$	$P_1^g = 17.447$	$Q_1^g = 7.722$
	$P_{88}^g = 0.50$	$Q_{88}^g = 0.25$	$P_{88}^g = 0.50$	$Q_{88}^g = 0.25$
	$P_{106}^g = 0.50$	$Q_{106}^g = 0.25$	$P_{106}^g = 0.50$	$Q_{106}^g = 0.25$
Active power loss of the system (kW)	136.586		134.054	
Maximum voltage deviation (ξ_V %)	-		0.0023 at node [117]	
Maximum current deviation (ξ_I %)	-		0.0701 at branch [1-100]	
Maximum power flow in the system. (MW, Mvar)	$P_{1-2}=2.599$; $Q_{1-2}=1.139$		$P_{1-2}=2.599$; $Q_{1-2}=1.139$	

2.5 Comments and Conclusions

In this chapter, two models, NLP and linearized LP, were explored to solve an AC-OPF problem for radial distribution networks (RDNs). The NLP model is represented by a set of non-linear equations based on the Branch Flow extension. The NLP equations were approximated by a linear model that can be solved using LP programming. The results of both models were compared for the problem of active power losses using the 136-bus radial distribution system. The results showed a satisfactory performance, obtaining errors of less than 0.07 %, considering only a number of linearization steps of $Y = 50$, emphasizing that if the number of steps increases, the computational cost will be increased, but the results are more accurate. The results showed that the linearized model can be used as an approximation of the original problem.

3 Reactive Power Capability Model of WPP

Notation

Parameters:

Z_{WT}	Impedance of the WT feeder
$\underline{V}_c, \overline{V}_c$	Minimum and maximum permissible grid side converter voltage at WTs
\overline{I}_c	Maximum permissible current limit of grid side converter at WTs
Z_{coll}	Aggregated equivalent impedance of wind power collection system
Z_{WPP}	Aggregated equivalent impedance of wind power plant
B_{WPP}^{sh}	Aggregated equivalent shunt capacitance of wind power collection system.

Variables:

\vec{I}	Current flowing into the WPP collector grid from WT feeder
P^{WT}, Q^{WT}	Active and reactive power supplied by the WT feeder
V_{LV}, V_{HV}	Low and high voltage side of the ideal WT transformer.

Sets:

Γ^{WT}, Γ^{SE}	Set of wind power generation level at WTs and voltage magnitude level at the LV side of the main transformer
----------------------------	--

Functions:

$\overline{Q}_{WT}^I, \underline{Q}_{WT}^I$	Maximum reactive power for injection and absorption of WT by the converter current
$\overline{Q}_{WT}^V, \underline{Q}_{WT}^V$	Maximum reactive power for injection and absorption of WT by the converter voltage
$Q_{inj}^{WT}, Q_{abs}^{WT}$	Maximum reactive power injection and absorption capability of WT
$Q_{inj}^{WPP}, Q_{abs}^{WPP}$	Maximum reactive power injection and absorption capability of WPP

3.1 Introduction

In this Chapter, the methods found in literature to estimate the reactive power capability (RPC) of WPP are described. The main challenge to obtain the RPC for WPPs is that the wind turbines (WTs) are scattered and interconnected by a collecting network. As a result, the active and reactive losses and the parameters of the branches can no longer be neglected. There are three basic approaches to estimate the RPC: scaled, aggregated and detailed. The scaled approach scales up all the individual WT capability curves inside a WPP, such as proposed in (Konopinski; Vijayan; Ajjarapu, 2009; Meegahapola; Littler; Pereraa, 2013). The main disadvantage of this approach is that the collector system is not represented, resulting in an overestimated RPC (Sarkar et al., 2019). In the aggregated approach, a methodology is proposed to estimate the equivalent impedance among the WPP and PCC (Sarkar et al., 2019). The main goal of this approach is to combine the advantages of the scaling and detailed approaches resulting in an estimation of RPC close to the detailed method with low computational burden. The detailed approach considers the full model of a WT, including the grid-side-converter (GSC) parameters and the internal AC network (Ullah; Bhattacharya; Thiringer, 2009; Kim et al., 2016; Karbouj; Rather, 2018). The main disadvantage of the detailed approach is the expensive computational burden. It also should be noted that none of the approaches presented in the literature take into account the operating and electrical limits of the WTs and collecting system.

The rest of the chapter is organized as follows: Section 3.2 presents the modeling of the reactive power capability of a single Type-4 wind turbine. Section 3.3 presents the reactive power capability approach for WPPs. Finally, Section 3.4 contains the summary of the chapter.

3.2 Reactive Power Capability Model of Type-4 WT

A Type-4 WT presents a great deal of flexibility in design and operation as the output of the rotating machine is sent to the grid through a full-scale back-to-back frequency converter. The frequency converter offers reactive power compensation (i.e. reactive power supply to the grid, much like a STATCOM) and a smoother grid connection for the entire speed range. Hence, Type-4 WTs can use direct drive synchronous generators and the gearbox may be eliminated. In the last decade, advances in power electronic devices and controls have made the converters both responsive and efficient (GLOVER; SARMA; OVERBYE, 2012). There are two generic models proposed in the IEC 61400-27 standard (Types 4A and 4B) for Type-4 WTs. The main difference between them is the two-mass mechanical model included in Type 4B WTs (to reflect that the drive train oscillations are excited during grid faults) (Das; HANSEN; Sørensen, 2016). However, in

this work we are constrained to the steady-state operation and the dynamic response is neglected. The main components of a Type-4 WT are presented in Fig. 3.1.

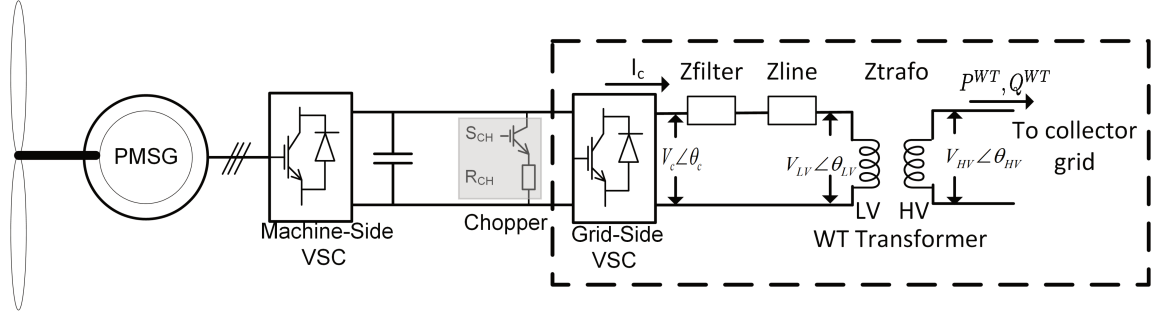


Figure 3.1 – Schematic representation of a Type-4 WT connected to the WPP's collector grid. [Source: adapted from (Sarkar et al., 2019)]

The Type-4 WT is composed by a grid side converter (GSC) with permanent magnet synchronous generator (PMSG) that is connected to the WT transformer through a filter and a short line. Since a WT generates power at a low voltage level (typically 0.69 kV), the WT transformer is used to step-up the voltage to the collector grid (typically 22.9 kV).

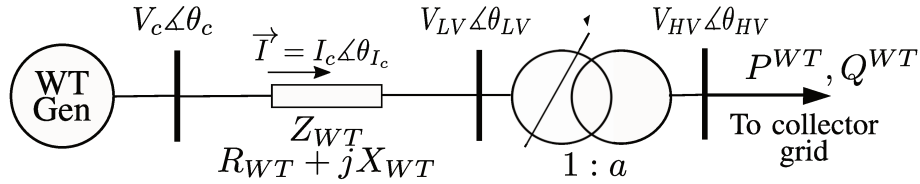


Figure 3.2 – Equivalent representation of a WT feeder connected to the WPP's collector grid. [Source: adapted from (Sarkar et al., 2019)]

The steady-state model of the Type-4 WT can be represented as single WT feeder connected to a collector grid such as presented in Fig. 3.2, where V_c and I_c represent the converter voltage magnitude and current carrying of GSC, respectively; Z_{WT} represents the equivalent impedance (including the filter and the transmission line) between the GSC and the high-voltage-side (HV) of the WT transformer. V_{LV} represents the voltage magnitude at the low-voltage-side (LV) of the ideal WT transformer. The transformer has a tap-changing mechanism represented by the discrete control variable " a ". Reactive power capability of a WT is dependent on two limiting factors: converter voltage limitation and converter current limitation. In the following subsections, analytical equations will be developed in order to determine the limits of the reactive power capability curve based on these specified limits (V_c and I_c).

3.2.1 Converter Current Limitation

The current-carrying capacity in the GSC is obtained by the relation between active and reactive power generation at the LV side of the WT feeder (P^{WT} and Q^{WT}), as shown in (3.1):

$$(P^{\text{WT}})^2 + (Q^{\text{WT}})^2 = (V_{\text{LV}} I_c)^2 \quad (3.1)$$

The reactive power limits for injection ($\overline{Q}_{\text{WT}}^I$) and absorption ($\underline{Q}_{\text{WT}}^I$) by the converter's current can be obtained from positive and negative roots of (3.1), respectively. Note that the reactive power module in (3.2) and (3.3) is at its maximum using the maximum current of GSC (\overline{I}_c).

$$\overline{Q}_{\text{WT}}^I (V_{\text{LV}}, P^{\text{WT}}) = \sqrt{(V_{\text{LV}} \overline{I}_c)^2 - (P^{\text{WT}})^2} \quad (3.2)$$

$$\underline{Q}_{\text{WT}}^I (V_{\text{LV}}, P^{\text{WT}}) = -\sqrt{(V_{\text{LV}} \overline{I}_c)^2 - (P^{\text{WT}})^2} \quad (3.3)$$

3.2.2 Converter Voltage Limitation

The converter voltage limit in GSC is obtained by the relation between active and reactive power generation at the LV side of the WT feeder (P^{WT} and Q^{WT}) calculated due to current flowing into the WPP's collector network, as shown in the following complex expression:

$$P^{\text{WT}} + jQ^{\text{WT}} = V_{\text{LV}} \angle \theta_{\text{LV}} \vec{I}^* \quad (3.4)$$

The current flowing into the WPP collector grid (\vec{I}) can be expressed as (3.5).

$$\vec{I} = \frac{V_c \angle \theta_c - V_{\text{LV}} \angle \theta_{\text{LV}}}{Z_{\text{WT}}} \quad (3.5)$$

Substituting the current (\mathbf{I}) in (3.4):

$$P^{\text{WT}} + jQ^{\text{WT}} = V_{\text{LV}} \angle \theta_{\text{LV}} \left(\frac{V_c \angle \theta_c - V_{\text{LV}} \angle \theta_{\text{LV}}}{Z_{\text{WT}}} \right)^* \quad (3.6)$$

Identifying the real and imaginary parts in the equation (3.6), the following are obtained:

$$P^{\text{WT}} = \frac{1}{Z_{\text{WT}}^2} [V_{\text{LV}} V_c (R_{\text{WT}} \cos \theta - X_{\text{WT}} \sin \theta) - V_{\text{LV}}^2 R_{\text{WT}}] \quad (3.7)$$

$$Q^{\text{WT}} = \frac{1}{Z_{\text{WT}}^2} [V_{\text{LV}} V_c (X_{\text{WT}} \cos \theta + R_{\text{WT}} \sin \theta) - V_{\text{LV}}^2 X_{\text{WT}}] \quad (3.8)$$

Adding the squares of (3.7) and (3.8), and using the trigonometric relationships, the following is obtained:

$$\left(P^{\text{WT}} + \frac{V_{\text{LV}}^2 R_{\text{WT}}}{Z_{\text{WT}}^2} \right)^2 + \left(Q^{\text{WT}} + \frac{V_{\text{LV}}^2 X_{\text{WT}}}{Z_{\text{WT}}^2} \right)^2 = \frac{(V_{\text{LV}} V_c)^2}{Z_{\text{WT}}^2} \quad (3.9)$$

The reactive power limits for injection ($\overline{Q}_{\text{WT}}^V$) and absorption ($\underline{Q}_{\text{WT}}^V$) by the converter voltage can be obtained from the positive root of (3.9) and maximum/minimum converter voltage, respectively.

$$\overline{Q}_{WT}^V(V_{LV}, P^{WT}) = \sqrt{\frac{(V_{LV}\overline{V}_c)^2}{Z_{WT}^2} - \left(P^{WT} + \frac{V_{LV}^2 R_{WT}}{Z_{WT}^2}\right)^2} - \frac{V_{LV}^2 X_{WT}}{Z_{WT}^2} \quad (3.10)$$

$$\underline{Q}_{WT}^V(V_{LV}, P^{WT}) = \sqrt{\frac{(V_{LV}\underline{V}_c)^2}{Z_{WT}^2} - \left(P^{WT} + \frac{V_{LV}^2 R_{WT}}{Z_{WT}^2}\right)^2} - \frac{V_{LV}^2 X_{WT}}{Z_{WT}^2} \quad (3.11)$$

Note that the reactive power in (3.10) and (3.11) is at its maximum using the maximum/minimum converter voltage of GSC (\overline{V}_c).

Given an arbitrary value of $V_{LV} = 0.95$ pu, Fig. 3.3 shows the limits of reactive power injection for $P^{WT} = [0.0, 1.0]$ pu, using the expressions (3.2)–(3.3) and (3.10)–(3.11).

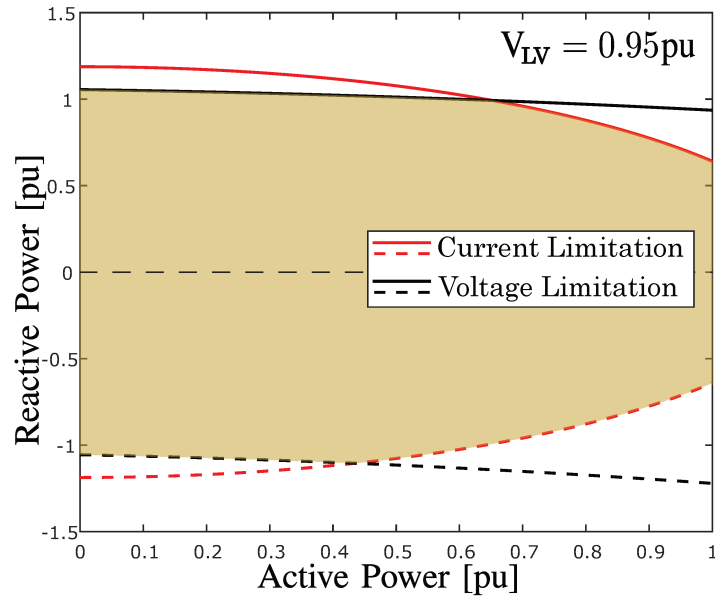


Figure 3.3 – WT power capability curve with limited voltage and current. [Source: adapted from (Sarkar et al., 2019)]

Note that the area of the intersection between the curves represents the reactive power capability of an individual WT feeder. Therefore, the maximum reactive power injection, Q_{inj}^{WT} , and absorption, Q_{inj}^{WT} capability of an individual WT feeder can be written as:

$$Q_{inj}^{WT} = \min(\overline{Q}_{WT}^I, \overline{Q}_{WT}^V) \quad (3.12)$$

$$Q_{abs}^{WT} = \max(\underline{Q}_{WT}^I, \underline{Q}_{WT}^V) \quad (3.13)$$

Fig. 3.4 shows the WT reactive power capability at the LV side of the WT transformer (V_{LV}) for different voltage magnitudes in an operating $[0.95-1.05]$ pu using expressions (3.12) and (3.13), in order to observe the impact of the reactive power generation due to the voltage magnitude. These results are obtained using the electrical parameters of the WT feeder that are presented in Appendix C.

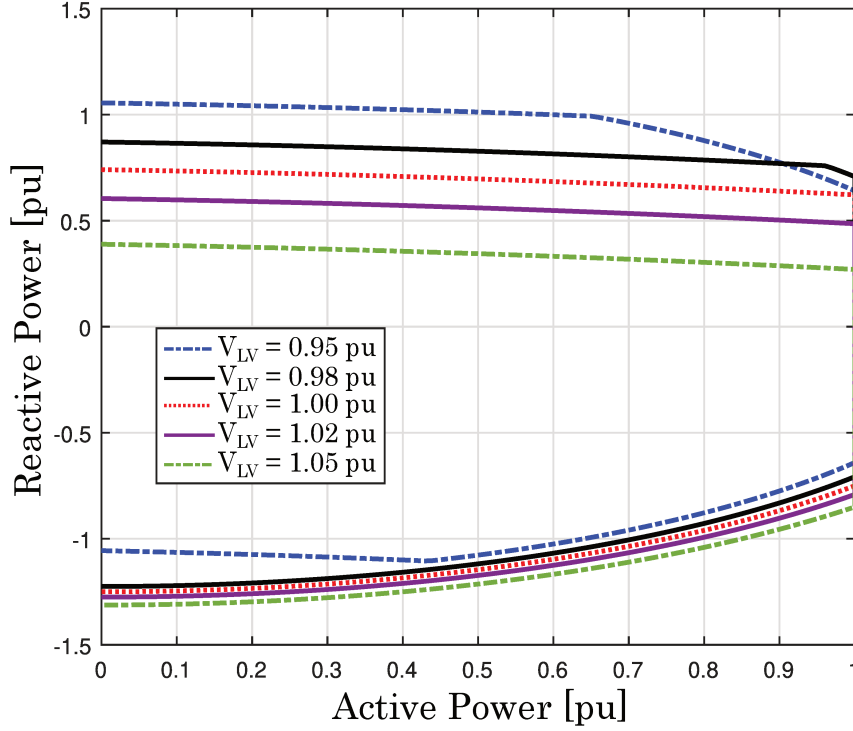


Figure 3.4 – Reactive power capability curves for Type-4 WT. [Source: adapted from (Sarkar et al., 2019)]

3.3 WPP Reactive Power Capability Model

This section presents a review of the different methodologies to estimate the WPP's reactive power capability (Sarkar et al., 2019). Three approaches are considered: scaling, aggregated and detailed. For these three approaches the following general assumptions are taken:

- WPP reactive power capability is determined at the LV side of the main transformer;
- The voltage regulation in the WT transformers remains constant and equal to one;
- All WTs produce the same active power. Hence, spatial variation in wind speed (due to variability in wind and wake effect) is neglected.

3.3.1 Scaled WT Model

The WPP capability curve is derived by scaling up the WT capability curve with the number of WTs. The electrical parameters of the collector system are neglected (Meegahapola; Littler; Pereraa, 2013; Konopinski; Vijayan; Ajjarapu, 2009) and directly given by (3.14) and (3.15):

$$Q_{\text{inj}}^{\text{WPP}} = N \times Q_{\text{inj}}^{\text{WT}} \quad (3.14)$$

$$Q_{\text{abs}}^{\text{WPP}} = N \times Q_{\text{abs}}^{\text{WT}} \quad (3.15)$$

Where, N represents the total amount of WTs in operation, Q_{inj}^{WT} and Q_{abs}^{WT} present the maximum reactive power injection/absorption capability of WT, respectively. All the parameters are in pu.

3.3.2 Aggregated WPP Model

In this model a series and shunt equivalent impedance are estimated to represent the collector system (Sarkar et al., 2019). A procedure based on circuit analysis is used to determine the equivalent impedance, which is calculated from the apparent power loss in the WPP's collector system (Muljadi et al., 2006). The equivalent system that represents impedance of the grid and shunt capacitance of the collector system is shown in Fig. 3.5:

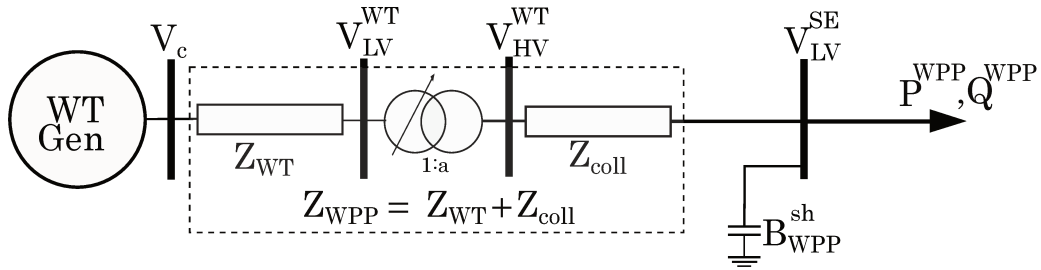


Figure 3.5 – A single WT representation of WPP with aggregated WPP collection system. [Source: adapted from (Sarkar et al., 2019)].

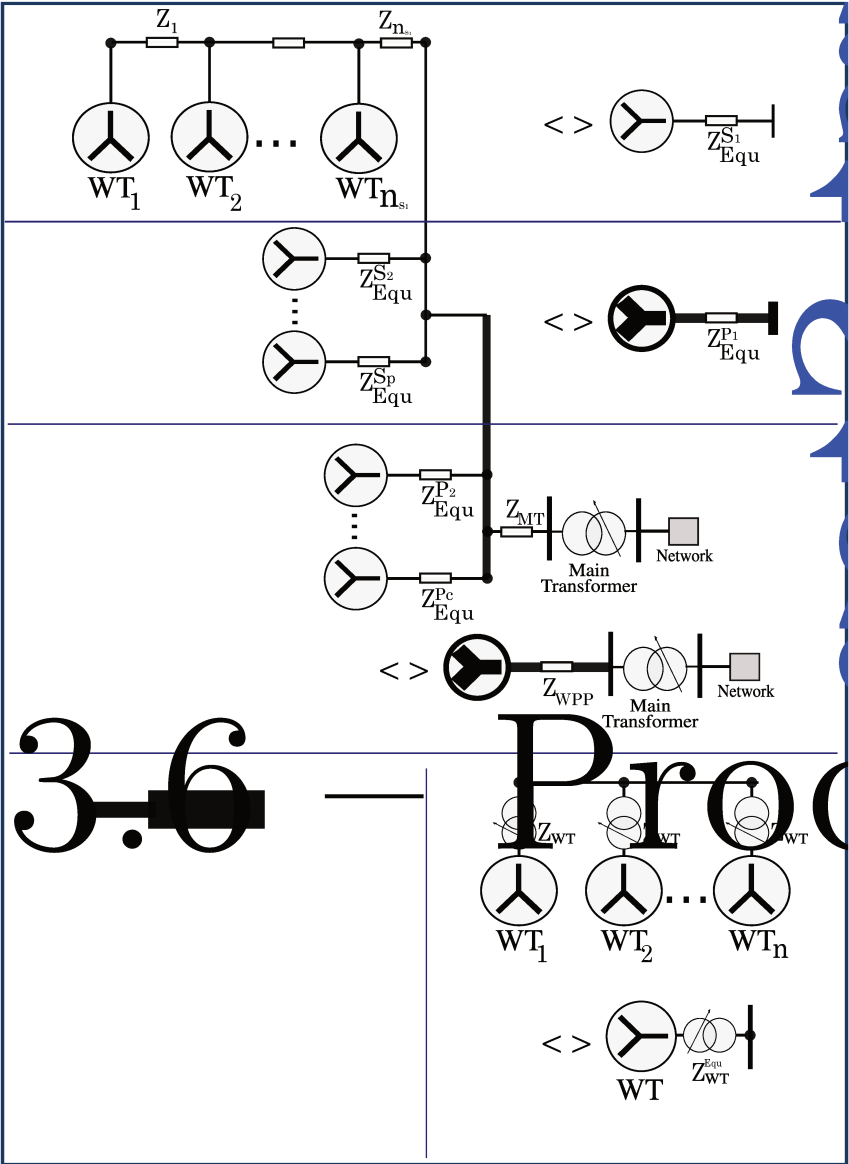
Where, Z_{WT} represents the equivalent impedance of WT feeder (filter, line and WT transformer), Z_{coll} represents the equivalent impedance of the collector system and Z_{WPP} represents the combined impedance of the WT's feeder model and the WPP's collector system. B_{WPP}^{sh} represents the equivalent shunt susceptance.

In this approach, the RPC is determined into two key stages: i) to estimate the WPP equivalent impedances; ii) from the equivalent impedances (Z_{WPP} , B_{WPP}^{sh}), voltage at reference bus (V_{LV}^{SE}) and active power (P^{WPP}) the reactive power (Q_{inj}^{WPP} , Q_{abs}^{WPP}) can be estimated, and, consequently, the RPC. These two stages will be described in detail as follows.

3.3.2.1 WPP Equivalent Impedance

The authors proposed a back to forward procedure where an equivalent impedance of the group of WTs furthest from the main transformer is estimated and subsequently steps are realized in the direction of the branches close to the main transformer. To reach this goal the following assumptions are taken: i) the current injection from all WTs are equal in magnitude and angle; ii) reactive power generated by the line capacitive shunt is calculated considering the bus voltage equal to 1 pu.

The procedure to calculate the WPP's equivalent impedances is divided into five steps, which are illustrated in Fig. 3.6.



(left graph), thus obtaining the circuit equivalent (right graph) with its respective equivalent impedance Z_{WPP} .

- Fourth step: to estimate the line shunt capacitance equivalent B_{WPP} from all branches of the collector system considering all the bus voltages equal to 1 pu.
- Fifth step: to estimate the equivalent impedance Z_{WT}^{Equ} from all WT feeders considering that all of them are connected in parallel. The deduction of the calculation of the equivalent impedance for each step is described in Appendix B.

3.3.2.2 WPP Reactive Power Capability

As can be seen, the equivalent scheme of the WPP shown in Fig. 3.5 is similar to a WT feeder shown in Fig. 3.2. Then, using the parameters in Fig. 3.5, the WPP reactive power can be calculated from Equations (3.2)–(3.3) and (3.10)–(3.11). Using the aggregated WPP notation it results in the following expressions:

$$\overline{Q}_{WPP}^I(V_{LV}, P^{WPP}) = \sqrt{(V_{LV}\overline{I}_c)^2 - (P^{WPP})^2} \quad (3.16)$$

$$\underline{Q}_{WPP}^I(V_{LV}, P^{WPP}) = -\sqrt{(V_{LV}\overline{I}_c)^2 - (P^{WPP})^2} \quad (3.17)$$

$$\overline{Q}_{WPP}^V(V_{LV}, P^{WPP}) = \sqrt{\frac{(V_{LV}\overline{V}_c)^2}{Z_{WPP}^2} - \left(P^{WPP} + \frac{V_{LV}^2 R_{WPP}}{Z_{WPP}^2}\right)^2} - \frac{V_{LV}^2 X_{WPP}}{Z_{WPP}^2} \quad (3.18)$$

$$\underline{Q}_{WPP}^V(V_{LV}, P^{WPP}) = \sqrt{\frac{(V_{LV}\underline{V}_c)^2}{Z_{WPP}^2} - \left(P^{WPP} + \frac{V_{LV}^2 R_{WPP}}{Z_{WPP}^2}\right)^2} - \frac{V_{LV}^2 X_{WPP}}{Z_{WPP}^2} \quad (3.19)$$

Similar to the WT reactive power capability model, reactive power injected by susceptance of the WPP collection grid B_{WPP}^{sh} is added to the maximum injection and absorption capability obtained at the LV side of the main transformer. Therefore, the maximum reactive power injection, Q_{inj}^{WPP} , and absorption, Q_{abs}^{WPP} capability of WPP are calculated by the following expressions:

$$Q_{inj}^{WPP} = \min(\overline{Q}_{WPP}^I, \overline{Q}_{WPP}^V) + V_{LV}^2 B_{WPP}^{sh} \quad (3.20)$$

$$Q_{abs}^{WPP} = \max(\underline{Q}_{WPP}^I, \underline{Q}_{WPP}^V) + V_{LV}^2 B_{WPP}^{sh} \quad (3.21)$$

3.3.3 WPP Detailed Model

In this method the full model of the electrical components of a WPP is used (Ullah; Bhattacharya; Thiringer, 2009; Kim et al., 2016; Karbouj; Rather, 2018). The general idea of this method is to run multiple power flow (AC-PF) cases through a loop process. In each iteration (k) different specified scenarios are considered, such as: wind power generation level at WTs, voltage magnitude level at reference bus and operation mode. This approach is considered as a base method, being useful for validation and comparison with the other two approaches described in this chapter (Sarkar et al., 2019). Although providing accurate WPP reactive power capability, the disadvantages of this method are: (i) knowledge of all WPP parameters (what may be difficult in planning stage), (ii) expensive computation burden for large WPPs, (iii) capacitor bank operation and the transformation ratio a are not considered as discrete control variables.

The method to perform the AC-PF on the detailed model proposed in (Sarkar et al., 2019) is described in the flowchart illustrated in Fig. 3.6. In order to exemplify the RPC using the present approach, we found it useful to describe the solution strategy in the next subsection.

3.3.3.1 Algorithm proposed by Sakar et al., 2019

The procedure to calculate the estimated RPC for a given voltage at the reference bus is described by the following items:

- *Initial conditions:* The algorithm starts by setting the initial values, such as the LV end of the WPP transformer, set as the reference bus and this reference bus voltage is varied to obtain WPP reactive power capability curves according to the elements of Γ^{SE} . In addition, WT generator buses are set as PV buses.
- *Calculating WT reactive power limits:* Maximum and minimum reactive power limits of WT generators are calculated with voltages equal to \bar{V}_c (to calculate $Q_{\text{inj}}^{\text{WT}}$) or \underline{V}_c (to calculate $Q_{\text{abs}}^{\text{WT}}$) using a WT RPC curve model.
- *Multiple power flow:* AC-PF is executed enforcing reactive power limits on the WT generators. WT generator buses are converted to PQ buses when the reactive power limit is reached. Initially, all HV end buses of the WT transformer are assumed to have the same voltages as the reference voltage. Since these voltages are close enough but not equal in practice, the AC-PF results are used to update the voltages at the HV ends of the WT transformer. This changes the reactive power capability at the LV end of the WT transformer. Therefore, the reactive powers calculated at the LV ends of the WT transformers are compared with the results of previous iterations in order to check if the error is within tolerated levels (first-loop). This

process is repeated for all values of the active power; from the initial to the final value (Second.-loop).

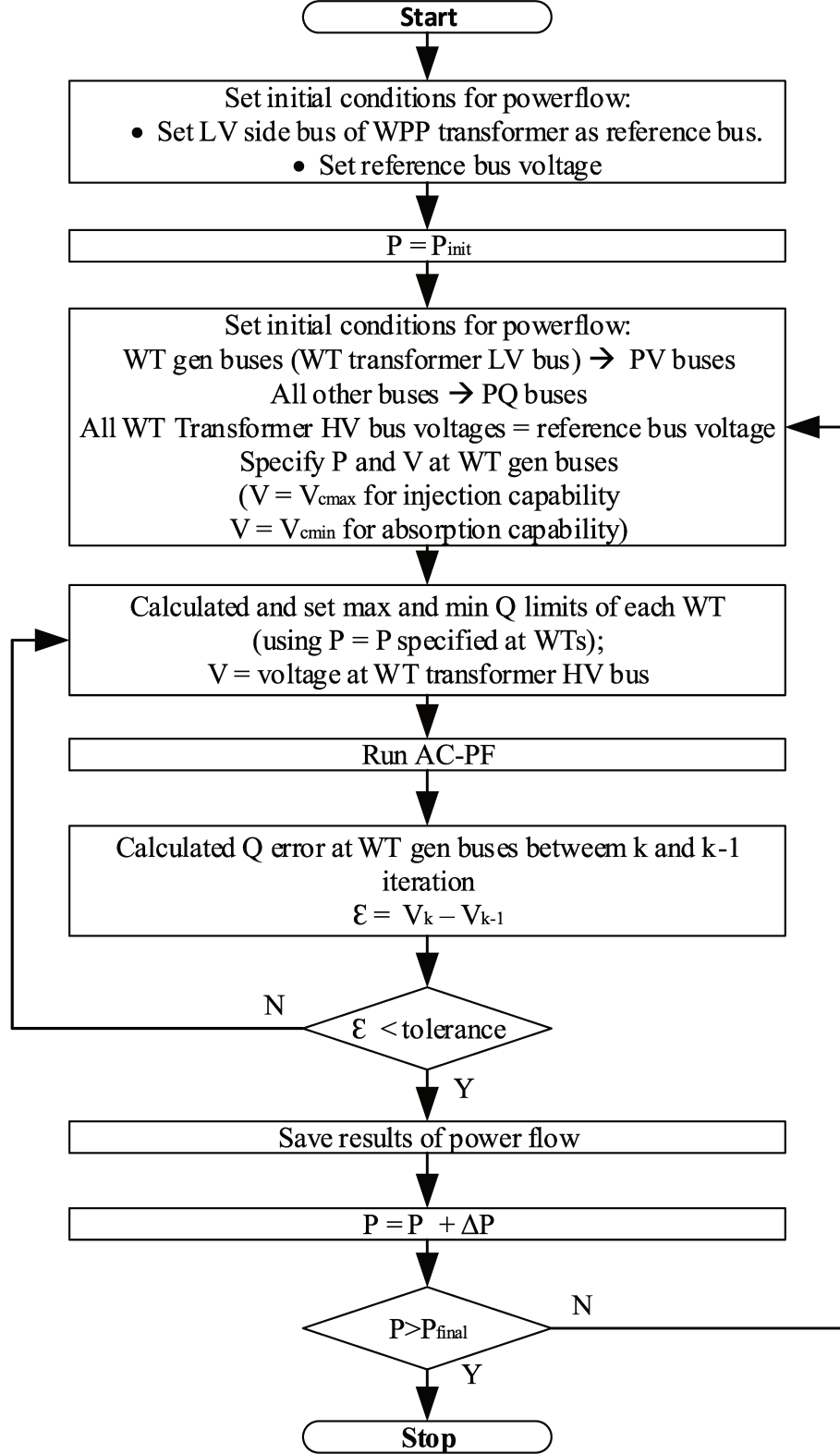


Figure 3.7 – Flowchart to determine WPP reactive power capability using a detailed model.
[Source: from (Sarkar et al., 2019)]

3.4 Summary

In this chapter, some key design and operation aspects of a Type-4 WT and a WPP were developed to represent the RPC estimation problem. These were divided into the following approaches: (a) Modeling of the reactive power capability of a Type-4 WT; (b) Review of methodologies focused on RPC estimation for WPPs.

Firstly, the size of each WT reactive power capability curve depends on the grid-side converter (GSC) parameters. Additionally, the RPC limits of WTs are represented by functions of a non-linear nature with two independent variables: the amount of active power generation at a WT and grid-side voltage magnitude (HV side of the individual WT transformer), both of which are random variables. These non-linear functions are not recommended to be directly addressed in the formulation of optimization problems, since it would present the main disadvantages, such as expensive computational burden and not guaranteeing the optimal global solution.

Secondly, the methodologies focused on determining the WPC RPC described in this Chapter are flexible and scalable for any WT type. The detailed approach is considered a base methodology because it presents a full model of the electrical components. However, the main disadvantage is the difficulty in being implemented and the high computational burden for large WPPs. The scaled approach attempts to represent the RPC estimation with low computational burden. However, this could not be more considered since it does not consider a basic key factor, such as active and reactive power losses, resulting an overestimation in the RPC curves. The aggregate approach is a recent methodology, presenting an equivalent impedance that allows simplifying the collector system to a circuit equivalent (line and WT feeder), thus obtaining the RPC curves with an acceptable accuracy with respect to the detailed method. This can be useful for real-time operation since the computational burden is very low even for large WPPs. Notwithstanding, the collector system limits are neglected in the described methodologies. This is a key factor that will impact the RPC curves. This impact will be analyzed in Chapter 5.

4 Optimized Reactive Power Capability of Wind Power Plant

Notation

Sets:

\mathcal{B}	Set of nodes (Buses)
\mathcal{L}	Set of circuit (Branches) where $\mathcal{L} \subseteq \mathcal{B} \times \mathcal{B}$
\mathcal{G}	Set of transformer branch at WT feeder
\mathcal{C}	Set of WPP operation modes.
\mathcal{K}	Set of scenarios, defined as $\Gamma^{\text{WT}} \times \Gamma^{\text{SE}}$.
Γ^{WT}	Set of wind power generation scenarios at the WTs
Γ^{PCC}	Set of voltage magnitude scenarios at PCC.

Indexes:

i	Node (Bus "From") $i \in \mathcal{B}$
j	Node (Bus "To") $j \in \mathcal{B}$
ij	Circuit (Branch) $ij \in \mathcal{L}$
c	WPP operation mode $c \in \mathcal{C}$, where $c = 1$ if the WPP is in reactive injection mode, and $c = 2$ if the WPP is in reactive absorption mode
k_1, k_2	Scenario $k_1 = (\gamma^{\text{WT}}, \gamma^{\text{PCC}})$; $k_2 = (\wp^{\text{WT}}, \wp^{\text{PCC}})$ and $\{k_1, k_2\} \in \mathcal{K}$
$\gamma^{\text{WT}}, \wp^{\text{WT}}$	Scenario $\{\gamma^{\text{WT}}, \wp^{\text{WT}}\} \in \Gamma^{\text{SE}}$
$\gamma^{\text{PCC}}, \wp^{\text{PCC}}$	Scenario $\{\gamma^{\text{PCC}}, \wp^{\text{PCC}}\} \in \Gamma^{\text{SE}}$

Parameters:

\mathcal{B}_i^{T}	Node type at bus i , where it can take the values of 0,1 and 2 for PQ, PV and reference bus, respectively
$\mathcal{L}_{ij}^{\text{T}}$	Circuit type at branch ij , where it can take the values of 0,1 and 2 for standard branch, NLTC and OLTC transformer, respectively

Z_{WT}	Equivalent impedance ($R_{WT} + jX_{WT}$) of WT from the converter to the transformer.
$\underline{V}_c, \overline{V}_c$	Minimum and maximum permissible grid side converter voltage at WTs
\overline{I}_c	Maximum permissible current limit of grid side converter at WTs
$\overline{P}_i^{\text{WT}}$	Nominal active power generation of WT at bus i
B_i^{sh}	Shunt susceptance at bus i
B_{ij}^{sh}	Susceptance of branch ij
\overline{I}_{ij}	Maximum current magnitude of branch ij .
P_i^d, Q_i^d	Active and reactive power demand at bus i
R_{ij}, X_{ij}	Resistance and reactance of branch ij
Z_{ij}	Impedance of branch ij
\overline{S}_{ij}	Maximum capacity of branch ij
$\underline{V}_i, \overline{V}_i$	Minimum and maximum voltage magnitude at bus i
$R^\%, R_{\text{WT}}^\%$	Regulation rate of the main and WT transformer
\overline{n}	Maximum number of taps at the main transformer
\overline{n}_{WT}	Maximum number of taps at the WT transformer
V'_{i,c,k_1}	Approximation of the voltage magnitude at bus i , operation mode c and scenario k_1
V^n	Nominal voltage magnitude
Y	Number of linearization blocks
Δ_{ij}^S	Upper limit of each linearization block

Continuous variables:

$a_{ij}^{\text{NLTC}}, a_{ij,c,k_1}^{\text{OLTC}}$	Voltage magnitude ratio of the transformer equipped with NLTC and OLTC at branch ij , operation mode c and scenario k_1
$I_{ij,c,k_1}, I_{ij,c,k_1}^{\text{sqr}}$	Magnitude and square value of the current flow at branch ij , mode c and scenario k_1
$P_{c,k_1}^{\text{PCC}}, Q_{c,k_1}^{\text{PCC}}$	Active and reactive power exchange at the PCC, at operation mode c and scenario k_1
$P_{ij,c,k_1}, Q_{ij,c,k_1}$	Active and reactive power flow at branch ij , operation mode c and scenario k_1

$P_{i,c,k_1}^{\text{WT}}, Q_{i,c,k_1}^{\text{WT}}$	Active and reactive power generated by the WT at node i , mode c and scenario k_1
$P_{ij,c,k_1}^+, P_{ij,c,k_1}^-$	Auxiliary non-negative variable for the linearization of $ P_{ij,c,k_1} $, at operation mode c and scenario k_1
$Q_{ij,c,k_1}^+, Q_{ij,c,k_1}^-$	Auxiliary non-negative variable for the linearization of $ Q_{ij,c,k_1} $, at operation mode c and scenario k_1
$V_{\text{LV},i,c,k_1}, V_{\text{LV},i,c,k_1}^{\text{sqr}}$	Magnitude and square value of the voltage in the LV-side of the WT transformer at bus i , operation mode c and scenario k_1
$V_{i,c,k_1}, V_{i,c,k_1}^{\text{sqr}}$	Magnitude and square value of the voltage at bus i , operation mode c and scenario k_1
V_{ij,c,k_1}^c	Auxiliary variable for representing the product $a_{ij,c,k_1}^2 V_{i,c,k_1}^{\text{sqr}}$, at branch ij , operation mode c and scenario k_1
$\Delta_{ij,c,k_1,y}^P, \Delta_{ij,c,k_1,y}^Q$	Value of the y^{th} linearization block for the active and reactive power flow at branch ij , operation mode c and scenario k_1

Binary and integer variables:

$v_{ij,w}^{\text{NLTC}}, v_{ij,c,k_1,w}^{\text{OLTC}}$	Binary variable used to calculate the regulated voltage magnitude at branch ij , operation mode c , scenario k_1 and step w
$n_{ij}^{\text{NLTC}}, n_{ij,c,k_1}^{\text{OLTC}}$	Integer variable used to determinate tap-changer position of transformer equipped with NLTC and OLTC at branch ij , operation mode c and scenario k_1 .

Functions:

$\overline{Q}_{\gamma\text{WT}}^I, \underline{Q}_{\gamma\text{WT}}^I$	Non-linear representation of the reactive power production limits due to the current magnitude limits \overline{I}_c at WT Feeder
$\overline{Q}_{\gamma\text{WT}}^V, \underline{Q}_{\gamma\text{WT}}^V$	Non-linear representation of the reactive power production limits due to the voltage magnitude limits at the GSC converter \overline{V}_c and \underline{V}_c at WT Feeder
$\overline{h}_{\gamma\text{WT}}^I, \underline{h}_{\gamma\text{WT}}^I$	Linear representation of the reactive power production limits due to the current magnitude limits \overline{I}_c at WT Feeder
$\overline{h}_{\gamma\text{WT}}^V, \underline{h}_{\gamma\text{WT}}^V$	Linear representation of the reactive power production limits due to the voltage magnitude limits at the GSC converter \overline{V}_c and \underline{V}_c at WT Feeder

4.1 Introduction

In this work we proposed an optimal power flow approach to select the optimal tapping settings in order to increase the WPP RPC. This new methodology is based on a detailed model including the collector system limits, discrete variables (tap-changer and capacitor banks) as well as the uncertainties scenarios such as: active power generation at WTs, PCC voltage magnitudes and WPP operation modes (inductive or capacitive). It should be noted that the majority of transformers in a WPP are no-load tap changers (NLTC). Thus, tap settings cannot be changed in real-time operation. As a result, they must be defined during the planning stage in order to improve the reactive power capability.

The aim of this chapter is to present the mathematical formulation based on the branch-flow model, in order to solve the optimized reactive power capability (ORPC) problem. A mixed-integer nonlinear programming model (MINLP) is proposed and approximated by a mixed-integer linear programming (MILP) model. Efficient linearization and approximation techniques are applied to obtain the equivalent Type-4 WT reactive power capability, as well as the tap-changer in the transformers and the AC internal network, all of them expressed in mixed-integer linear form. This MILP model can be solved using off-the-shelf mathematical programming solvers guarantee an optimal solution in reasonable time.

The rest of the chapter is organized as follows: Section 4.2 presents MINLP formulation to solve the ORPC as a two-mode model. Section 4.3 presents the linearization and approximation techniques to obtain the MILP formulation of the ORPC initial model. Section 4.3 presents an extension of the initial ORPC model including specific scenarios. Finally, Section 4.4 contains the summary of the chapter.

4.2 Optimized Reactive Power Capability as a Two-Mode Model

The ORPC problem determines the tap position of the NLTC/OLTC transformers and the capacitor banks that maximize the production/consumption of reactive power being absorbed/injected into the WPP, considering a list of plausible scenarios for PCC voltage magnitudes and active power generation at each WT unit. The model comprises two operation modes: inductive (for reactive power absorption) and capacitive (for reactive power injection). In order to formulate the ORPC's initial model, the following assumptions are made:

- The wind speed throughout the area of the WPP is constant, that is, the production levels of all WT units are the same.
- All WT transformers have similar tap-changing mechanisms.

4.2.1 Formulation of the ORPC's Initial Model

The ORPC problem in (4.1)–(4.20) is an MINLP, in which the branch flow formulation for single-phase AC distribution networks has been adapted from (Low; Farivar, 2013).

Block (A.0): Objective function

$$\max \quad \mathbf{f}_o = (Q_{\text{inj}}^{\text{WPP}} + Q_{\text{abs}}^{\text{WPP}}) = \sum_{c \in \mathcal{C}} Q_c^{\text{PCC}} \quad (4.1)$$

Subject to:

Block (A.1): AC power flow at the collector grid

$$P_{i,c}^{\text{WT}} - P_i^d + \sum_{ji \in \mathcal{L}} P_{ji,c} - \sum_{ij \in \mathcal{L}} (P_{ij,c} + R_{ij} I_{ij,c}^{\text{sqr}}) = 0, \quad \forall i \in \mathcal{B} | \mathcal{B}_i^{\text{T}} \neq 3, c \in \mathcal{C} \quad (4.2)$$

$$Q_{i,c}^{\text{WT}} - Q_i^d - Q_{i,c}^{\text{sh}} + \sum_{ji \in \Omega_l} (Q_{ji,c} + B_{ji}^{\text{shl}} V_{i,c}^{\text{sqr}}) - \sum_{ij \in \Omega_l} (Q_{ij,c} - B_{ij}^{\text{shl}} V_{i,c}^{\text{sqr}} + X_{ij} I_{ij,c}^{\text{sqr}}) = 0, \quad \forall i \in \mathcal{B} | \mathcal{B}_i^{\text{T}} \neq 3, c \in \mathcal{C} \quad (4.3)$$

$$V_{i,c}^{\text{sqr}} - V_{j,c}^{\text{sqr}} = 2(R_{ij} P_{ij,c} + X_{ij} Q_{ij,c}) + Z_{ij}^2 I_{ij,c}^{\text{sqr}}, \quad \forall ij \in \mathcal{L} | \mathcal{L}_{ij}^{\text{T}} = 0, c \in \mathcal{C} \quad (4.4)$$

$$V_{j,c}^{\text{sqr}} I_{ij,c}^{\text{sqr}} = P_{ij,c}^2 + Q_{ij,c}^2, \quad \forall ij \in \mathcal{L}, c \in \mathcal{C} \quad (4.5)$$

$$P_{ij,c}^2 + Q_{ij,c}^2 \leq \overline{S}_{ij}^2, \quad \forall ij \in \mathcal{L}, c \in \mathcal{C} \quad (4.6)$$

$$Q_{\text{abs},i,c}^{\text{WT}} \leq Q_{i,c}^{\text{WT}} \leq Q_{\text{inj},i,c}^{\text{WT}}, \quad \forall i \in \mathcal{B} | \mathcal{B}_i^{\text{T}} = 2, c \in \mathcal{C} \quad (4.7)$$

$$\underline{V}_i^2 \leq V_{i,c}^{\text{sqr}} \leq \overline{V}_i^2, \quad \forall i \in \mathcal{B} | \mathcal{B}_i^{\text{T}} \neq 3, c \in \mathcal{C} \quad (4.8)$$

$$Q_{i,1}^{\text{sh}} = 0 \text{ and } Q_{i,2}^{\text{sh}} = B_i^{\text{sh}} V_{i,2}^{\text{sqr}}, \quad \forall i \in \mathcal{B} | \mathcal{B}_i^{\text{T}} \neq 3 \quad (4.9)$$

Block (A.2): Transformers equipped with NLTC

$$a_{ij}^{\text{NLTC}} = 1 + R_{ij}^{\%} \left[\frac{n_{ij}}{2\overline{n}} \right], \quad \forall ij \in \mathcal{L} | \mathcal{L}_{ij}^{\text{T}} = 1, n_{ij} \in \mathbb{Z} | -\overline{n}_{ij} \leq n_{ij} \leq \overline{n}_{ij} \quad (4.10)$$

$$(a_{ij}^{\text{NLTC}})^2 V_{i,c}^{\text{sqr}} - V_{j,c}^{\text{sqr}} = 2(R_{ij} P_{ij,c} + X_{ij} Q_{ij,c}) + Z_{ij}^2 I_{ij,c}^{\text{sqr}}, \quad \forall ij \in \mathcal{L} | \mathcal{L}_{ij}^{\text{T}} = 1, c \in \mathcal{C} \quad (4.11)$$

$$a_{ij}^{\text{NLTC}} = 1 + R_{\text{WT}}^{\%} \left[\frac{n_{ij}}{2\overline{n}_{\text{WT}}} \right], \quad \forall ij \in \mathcal{G}, n_{ij} \in \mathbb{Z} | -\overline{n}_{ij} \leq n_{ij} \leq \overline{n}_{ij} \quad (4.12)$$

$$V_{j,c}^{\text{sqr}} = (a_{ij}^{\text{NLTC}})^2 V_{i,c}^{\text{sqr}}, \quad \forall ij \in \mathcal{G}, c \in \mathcal{C} \quad (4.13)$$

$$V_{j,c}^{\text{sqr}} = (a_{ij}^{\text{NLTC}})^2 V_{\text{LV},j,c}^{\text{sqr}}, \quad \forall j \in \mathcal{B} | \mathcal{B}_j^{\text{T}} = 2, c \in \mathcal{C} \quad (4.14)$$

$$\underline{V}_j^2 \leq V_{\text{LV},j,c}^{\text{sqr}} \leq \overline{V}_j^2, \quad \forall j \in \mathcal{B} | \mathcal{B}_j^{\text{T}} = 2, c \in \mathcal{C} \quad (4.15)$$

Block (A.3): Main transformer equipped with OLTC

$$a_{ij,c}^{\text{OLTC}} = 1 + R^{\%} \left[\frac{n_{ij,c}}{2\bar{n}} \right], \quad \forall ij \in \mathcal{L} | \mathcal{L}_{ij}^T = 2, c \in \mathcal{C}, n_{ij} \in \mathbb{Z} | -\bar{n}_{ij} \leq n_{ij} \leq \bar{n}_{ij} \quad (4.16)$$

$$\left(a_{ij,c}^{\text{OLTC}} \right)^2 V_{i,c}^{\text{sqr}} - V_{j,c}^{\text{sqr}} = 2(R_{ij}P_{ij,c} + X_{ij}Q_{ij,c}) + Z_{ij}^2 I_{ij,c}^{\text{sqr}}, \quad \forall ij \in \mathcal{L} | \mathcal{L}_{ij}^T = 2, c \in \mathcal{C} \quad (4.17)$$

Block (A.4): Point of common coupling (PCC)

$$P_c^{\text{PCC}} + \sum_{ji \in \mathcal{L} | \mathcal{L}_{ij}^T \neq 0} P_{ji,c} - \sum_{ij \in \mathcal{L} | \mathcal{L}_{ij}^T \neq 0} (P_{ij,c} + R_{ij}I_{ij,c}^{\text{sqr}}) = 0, \quad \forall c \in \mathcal{C} \quad (4.18)$$

$$\underbrace{(3 - 2c)}_{\text{Inj/Abs}} Q_c^{\text{PCC}} + \sum_{ji \in \mathcal{L} | \mathcal{L}_{ij}^T \neq 0} Q_{ji,c} - \sum_{ij \in \mathcal{L} | \mathcal{L}_{ij}^T \neq 0} (Q_{ij,c} X_{ij} I_{ij,c}^{\text{sqr}}) = 0, \quad \forall c \in \mathcal{C} \quad (4.19)$$

$$Q_c^{\text{PCC}} \geq 0, \quad \forall c \in \mathcal{C} \quad (4.20)$$

The objective function in (4.1) maximizes the amount of reactive power injected/absorbed at the PCC, given by the two modes: $c = 1$ for reactive injection and $c = 2$ for absorption. Block (A.1) shows the AC branch model adapted from (Low; Farivar, 2013) and constraints (4.2) and (4.3) represent the active and reactive power balance at each node, respectively. Constraints (4.4) and (4.5) represent the calculation of the voltage magnitudes and the current magnitudes at each branch. Constraint (4.6) represents the capacity limits at every branch. Constraint (4.8) represents the square voltage magnitude limits. The reactive power capability of the individual WT units is given by inequality (4.7), $Q_{\text{inj},i,c}^{\text{WT}}$ and $Q_{\text{abs},i,c}^{\text{WT}}$ were defined in (3.12) and (3.13) respectively. Finally, (4.9) represents the availability of the capacitor banks, depending on the operation mode.

4.2.1.1 Transformers Equipped with NLTC

As shown in block (A.2), NLTC devices are typically equipped in the WT transformers. Constraint (4.10) and (4.12) calculates the voltage magnitude ratio depending on the tap-changer position for the main and WT transformers respectively, i.e., the discrete control variable n_{ij} , that is fixed once and maintained for every operation mode. Thus, constraints (4.11) and (4.13) represent the voltage drop within the transformer considering the tap-changer position. On the other hand, constraint (4.14) is analogue to (4.13) for WT feeders, where $V_{\text{LV}}^{\text{sqr}}$ is the square value of the voltage magnitude at the LV side of the WT's transformer. Finally, constraint (4.15) represents the voltage magnitude limits of V_{LV} used to assess the reactive power limits via (4.21)–(4.24).

4.2.1.2 Main Transformer Equipped with OLTC

In block (A.3), the main transformer of the WPP is typically equipped with OLTC. Such mechanism can modify the voltage magnitude ratio of the transformer for every operation mode, i.e., the discrete control variable $n_{ij,c}$ can change for each operation mode. In this case, constraint (4.16) calculates the voltage magnitude ratio and constraint (4.17) represents the voltage magnitude drop at the transformer.

4.2.1.3 Point of Common Coupling

In block (A.5), the active and reactive power balance equations at the PCC are given by (4.18) and (4.19). The term $(3 - 2c)$ in (4.19) computes the operation mode, i.e., if the WPP is injecting reactive power, then $c = 1$, and; if the WPP is absorbing, then $c = 2$, and in both cases the term Q_c^{PCC} must be guaranteed to be positive (4.20).

Note that the formulation for this optimization problem (4.1)–(4.20) is non-convex and difficult to be solved analytically. Besides, the number of equations and the number of variables are not equal, hence there will be no single solution, on the contrary, there will be one or more local solutions, without guaranteeing the optimal global solution. This ORPC initial model, could be solved by solver KNITRO (BYRD; NOCEDAL; WALTZ, 2006) in mathematical modeling languages such as AMPL (R. Fourer and D. M. Gay and B. W. Kernighan, 2003) or JuMP (KWON, 2016).

In order to avoid the uncertainty in obtaining the optimal global solution in MINLP models, the original formulation must be conveniently transformed using relaxation, approximation, or linearization methodologies, thus guaranteeing an optimal global solution for this new formulation, being this very close to the solution of the original formulation with a lower computational burden. In the following subsection, approximation and linearization techniques will be applied in order to solve the ORPC's initial model.

4.3 Linearization of the ORPC's Initial Model

In this section, we will explore linearization and approximation techniques in order to convert the ORPC initial problem from the MINLP to the MILP model.

4.3.1 Linearization of the Type-4 WT Reactive Power Capability

The limits for reactive power production at the LV side of the WT transformer is determined by constraint (4.7), where $Q_{\text{inj},i,c}^{\text{WT}}$ and $Q_{\text{abs},i,c}^{\text{WT}}$ are determined by Equations (3.2)–(3.3) and (3.10)–(3.11). Where (3.2)–(3.3) represent the limits of reactive power production due to the current magnitude limits \bar{I}_c , and (3.10)–(3.11) represent the limits of reactive power production due to the voltage magnitude limits at the GSC converter \bar{V}_c and \underline{V}_c (see subsection 3.2). These limits are illustrated in Fig. 4.1a.

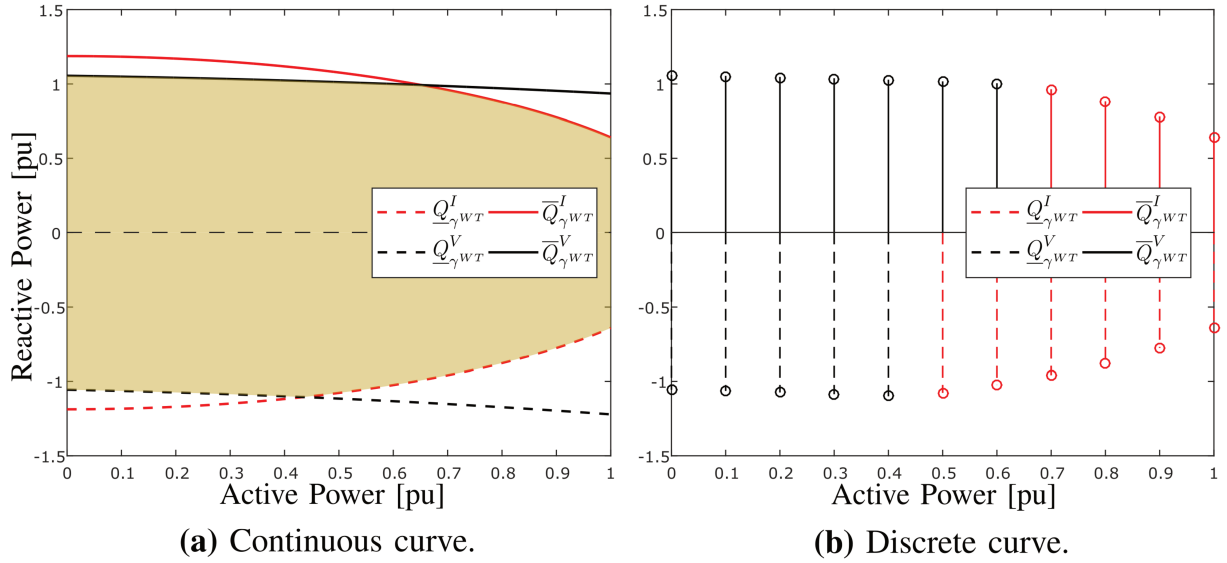


Figure 4.1 – WT power capability curve: a) voltage-limited and current-limited capability curve, b) Discrete limits for different levels of wind generation

Given an arbitrary value of $V_{LV} = 0.95$ pu, Fig. 4.1a shows the limits of reactive power injection for $P^{WT} = [0.0, 1.0]$ pu, using constraint (4.7). For $P^{WT} = \{0.0, 0.1, \dots, 0.9, 1.0\}$ pu, Fig. 4.1b shows the discrete version of the reactive power limits. The intersection area between the curves represents the reactive power capability of an individual WT feeder.

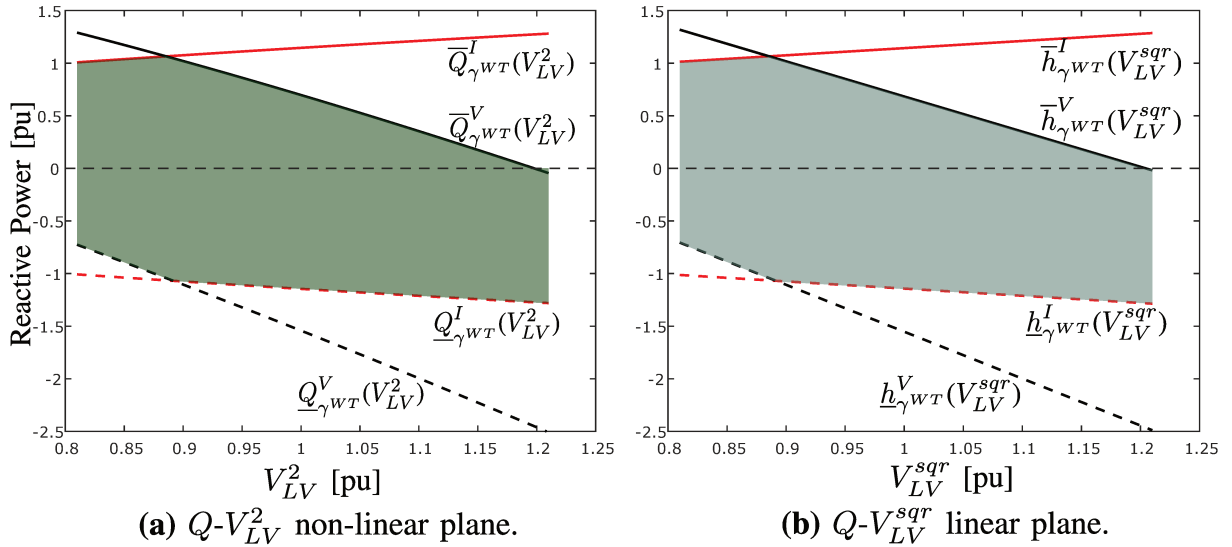


Figure 4.2 – Reactive power capability - voltage at LV side WT transformer limited by voltage and current by the GSC converter.

The limits for reactive power production are nonlinear and depend on the values of V_{LV} and P^{WT} . To linearize them, the first step is to consider a discrete set of wind power production scenarios $\gamma^{WT} \in \Gamma^{WT}$. Thus, as depicted in Fig. 4.1b, P^{WT} becomes a parameter. For each scenario $\gamma^{WT} \in \Gamma^{WT}$, the limits of reactive power production will only depend on the value of V_{LV}^2 . Fig. 4.2a shows the capability limits for $V_{LV}^2 = [0.81, 1.21]$ pu² and scenario $\gamma^{WT} | P^{WT} = 0.5$ pu. As shown in Fig. 4.2b, these curves can be efficiently

represented by linear functions with a change of variables $V_{LV}^2 \equiv V_{LV}^{\text{sqr}}$, whose coefficients can be obtained via Taylor series expansion.

The area within the polytope in Fig. 4.2b represents the linearized reactive power capability of the WT unit. Thus, for given Taylor polynomial parameters $\bar{\alpha}_{\gamma\text{WT}}^I$, $\underline{\alpha}_{\gamma\text{WT}}^I$, $\bar{\alpha}_{\gamma\text{WT}}^V$, $\underline{\alpha}_{\gamma\text{WT}}^V$, $\bar{\beta}_{\gamma\text{WT}}^I$, $\underline{\beta}_{\gamma\text{WT}}^I$, $\bar{\beta}_{\gamma\text{WT}}^V$ and $\underline{\beta}_{\gamma\text{WT}}^V$; the reactive power limits of each WT can be obtained using (4.21)–(4.24) for each wind power production scenario γ^{WT} . The expressions of the Taylor coefficients are shown in Appendix D.

$$\bar{h}_{\gamma\text{WT}}^I(V_{LV}^{\text{sqr}}) = \bar{\alpha}_{\gamma\text{WT}}^I V_{LV}^{\text{sqr}} + \bar{\beta}_{\gamma\text{WT}}^I \quad (4.21)$$

$$\underline{h}_{\gamma\text{WT}}^I(V_{LV}^{\text{sqr}}) = \underline{\alpha}_{\gamma\text{WT}}^I V_{LV}^{\text{sqr}} + \underline{\beta}_{\gamma\text{WT}}^I \quad (4.22)$$

$$\bar{h}_{\gamma\text{WT}}^V(V_{LV}^{\text{sqr}}) = \bar{\alpha}_{\gamma\text{WT}}^V V_{LV}^{\text{sqr}} + \bar{\beta}_{\gamma\text{WT}}^V \quad (4.23)$$

$$\underline{h}_{\gamma\text{WT}}^V(V_{LV}^{\text{sqr}}) = \underline{\alpha}_{\gamma\text{WT}}^V V_{LV}^{\text{sqr}} + \underline{\beta}_{\gamma\text{WT}}^V \quad (4.24)$$

Finally, constraints of reactive power production of each WT is given by (4.25) and (4.26).

$$\underline{h}_{\gamma\text{WT}}^I(V_{LV}^{\text{sqr}}) \leq Q_{\gamma\text{WT}}^{\text{WT}} \leq \bar{h}_{\gamma\text{WT}}^I(V_{LV}^{\text{sqr}}) \quad (4.25)$$

$$\underline{h}_{\gamma\text{WT}}^V(V_{LV}^{\text{sqr}}) \leq Q_{\gamma\text{WT}}^{\text{WT}} \leq \bar{h}_{\gamma\text{WT}}^V(V_{LV}^{\text{sqr}}) \quad (4.26)$$

4.3.2 Linearization of the Voltage Magnitude Regulation

In order to solve the ORPC using a MILP solver, the integer variable n_{ij} in (4.10) and (4.12) developed in block (A.2) for transformers equipped with NLTC, can be represented by a set of variables $v_{ij,w}^{\text{NLTC}}$ as shown in Equations (4.27)–(4.28) and (4.33)–(4.34) from block (B.1) and (B.2) for main and WT transformers respectively. The square of variable a_{ij}^{NLTC} is expressed in (4.29) and (4.35). The regulated voltage is given by (4.30) and (4.36), having a product between a continuous and binary variable $V_{j,c}^{\text{sqr}} v_{ij,w}^{\text{NLTC}}$. This term can be linearized with a disjunctive formulation in (4.31)–(4.32) and (4.37)–(4.38) for main and WT transformers respectively. Analogously, the integer variable $n_{ij,c}$ in (4.16) developed in block (A.3) for a main transformer equipped with OLTC, can be represented by a set of variables $v_{ij,c,w}^{\text{OLTC}}$ as shown in equations (4.39)–(4.40) from block (B.3). The square of variable $a_{ij,c}^{\text{OLTC}}$ is expressed in (4.41). The regulated voltage is given by (4.42), having a product between a continuous and a binary variable $V_{j,c}^{\text{sqr}} v_{ij,c,w}^{\text{OLTC}}$. This term can be linearized with a disjunctive formulation in (4.43) and (4.44), see (Macedo et al., 2015).

Block (B.1): Linear voltage magnitude regulation for NLTC main transformer.

$$\sum_{w=0}^{2\bar{n}} v_{ij,w}^{\text{NLTC}} = 1, \quad \forall ij \in \mathcal{L} | \mathcal{L}_{ij}^{\text{T}} = 1, v_{ij,w}^{\text{NLTC}} \in \{0, 1\} \quad (4.27)$$

$$a_{ij}^{\text{NLTC}} = 1 + R^{\%} \sum_{w=0}^{2\bar{n}} \left[\frac{(w - \bar{n}) v_{ij,w}^{\text{NLTC}}}{\bar{n}} \right], \quad \forall ij \in \mathcal{L} | \mathcal{L}_{ij}^{\text{T}} = 1, v_{ij,w}^{\text{NLTC}} \in \{0, 1\} \quad (4.28)$$

$$\left(a_{ij}^{\text{NLTC}}\right)^2 = \sum_{w=0}^{2\bar{n}} \left[\left(1 + R\% \frac{(w - \bar{n})}{\bar{n}}\right)^2 v_{ij,w}^{\text{NLTC}} \right], \quad \forall ij \in \mathcal{L} | \mathcal{L}_{ij}^T = 1, v_{ij,w}^{\text{NLTC}} \in \{0, 1\} \quad (4.29)$$

$$\left(a_{ij}^{\text{NLTC}}\right)^2 V_{j,c}^{\text{sqr}} = \sum_{w=0}^{2\bar{n}} \left[\left(1 + R\% \frac{(w - \bar{n})}{\bar{n}}\right)^2 V_{ij,c}^c \right], \quad \forall ij \in \mathcal{L} | \mathcal{L}_{ij}^T = 1, V_{ij,c}^c = v_{ij,w}^{\text{NLTC}} V_{j,c}^{\text{sqr}} \quad (4.30)$$

$$\underline{V}_i^2 (1 - v_{ij,w}^{\text{NLTC}}) \leq V_{j,c}^{\text{sqr}} - V_{ij,c}^c \leq \bar{V}_i^2 (1 - v_{ij,w}^{\text{NLTC}}), \quad \forall ij \in \mathcal{L} | \mathcal{L}_{ij}^T = 1, c \in \mathcal{C}, w = 0 \dots 2\bar{n} \quad (4.31)$$

$$\underline{V}_j^2 v_{ij,w}^{\text{NLTC}} \leq V_{ij,c}^c \leq \bar{V}_j^2 v_{ij,w}^{\text{NLTC}}, \quad \forall ij \in \mathcal{L} | \mathcal{L}_{ij}^T = 1, c \in \mathcal{C}, w = 0 \dots 2\bar{n} \quad (4.32)$$

Block (B.2): Linear voltage magnitude regulation for WT transformer.

$$\sum_{w=0}^{2\bar{n}_{\text{WT}}} v_{ij,w}^{\text{NLTC}} = 1, \quad \forall ij \in \mathcal{G}, v_{ij,w}^{\text{NLTC}} \in \{0, 1\} \quad (4.33)$$

$$a_{ij}^{\text{NLTC}} = 1 + R_{\text{WT}}\% \sum_{w=0}^{2\bar{n}_{\text{WT}}} \left[\frac{(w - \bar{n}_{\text{WT}}) v_{ij,w}^{\text{NLTC}}}{\bar{n}_{\text{WT}}} \right], \quad \forall ij \in \mathcal{G}, v_{ij,w}^{\text{NLTC}} \in \{0, 1\} \quad (4.34)$$

$$\left(a_{ij}^{\text{NLTC}}\right)^2 = \sum_{w=0}^{2\bar{n}_{\text{WT}}} \left[\left(1 + R_{\text{WT}}\% \frac{(w - \bar{n}_{\text{WT}})}{\bar{n}_{\text{WT}}}\right)^2 v_{ij,w}^{\text{NLTC}} \right], \quad \forall ij \in \mathcal{G}, v_{ij,w}^{\text{NLTC}} \in \{0, 1\} \quad (4.35)$$

$$\left(a_{ij}^{\text{NLTC}}\right)^2 V_{j,c}^{\text{sqr}} = \sum_{w=0}^{2\bar{n}_{\text{WT}}} \left[\left(1 + R_{\text{WT}}\% \frac{(w - \bar{n}_{\text{WT}})}{\bar{n}_{\text{WT}}}\right)^2 V_{ij,c}^c \right], \quad \forall ij \in \mathcal{G} | V_{ij,c}^c = v_{ij,w}^{\text{NLTC}} V_{j,c}^{\text{sqr}} \quad (4.36)$$

$$\underline{V}_i^2 (1 - v_{ij,w}^{\text{NLTC}}) \leq V_{j,c}^{\text{sqr}} - V_{ij,c}^c \leq \bar{V}_i^2 (1 - v_{ij,w}^{\text{NLTC}}), \quad \forall ij \in \mathcal{G}, c \in \mathcal{C}, w = 0 \dots 2\bar{n}_{\text{WT}} \quad (4.37)$$

$$\underline{V}_j^2 v_{ij,w}^{\text{NLTC}} \leq V_{ij,c}^c \leq \bar{V}_j^2 v_{ij,w}^{\text{NLTC}}, \quad \forall ij \in \mathcal{G}, c \in \mathcal{C}, w = 0 \dots 2\bar{n}_{\text{WT}} \quad (4.38)$$

Block (B.3): Linear voltage magnitude regulation for OLTC main transformer.

$$\sum_{w=0}^{2\bar{n}} v_{ij,c,w}^{\text{OLTC}} = 1, \quad \forall ij \in \mathcal{L} | \mathcal{L}_{ij}^T = 2, c \in \mathcal{C}, v_{ij,c,w}^{\text{OLTC}} \in \{0, 1\} \quad (4.39)$$

$$a_{ij,c}^{\text{OLTC}} = 1 + R\% \sum_{w=0}^{2\bar{n}} \left[\frac{(w - \bar{n}) v_{ij,c,w}^{\text{OLTC}}}{\bar{n}} \right], \quad \forall ij \in \mathcal{L} | \mathcal{L}_{ij}^T = 2, c \in \mathcal{C}, v_{ij,c,w}^{\text{OLTC}} \in \{0, 1\} \quad (4.40)$$

$$\left(a_{ij,c}^{\text{OLTC}}\right)^2 = \sum_{w=0}^{2\bar{n}} \left[\left(1 + R\% \frac{(w - \bar{n})}{\bar{n}}\right)^2 v_{ij,c,w}^{\text{OLTC}} \right], \quad \forall ij \in \mathcal{L} | \mathcal{L}_{ij}^T = 2, c \in \mathcal{C}, v_{ij,c,w}^{\text{OLTC}} \in \{0, 1\} \quad (4.41)$$

$$\left(a_{ij,c}^{\text{OLTC}}\right)^2 V_{j,c}^{\text{sqr}} = \sum_{w=0}^{2\bar{n}} \left[\left(1 + R\% \frac{(w - \bar{n})}{\bar{n}}\right)^2 V_{ij,c}^c \right], \quad \forall ij \in \mathcal{L} | \mathcal{L}_{ij}^T = 2, V_{ij,c}^c = v_{ij,c,w}^{\text{OLTC}} V_{j,c}^{\text{sqr}} \quad (4.42)$$

$$\underline{V}_i^2 (1 - v_{ij,c,w}^{\text{OLTC}}) \leq V_{j,c}^{\text{sqr}} - V_{ij,c}^c \leq \bar{V}_i^2 (1 - v_{ij,c,w}^{\text{OLTC}}), \quad \forall ij \in \mathcal{L} | \mathcal{L}_{ij}^T = 2, c \in \mathcal{C}, w = 0 \dots 2\bar{n} \quad (4.43)$$

$$\underline{V}_j^2 v_{ij,c,w}^{\text{OLTC}} \leq V_{ij,c}^c \leq \bar{V}_j^2 v_{ij,c,w}^{\text{OLTC}}, \quad \forall ij \in \mathcal{L} | \mathcal{L}_{ij}^T = 2, c \in \mathcal{C}, w = 0 \dots 2\bar{n} \quad (4.44)$$

4.3.3 Linear Approximation of the AC Power Flow

Constraint (4.5) has two types of nonlinearities: a product between two variables ($V_{j,c}^{\text{sqr}} I_{ij,c}^{\text{sqr}}$) and the sum of two squared variables ($P_{ij,c}^2 + Q_{ij,c}^2$). Thus, Equation (4.45) is the approximation of $V_{j,c}^{\text{sqr}} I_{ij,c}^{\text{sqr}}$, where the squared voltage magnitude $V_{j,c}^{\text{sqr}}$ is approximate to the squared constant voltage value $(V'_{j,c})^2$, as shown in 4.4.1.2. Additionally, Equation (4.46) approximates the term $P_{ij,c}^2 + Q_{ij,c}^2$ via the piecewise linearization function (Lin et al., 2013). This function uses a set of discretization blocks, as in (4.46)–(4.53), where $\Delta_{ij}^S = V^n I_{ij}^{\text{max}} / Y$, $m_{ij,y}^s = (2y - 1)\Delta_{ij}^S$. The piecewise linearization of terms $P_{ij,c}^2$ and $Q_{ij,c}^2$ is illustrated in Fig. 4.3. Therefore, constraint (4.5) can be represented by a linearized approximation as shown (4.54). (see subsection 2.3.2).

Block C.1: Linear approximation of the AC power flow

$$V_{j,c}^{\text{sqr}} I_{ij,c}^{\text{sqr}} \approx (V'_{j,c})^2 I_{ij,c}^{\text{sqr}}, \quad \forall ij \in \mathcal{L}, c \in \mathcal{C} \quad (4.45)$$

$$P_{ij,c}^2 + Q_{ij,c}^2 \approx \sum_{y=1}^Y m_{ij,y}^s \Delta_{ij,y,c}^P + \sum_{y=1}^Y m_{ij,y}^s \Delta_{ij,y,c}^Q, \quad \forall ij \in \mathcal{L}, c \in \mathcal{C} \quad (4.46)$$

$$P_{ij,c}^+ - P_{ij,c}^- = P_{ij,c}, \quad \forall ij \in \mathcal{L}, c \in \mathcal{C} \quad (4.47)$$

$$Q_{ij,c}^+ - Q_{ij,c}^- = Q_{ij,c}, \quad \forall ij \in \mathcal{L}, c \in \mathcal{C} \quad (4.48)$$

$$P_{ij,c}^+ + P_{ij,c}^- = \sum_{y=1}^Y \Delta_{ij,y,c}^P, \quad \forall ij \in \mathcal{L}, c \in \mathcal{C} \quad (4.49)$$

$$Q_{ij,c}^+ + Q_{ij,c}^- = \sum_{y=1}^Y \Delta_{ij,y,c}^Q, \quad \forall ij \in \mathcal{L}, c \in \mathcal{C} \quad (4.50)$$

$$P_{ij,c}^+, P_{ij,c}^-, Q_{ij,c}^+, Q_{ij,c}^- \geq 0 \quad \forall ij \in \mathcal{L}, c \in \mathcal{C} \quad (4.51)$$

$$0 \leq \Delta_{ij,y,c}^P \leq \Delta_{ij}^S, \quad \forall ij \in \mathcal{L}, y \in Y, c \in \mathcal{C} \quad (4.52)$$

$$0 \leq \Delta_{ij,y,c}^Q \leq \Delta_{ij}^S, \quad \forall ij \in \mathcal{L}, y \in Y, c \in \mathcal{C} \quad (4.53)$$

$$(V'_{j,c})^2 I_{ij,c}^{\text{sqr}} = \sum_{y=1}^Y m_{ij,y}^s \Delta_{ij,y,c}^P + \sum_{y=1}^Y m_{ij,y}^s \Delta_{ij,y,c}^Q, \quad \forall ij \in \mathcal{L}, c \in \mathcal{C} \quad (4.54)$$

The MILP formulation to solve the ORPC's initial model is given by (4.55).

$$\begin{cases} \max (4.1) \\ \text{s.t.: } (4.2)–(4.4), (4.8)–(4.9), (4.11), (4.15), (4.17)–(4.20), \\ \text{and } (4.25)–(4.54). \end{cases} \quad (4.55)$$

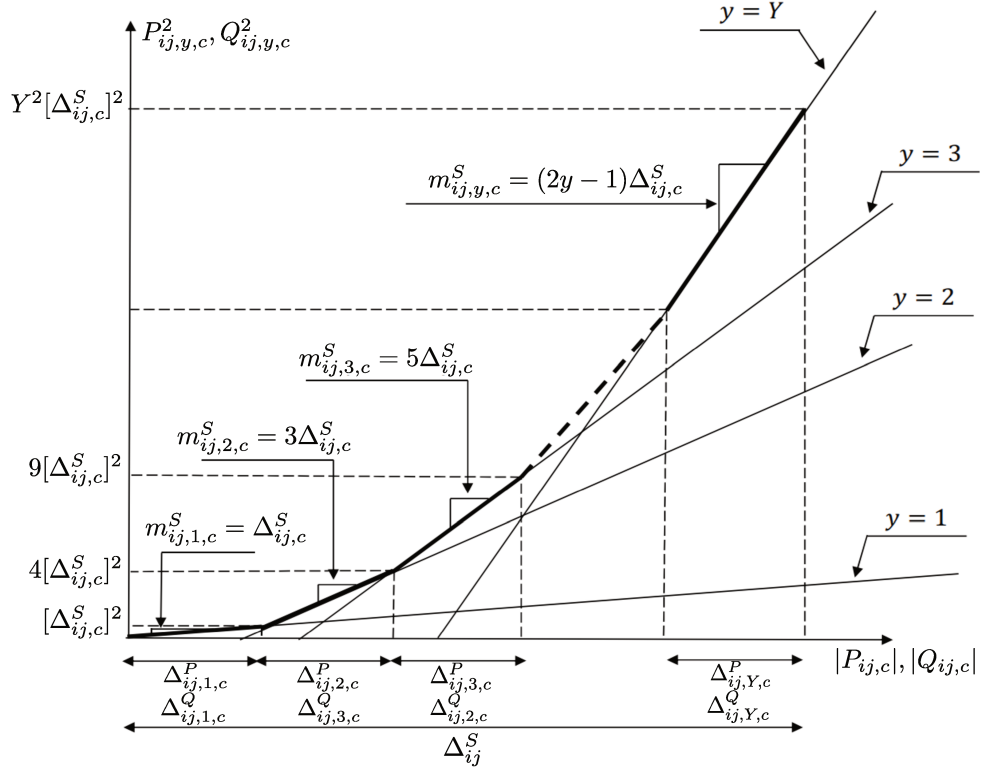


Figure 4.3 – Piecewise linearization function for terms $P_{ij,c}^2$ and $Q_{ij,c}^2$.

Note that the MILP formulation (4.55) is an approximation of the original ORPC initial model in (4.1)–(4.20). This MILP formulation, can be adequately solved by solver CPLEX (IBM ILOG, 2009), mathematical modeling languages such as AMPL (R. Fourer and D. M. Gay and B. W. Kernighan, 2003) or JuMP (KWON, 2016).

In order to obtain the full ORPC model, specific scenarios must be added (wind power production and voltage magnitude at PCC). Note that the list of PCC voltage magnitude level scenarios (Γ^{PCC}) and wind power production levels (Γ^{WT}) require an associated probability of occurrence that can be obtained via historical analysis or statistical inference. These specific scenarios will be introduced in the initial ORPC model and are described in the next section.

4.4 ORPC Model Including Specified Scenarios

The ORPC problem in (4.1)–(4.20) is defined for two operation modes: reactive absorption and injection. However, the wind power produced by each WT unit and the voltage magnitude at the PCC are unknown parameters. Thus, two sets of finite scenarios for both parameters are defined by Γ^{WT} and Γ^{PCC} . In this case, each wind power production level and its probability are given by $\gamma^{\text{WT}} \cdot \bar{P}_i^{\text{WT}}$ and \wp^{WT} , $\forall(\gamma^{\text{WT}}, \wp^{\text{WT}}) \in \Gamma^{\text{WT}}$. Moreover, each voltage magnitude at the PCC and its probability are given by $\gamma^{\text{PCC}} \cdot V^n$ and \wp^{PCC} , $\forall(\gamma^{\text{PCC}}, \wp^{\text{PCC}}) \in \Gamma^{\text{PCC}}$.

These sets of scenarios can be merged into one set \mathcal{K} , whose elements k_1 and k_2 result from the Cartesian product between Γ^{WT} and Γ^{PCC} , as shown in (4.56).

$$\mathcal{K} = \Gamma^{\text{WT}} \times \Gamma^{\text{PCC}} = \left\{ \underbrace{(\gamma^{\text{WT}}, \gamma^{\text{PCC}})}_{k_1}, \underbrace{(\wp^{\text{WT}}, \wp^{\text{PCC}})}_{k_2} \mid (\gamma^{\text{WT}}, \wp^{\text{WT}}) \in \Gamma^{\text{WT}}, (\gamma^{\text{PCC}}, \wp^{\text{PCC}}) \in \Gamma^{\text{PCC}} \right\} \quad (4.56)$$

Scenarios in Γ^{WT} and Γ^{PCC} will strongly depend on the characteristics of each particular WPP under study. Considering that both scenarios are unrelated, the probability of each element k_1 is the product between \wp^{WT} and \wp^{PCC} , as shown in (4.57).

$$\Upsilon_{k_2} = \wp^{\text{WT}} \times \wp^{\text{PCC}} \quad (4.57)$$

Thus, the objective function (4.1) must be modified as in (4.58), where Υ_{k_2} represents the weight of each scenario in the objective function.

$$\max \quad \mathbf{f}_1 = \sum_{(k_1, k_2) \in \mathcal{K}} \sum_{c \in C} \Upsilon_{k_2} Q_{c, k_1}^{\text{PCC}} \quad (4.58)$$

Finally, the variables used in (4.1)–(4.20) and the subsequent linearizations must be modified as shown in Table 4.1. Note that the tap settings of the transformers equipped with NLTC do not depend on the scenario k_1 , since they remain constant for every possible realization of \mathcal{K} .

Table 4.1 – Modified variables considering the set of scenarios \mathcal{K} .

Initial Model	Include \mathcal{K}	Initial Model	Include \mathcal{K}	Initial Model	Include \mathcal{K}
$P_{ij,c}$	P_{ij,c,k_1}	$Q_{ij,c}$	Q_{ij,c,k_1}	$V_{i,c}^{\text{sqr}}$	V_{i,c,k_1}^{sqr}
$P_{i,c}^{\text{WT}}$	P_{i,c,k_1}^{WT}	$Q_{i,c}^{\text{WT}}$	Q_{i,c,k_1}^{WT}	$I_{ij,c}^{\text{sqr}}$	$I_{ij,c,k_1}^{\text{sqr}}$
P_c^{PCC}	P_{c,k_1}^{PCC}	Q_c^{PCC}	Q_{c,k_1}^{PCC}	$Q_{i,c}^{\text{sh}}$	Q_{i,c,k_1}^{sh}
$\Delta_{ij,y,c}^P$	Δ_{ij,y,c,k_1}^P	$\Delta_{ij,y,c}^Q$	Δ_{ij,y,c,k_1}^Q	$V_{\text{LV},i,c}^{\text{sqr}}$	$V_{\text{LV},i,c,k_1}^{\text{sqr}}$
$P_{ij,c}^+$	P_{ij,c,k_1}^+	$P_{ij,c}^-$	P_{ij,c,k_1}^-	$a_{ij,c}^{\text{OLTC}}$	$a_{ij,c,k_1}^{\text{OLTC}}$
$Q_{ij,c}^+$	Q_{ij,c,k_1}^+	$Q_{ij,c}^-$	Q_{ij,c,k_1}^-	$v_{ij,c,w}^{\text{OLTC}}$	$v_{ij,c,k_1,w}^{\text{OLTC}}$

4.4.1 Proposed MILP Model

Considering the set of linearizations of the previous subsection 4.3 including specified scenarios, the proposed MILP model to solve the ORPC problem is given by (4.59).

$$\begin{cases} \max (4.58) \\ \text{s.t.: } (4.2)–(4.4), (4.8)–(4.9), (4.11), (4.15), (4.17)–(4.20), \\ \text{and } (4.25)–(4.54). \end{cases} \quad (4.59)$$

Note that the proposed MILP model (4.59) is an approximation of the original ORPC full model in (4.1)–(4.20). Additionally, the change of variables shown in Table 4.1 is included due to the set of scenarios Γ^{WT} and Γ^{PCC} . This formulation presents a low error rate, as was verified in Chapter 5.

The analysis of the computational complexity between the complete MINLP and MILP model and the description of the solution strategy of the proposed MILP model, in order to solve the ORPC problem (Full Model), will be developed in the following subsections:

4.4.1.1 Computational Complexity of the Proposed Models

The MINLP model for the ORPC problem can be solved with mixed-integer non-linear commercial solvers. However, MINLP solvers are poorly scalable and they cannot guarantee an optimal solution in reasonable time. On the other hand, the proposed MILP model (4.59) has a better computational complexity. As shown in (Mhanna; Verbič; Chapman, 2016), the use of piece-wise functions for linearizing the optimal power flow is computationally very efficient and accurate, despite the fact that a larger number of continuous variables is required. Table 4.2 summarizes the computational complexity for the proposed ORPC problem using the developed models, where \mathbf{n}^n is the number of transformers equipped with NLTC and \mathbf{n}^o is the number of transformers equipped with OLTC. Note that the number of continuous variables of the MILP is increased by a factor of $|\mathbf{Y}|$, given by the number of discretization blocks. However, the number of binary variables remains the same.

Table 4.2 – Computational complexity of the MINLP and the MILP model

MINLP Model	Size	Complexity Order
Binary variables	$(\mathbf{n}^n + \mathbf{n}^o \mathcal{K} \mathcal{C})(2\bar{n}_{ij} + 1)$	$ \mathcal{K} \bar{n}_{ij}$
Continuous variables	$(3 \mathcal{B} + 3 \mathcal{L} + 2) \mathcal{K} \mathcal{C} $	$ \mathcal{L} \mathcal{K} $
Equality constraints	$(3 \mathcal{B} + 3 \mathcal{L} - 3\mathbf{n}^n + 1) \mathcal{K} \mathcal{C} + \mathbf{n}^n$	$ \mathcal{L} \mathcal{K} $
Inequality constraints	$(3 \mathcal{B} + \mathbf{n}^o + 1) \mathcal{K} \mathcal{C} + \mathbf{n}^n$	$ \mathcal{B} \mathcal{K} $
MILP Model	Size	Complexity Order
Binary variables	$(\mathbf{n}^n + \mathbf{n}^o \mathcal{K} \mathcal{C})(2\bar{n}_{ij} + 1)$	$ \mathcal{K} \bar{n}_{ij}$
Continuous variables	$(3 \mathcal{B} + \mathcal{L} (5 + 2 \mathbf{Y}) + 2) \mathcal{K} \mathcal{C} $	$ \mathbf{Y} \mathcal{L} \mathcal{K} $
Equality constraints	$(3 \mathcal{B} + 3(2 \mathcal{L} - \mathbf{n}^n) + 1) \mathcal{K} \mathcal{C} + \mathbf{n}^n$	$ \mathbf{Y} \mathcal{L} \mathcal{K} $
Inequality constraints	$(3 \mathcal{B} + \mathbf{n}^o + \mathcal{L} (4 + 2 \mathbf{Y}) + 1) \mathcal{K} \mathcal{C} + \mathbf{n}^n$	$ \mathbf{Y} \mathcal{L} \mathcal{K} $

4.4.1.2 Solution Strategy

This subsection describes the step-by-step process used to solve the ORPC problem with the proposed MILP model (4.59). Essentially, this strategy is required to obtain a suitable value for $V'_{j,c}$, in the product $(V'_{j,c})^2 I_{ij,c}^{\text{sq}}r$ that appears in (4.54):

- *Step one:* Consider a initial value of V'_{j,c,k_1} equal the nominal voltage value V^n . Then, solve the ORPC with the integrality of $v_{ij,w}^{\text{NLTC}}$ and $v_{ij,c,k_1,w}^{\text{OLTC}}$ relaxed. Hence, the MILP

becomes a linear programming problem and the voltage magnitude values for each node in the found solution are used to fix V'_{j,c,k_1} .

- *Step two:* Solve the ORPC considering the estimated value of V'_{j,c,k_1} and the binary nature of $v_{ij,w}^{\text{NLTC}}$ and $v_{ij,c,k_1,w}^{\text{OLTC}}$.
- *Step three:* Validate the results with an AC-PF.

4.5 Final Comments

The linearization method of the limits of the reactive power capability of a Type-4 WT using the Taylor decomposition was presented. This procedure is detailed in section 4.3.1. In addition, the discrete control model of the tap-changer of the transformers equipped with NLTC and OLTC and capacitor bank are presented as decision variables. Furthermore, the terms of operation mode and uncertain scenarios (their respective probability) were introduced – all of them in order to obtain the proposed MILP model to solve the ORPC problem.

The proposed model (4.59) can be very useful for estimating RPC in real-time operation. To achieve this, it must be ensured that the tap settings are constant. In the next chapter, performance, accuracy, and computational time will be evaluated with the methodologies described in Chapter 3. Therefore the methodology developed in this chapter can be used to estimate the RPC (real-time operation) and ORPC (Planning stage) of the Type-4 WT based WPP.

5 Simulations and Results

5.1 Introduction

In this chapter, the results obtained with the methodology described in Chapter 4 are presented. The simulations are focused on two aspects: real-time operation and planning stage. The real-time operation approach aims to obtain the RPC of the Type-4 based WPP, considering the only operational limits of the collector system and the WTs. The WT transformer taps are fixed and scenarios are not taken into account. On the other hand, the planning stage approach aims to obtain optimal WPP tap setting considering all the operational constraints as well as the probabilities for the different specified scenarios (wind power generation level at WTs, voltage magnitude level at SE/PCC node and operation mode). Both proposed approaches are evaluated considering two test systems: A small WPP with seven WTs in string and the Burbo Bank WPP with twenty-five WTs (Sarkar et al., 2019).

The rest of the chapter is organized as follows: Section 5.2 presents the estimated RPC for a Type-4 based WPP in a real-time operation using the three proposed approaches found in the literature (see Chapter 3) and the proposed methodology. Finally, Section 5.3 presents the ORPC obtained for a Type-4 based WPP in the planning stage using the proposed methodology, exploring the accuracy, efficiency, and RPC increases obtained among the case studies.

5.2 Real-time Operation

In real-time, the WPP has already been commissioned, which means the taps of the NLTC transformers are already fixed as well as active power production is known (total wind). The operation of the WPP is conducted considering the boundaries of the components, in order to avoid equipment damage. As a result, only the boundaries of the WPP components and mode of operation are considered in the optimal power flow problem. This clearly simplifies the problem when compared with the planning stage.

In this section we will explore the accuracy, efficiency, and computational burden of the three proposed approaches found in the literature described in Section 3.3. The obtained results will be compared to the methodology proposed in this dissertation for the following test systems: A Small WPP and Burbo Bank WPP systems from (Sarkar et al., 2019) (electrical data are presented in Appendix C). The models were implemented in Julia Language (version 1.4.0) using the optimization package JuMP (version 0.19) (KWON, 2016), the AC-PF-MO with the non-commercial solver IPOPT (version 8.1.0.56, with default settings) (Yoshiaki Kawajir, 2015) and the proposed method is solved with the commercial solver CPLEX (version 12.8.0, with default settings) (IBM ILOG, 2009). The simulations were done in a notebook with a 2.20 GHz Intel Core i7-2670 processor and 8 GB of RAM. The specific scenarios Γ^{WT} and Γ^{SE} considered for this section are shown in (5.1). Besides, the voltage magnitude at the LV side of the WT transformer is maintained constant at 1.0 pu by the tap-changer ($a = 1$). In addition, the number of blocks of the piecewise linearization was $Y = 30$.

$$\begin{aligned}\Gamma^{\text{WT}} &= \{0.0 \quad 0.1 \quad 0.2 \quad \dots \quad 0.8 \quad 0.9 \quad 1.0\} \quad [\text{pu}] \\ \Gamma^{\text{SE}} &= \{0.95 \quad 0.98 \quad 1.0 \quad 1.02 \quad 1.05\} \quad [\text{pu}]\end{aligned}\tag{5.1}$$

5.2.1 A Small WPP with 7 WTs

The small WPP layout system from (Sarkar et al., 2019) is showed in Fig. 5.1, comprising 7 WT feeders each of 2.0 MW in string, whose electrical data and limits are presented in Appendix C. The WTs are operating with nominal voltage magnitude 0.69 kV on the LV-side and 34.5 kV on the HV-side of the WT transformer, i.e. collection grid voltage or voltage at the LV side of the main transformer.

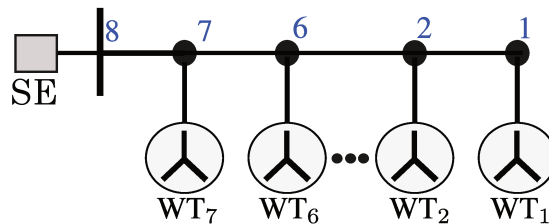


Figure 5.1 – Small WPP system layout with 7 WT feeders.

The estimated RPC for the small WPP system evaluated at different voltage levels Γ^{SE} on the reference bus $V_{\text{LV}}^{\text{SE}}$ using the methods studied in Chapter 3 and the proposed model are shown in Fig. 5.2.

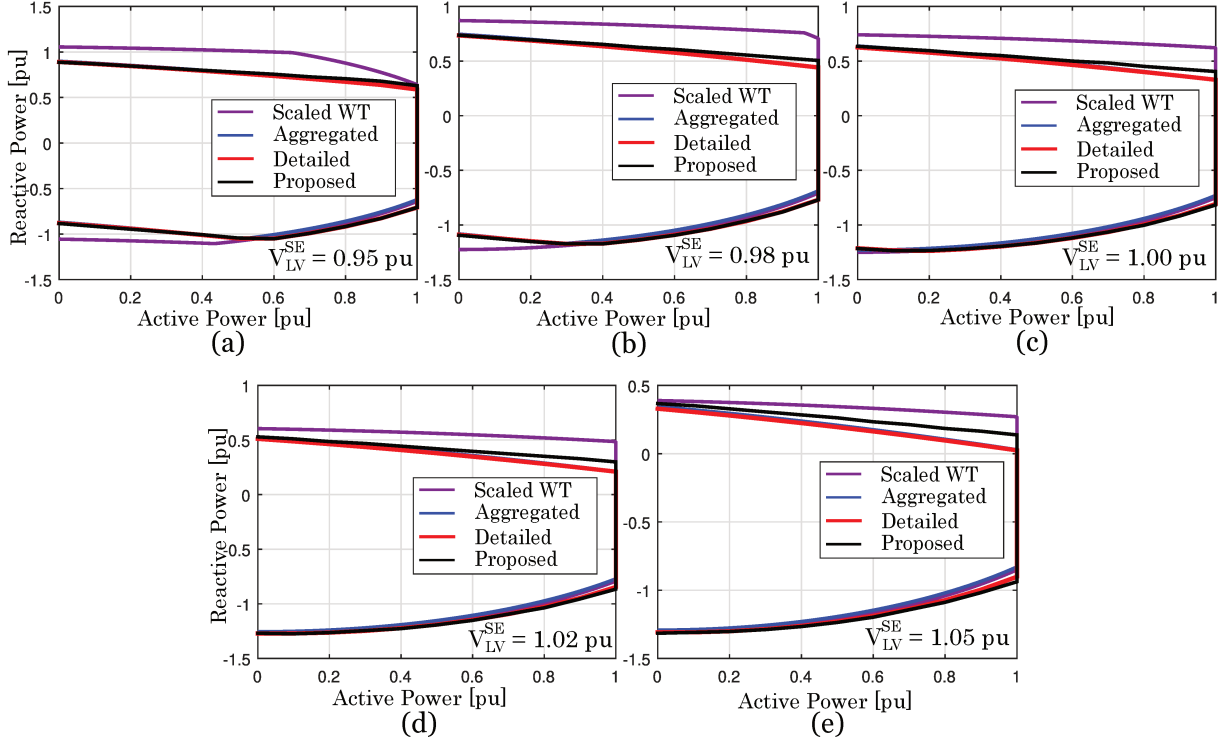


Figure 5.2 – Small WPP system RPC estimation using different methods.

From Fig. 5.2, the results obtained with the proposed model show a slight additional reactive power injection with respect to the other, as the magnitude voltage $V_{\text{LV}}^{\text{SE}}$ is increasing. This behavior is due to the main advantages of the proposed model based on an optimization problem, thus obtaining optimal operating points that allow increasing the reactive power capacity in PCC. In addition, the magnitude voltages at the buses are considered variables. As a result, they present a slightly higher reactive power in the injection mode compared to the aggregate model due to the susceptance of the WPP collection grid.

5.2.1.1 Performance Indexes

In order to evaluate the precision of the results by the methodology developed in Sections 3.3 and 4.3, they are compared with the RPC obtained using the base method (detailed WPP method). The accuracy criterion is the average Root Mean Square Error (RMSE) defined by the following expression (5.2):

$$\text{RMSE} = \sqrt{\frac{\sum_{\gamma^{\text{WT}}} (Q_{c,\gamma^{\text{WT}}}^{\text{SE}}_{\text{detailed}} - Q_{c,\gamma^{\text{WT}}}^{\text{SE}}_{\text{calculated}})^2}{|\Gamma^{\text{WT}}|}} \quad \forall c \in \mathcal{C}, \gamma^{\text{WT}} \in \Gamma^{\text{WT}} \quad (5.2)$$

Where, $Q_{c,\gamma^{\text{WT}}}^{\text{SE}}_{\text{detailed}}$ is reactive power calculated by base method at operation mode c , scenario for the γ^{WT} ; $Q_{c,\gamma^{\text{WT}}}^{\text{SE}}_{\text{calculated}}$ is the reactive power calculated using the others RPC

models at operation mode c , scenario γ^{WT} . The average RMSE is calculated as the average of RMSE errors across number of voltage levels of the set Γ^{SE} . For the small WPP system, the RMSE and the average RMSE calculated are shown in Table 5.1. Note that the calculation of the average RMSE is done in p.u. units using the base power of 14 MVA.

Table 5.1 – RMSE of calculated reactive power for the small WPP system.

Model		RMSE (Mvar)					Average	
		V = 0.95	V = 0.98	V = 1	V = 1.02	V = 1.05	Mvar	p.u.
Scaled WT	Inj.	2.8489	3.1236	2.9433	2.6833	2.2724	2.774	0.198
	Abs.	1.3638	0.8648	0.4262	0.3764	0.3536	0.677	0.048
Aggregated	Inj.	0.0851	0.1111	0.1311	0.1511	0.1807	0.131	0.009
	Abs.	0.6035	0.6122	0.6211	0.6145	0.6002	0.610	0.043
Proposed	Inj.	0.3179	0.4555	0.5749	0.7387	1.0345	0.624	0.044
	Abs.	0.0514	0.0399	0.0559	0.1004	0.2002	0.089	0.006

The results in Table 5.1 show satisfactory accuracy of the proposed method, with an average RMSE of 4.4% and 0.6% for the injection and absorption operation mode, respectively. However, the aggregated method presents a closer approximation in the injection operation mode with an average RMSE value of 0.9%.

In order to determine the RPC overestimation/underestimation of the results obtained by the different methods regarding to the base method, we will use the percent area difference comparison (PADC) as validation criteria. PADC is defined by the following expression (5.3):

$$\text{PADC} = \frac{A_{\text{calculated}}^{c,\gamma^{\text{SE}}} - A_{\text{detailed}}^{c,\gamma^{\text{SE}}}}{A_{\text{detailed}}^{c,\gamma^{\text{SE}}}} \times 100 \quad \forall c \in \mathcal{C}, \gamma^{\text{SE}} \in \Gamma^{\text{SE}}. \quad (5.3)$$

Where $A_{\text{detailed}}^{c,\gamma^{\text{SE}}}$ and $A_{\text{calculated}}^{c,\gamma^{\text{SE}}}$ are the reactive power capability curve area obtained in the LV side of the main transformer using the base method (detailed WPP method) and the others respectively at operation mode c , scenario γ^{SE} . For the Small WPP system, the PADC and the average PADC are shown in Table 5.2.

Table 5.2 – PADC of plotted reactive power capability for the small WPP system.

Model		PADC (%)					Avg. (%)
		V = 0.95	V = 0.98	V = 1	V = 1.02	V = 1.05	
Scaled WT	Inj.	27.0423	36.7360	41.4180	49.0819	80.3468	46.9250
	Abs.	4.6462	0.5152	-1.4547	-1.6066	-1.4596	0.1281
Aggregated	Inj.	0.6169	1.1820	1.7922	2.8013	6.6949	2.6175
	Abs.	-2.9118	-3.0429	-3.2144	-3.3527	-3.1939	-3.1431
Proposed	Inj.	-2.6954	0.1343	3.4333	9.1679	33.6331	8.7346
	Abs.	-4.7575	-5.0125	-5.3427	-5.2247	-4.8482	-5.0371

Results in Table 5.2 shows an overestimation/underestimation calculated using the Scaling WT/Aggregate/Proposed methods, obtaining the highest average PADC of 46.93% (overestimation) with the scaled WT method in injection mode and a lowest average PADC of -5.04% (underestimation) with the proposed method in absorption mode.

5.2.1.2 RPC with Bounding

We present the RPC estimation curves including collector system limits such as loadability limits of the branches. The RPC curves for the Small WPP system are calculated at different voltage levels Γ^{SE} on the reference bus $V_{\text{LV}}^{\text{SE}}$ using the proposed method, shown in Fig. 5.3.

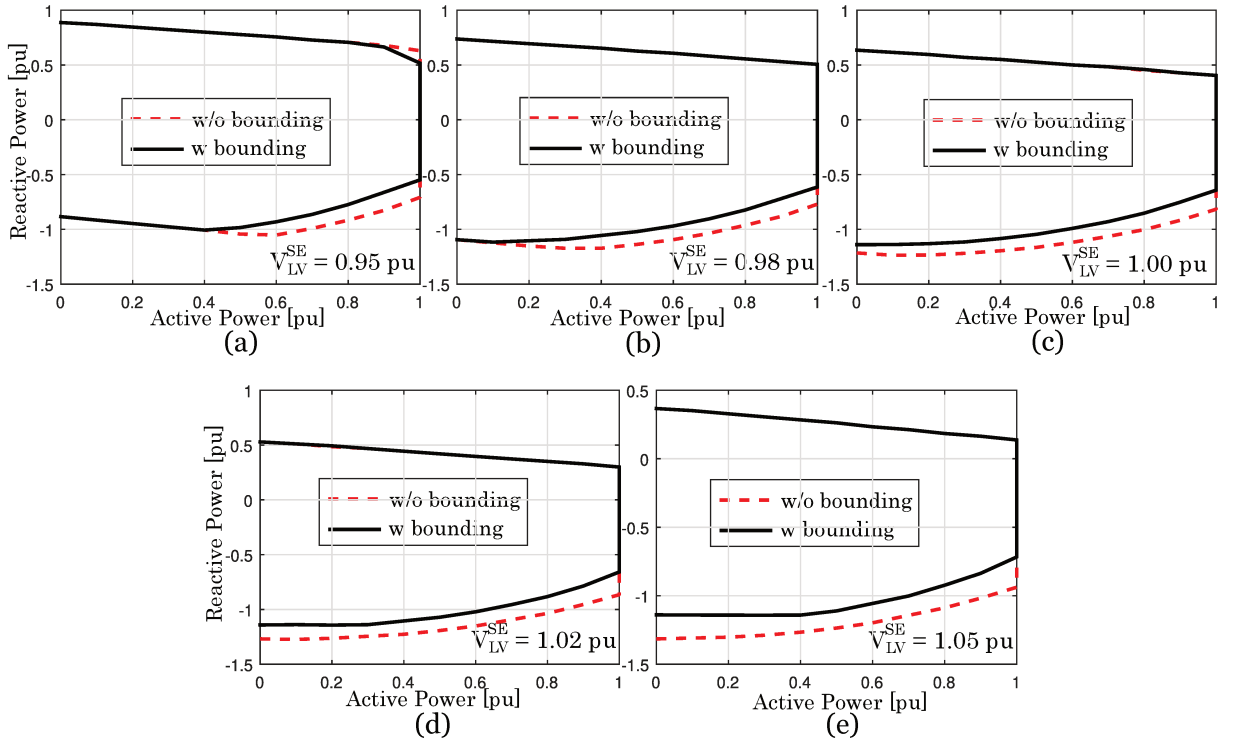


Figure 5.3 – Small WPP system RPC using the proposed method evaluated with and without collector system bounds.

From Fig. 5.3, the solid black line and dotted red line represent the RPC with/without including collector system limits, respectively. The results obtained considering the loadability limits in the branches show a decrease in reactive power absorption.

In order to determine the RPC overestimation/underestimation among the results obtained of the RPC estimation with collector system limits included and without them, we will use the modified PADC (PADC') as validation criteria. PADC' is defined by the following expression (5.4):

$$\text{PADC}' = \frac{A_{\text{w/o bounding}}^{c, \gamma^{\text{SE}}} - A_{\text{w bounding}}^{c, \gamma^{\text{SE}}}}{A_{\text{w bounding}}^{c, \gamma^{\text{SE}}}} \times 100 \quad \forall c \in \mathcal{C}, \gamma^{\text{SE}} \in \Gamma^{\text{SE}}. \quad (5.4)$$

Where $A_{w \text{ bounding}}^{c, \gamma^{SE}}$ and $A_{w/o \text{ bounding}}^{c, \gamma^{SE}}$, are RPC estimated curve areas considering/not-considering the collector system limits respectively at operation mode c , at scenario γ^{SE} . The $PADC'$ and the average $PADC'$ obtained for the Small WPP system are shown in Table 5.3.

Table 5.3 – $PADC'$ of plotted RPC curves for the Small WPP considering collector system bounding using the proposed method.

System		PADC' (%)					Avg. (%)
		V = 0.95	V = 0.98	V = 1	V = 1.02	V = 1.05	
Small WPP	Inj.	0.5258	0	-0.1433	-0.1870	0	0.0391
	w/o limits	7.1995	9.7740	11.4264	12.0800	13.3507	10.7661

The results in Table 5.3 show the RPC overestimation when the collector system limits are neglected. This is appreciable when the WPP operates in absorption mode resulting in an average $PADC'$ of 10.77%, whereas when the WPP operates in injection mode it is practically negligible, obtaining an average $PADC'$ of 0.03%.

5.2.2 Burbo Bank WPP

The Burbo Bank WPP system obtained from (Sarkar et al., 2019), situated in the west coast of UK, is a 90 MW WPP, whose topology is showed in Fig. 5.4, comprising 25 WT feeders each of 3.6 MW in string, whose electrical data and limits are presented in Appendix C. The WTs are operating with nominal voltage magnitude 0.69 kV on the LV-side and 34.5 kV on the HV-side of the WT transformer, i.e. collection grid voltage or voltage at the LV side of the main transformer.

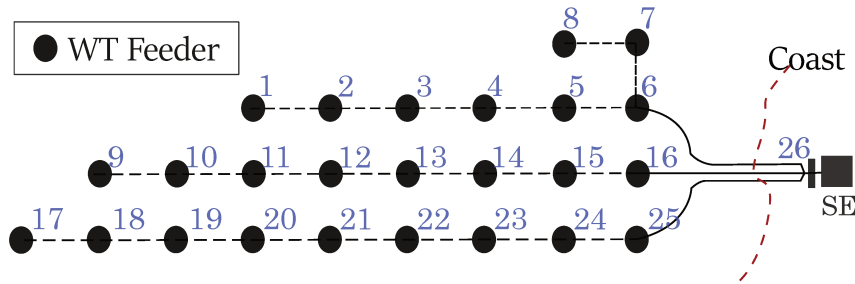


Figure 5.4 – Burbo Bank WPP system topology.

The reactive power capability for the Burbo Bank WPP system evaluated at different voltage levels V^{SE} on the reference bus V_{ref}^{SE} using the methods studied in this chapter is presented in Fig. 5.5.

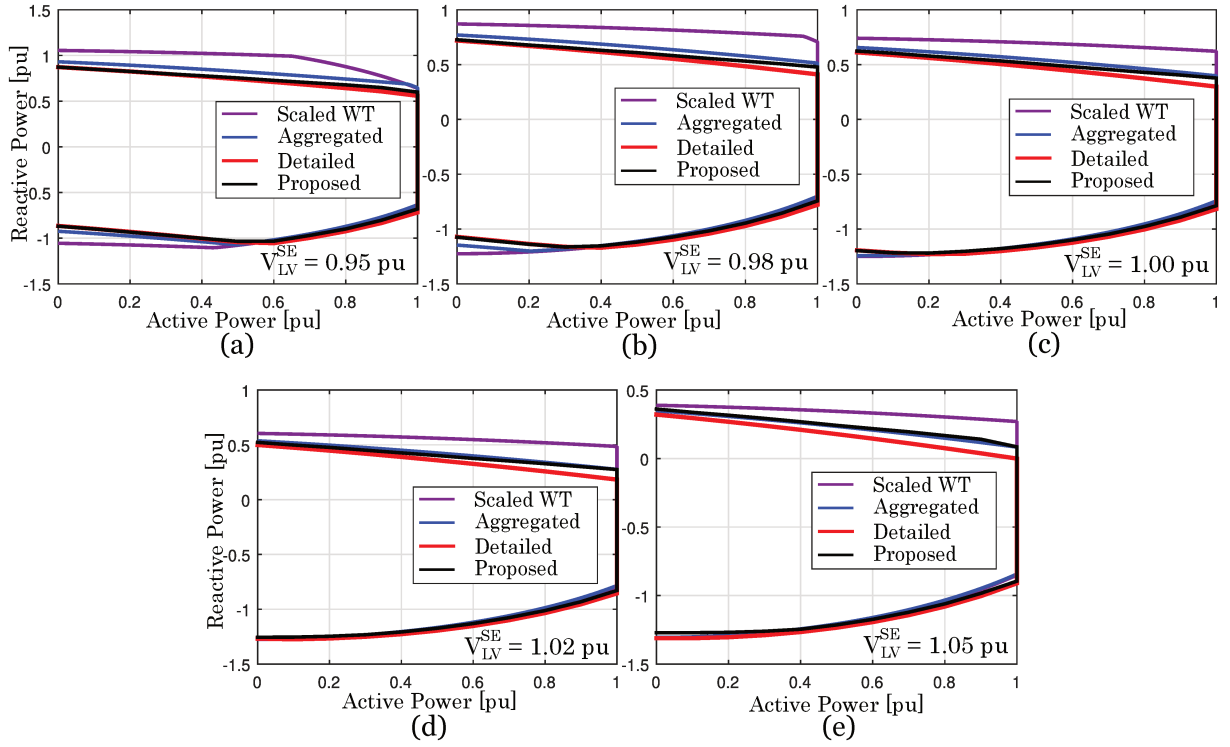


Figure 5.5 – Burbo Bank WPP system reactive power capability estimation using different methods.

From Fig. 5.5, the results obtained with the proposed method for a large WPP system present the best proximity to the detailed method with respect to the others. Like in the small WPP system, there is a slight additional reactive power injection with respect to the other, as the magnitude voltage V_{LV}^{SE} is increasing (see subsection 5.2.1).

5.2.2.1 Performance Indexes

In order to demonstrate the precision between the different methods with respect to the base method, the RMSE in (5.2) is used. The RMSE and average RMSE are shown in Table 5.4. Note that the calculation of the average RMSE is done in p.u. units using the base power of 90 MVA.

Table 5.4 – RMSE of calculated reactive power for Burbo Bank WPP system.

Model		RMSE (Mvar)					Average	
		V = 0.95	V = 0.98	V = 1	V = 1.02	V = 1.05	Mvar	p.u.
Scaled WT	Inj.	20.4414	22.1827	20.9000	19.0535	16.1257	19.740	0.219
	Abs.	9.5431	6.4285	3.4487	2.8852	2.7298	5.007	0.055
Aggregated	Inj.	7.5117	7.1218	6.6753	6.1707	5.3154	6.559	0.072
	Abs.	4.6466	4.8194	3.7608	3.3908	3.2639	3.976	0.044
Proposed	Inj.	2.0798	3.1436	3.8935	4.8581	6.3588	4.066	0.045
	Abs.	1.7796	1.9082	1.9601	1.9071	2.4300	1.997	0.022

The results in Table 5.4 show satisfactory accuracy of the proposed method, with the lowest average RMSE of 4.5% and 0.2% for injection and absorption operation mode,

respectively.

In order to demonstrate the RPC overestimation/underestimation between the different methods with respect to the base method, the PADC in (5.3) is used. The PADC and the average PADC are shown in Table 5.5.

Table 5.5 – PADC of plotted capability curves for Burbo Bank WPP system.

Model		PADC (%)					Avg. (%)
		V = 0.95	V = 0.98	V = 1	V = 1.02	V = 1.05	
Scaled WT	Inj.	31.3400	42.1311	47.8762	57.3093	97.1852	55.1684
	Abs.	4.8694	0.6569	-1.5087	-2.0039	-1.8719	0.0284
Aggregated	Inj.	11.5115	13.4194	15.4698	18.8473	32.8063	18.4109
	Abs.	-0.0194	-0.7336	-2.1230	-2.6113	-2.4751	-1.5925
Proposed	Inj.	-2.8613	0.4286	3.9763	9.9868	35.8942	9.4849
	Abs.	-6.4760	-6.8625	-7.4095	-7.5649	-7.7555	-7.2137

The results in Table 5.5 show an RPC overestimation/underestimation calculated using the proposed method, obtaining an average PADC of 9.48% (overestimation) and 7.21% (underestimation) in injection and absorption mode respectively.

Therefore, in this particular system, the proposed model obtains a better RPC estimated precision with respect to the others. Note that if the WPP operates in absorption mode the aggregated method presents a slightly larger error decreasing as the voltage magnitude increases. This is due to the fact that the reactive power generated by susceptance of the WPP collection grid is considered constant since the magnitude voltage at the buses is considered constant (see subsection 3.3.2.2). On the other hand, the results obtained using the scaled method present higher errors, thus reaching an average error of 55.168 Mvar in injection mode.

5.2.2.2 RPC with bounding

We present the RPC estimation curves including collector system limits, such as loadability limits of the branches. In this particular WPP system, the loadability in the branches-trunks was reduced by approximately 34% from the original value, in order to demonstrate the importance and advantage of the proposed model. The RPC curves for the Burbo Bank WPP system as calculated at different voltage levels Γ^{SE} on the reference bus $V_{\text{LV}}^{\text{SE}}$ using the proposed method are shown in Fig. 5.6. In addition, the RPC overestimation/underestimation among the results obtained from the RPC estimation with collector system limits included and without them are calculated using PADC' (5.4). The PADC' and the average PADC' are shown in Table 5.6.

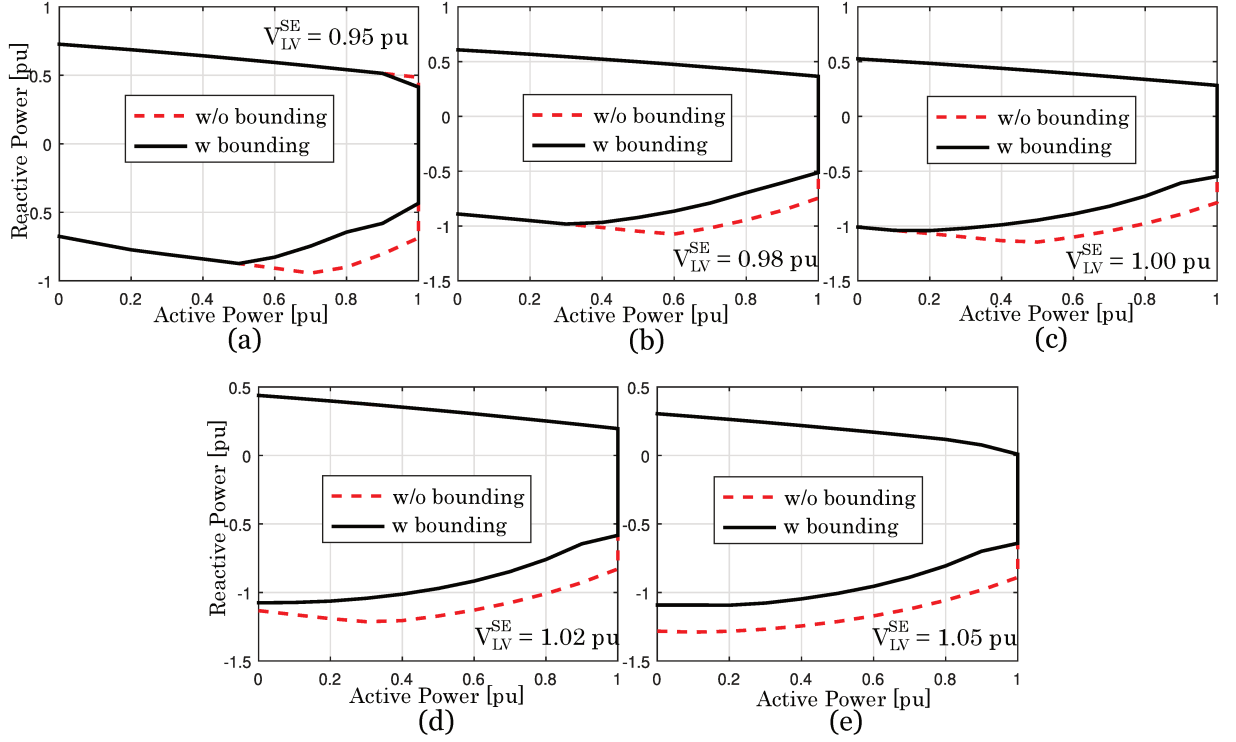


Figure 5.6 – Burbo Bank WPP system RPC using the proposed method evaluated with and without collector system bounds.

In Fig. 5.6, the solid black line and dotted red line represent the RPC with/without including collector system limits, respectively. The results obtained considering the loadability limits in the branches show a decrease in reactive power absorption.

Table 5.6 – PADC of plotted RPC curves for the Burbo Bank WPP system considering collector system bounding using the proposed method.

System		PADC (%)					Avg. (%)
		V = 0.95	V = 0.98	V = 1	V = 1.02	V = 1.05	
Burbo Bank	Inj.	0.3545	0.0000	0.0000	-0.0215	0.0000	0.0677
	w/o limits	Abs.	10.7432	13.5175	16.4181	19.5440	20.9823
							16.2410

The results in Table 5.6 show the RPC overestimation when the collector system limits are neglected. This is appreciable when the WPP operates in absorption mode resulting in an average PADC' of 16.24%. Whereas when the WPP operates in injection mode it is practically negligible, obtaining an average PADC' of 0.07%.

The results obtained using the proposed method were satisfactory for a small and large-scale WPP system, highlighting the main contribution of including the collector system limits for a more realistic estimation of the RPC in the WPP. In the next section, we will present the results of the computational time of the proposed method compared with others in order to validate the operation in real-time.

5.2.3 Assessment of the Computational Cost

The time required for obtaining maximum and minimum reactive power capability for each WPP system is summarized in Table 5.7. Each value is obtained with the accumulated times due to operating mode (\mathcal{C} : Injection and absorption), active power output of WT feeders (Γ^{WT}) and voltage level at the reference bus (Γ^{SE}). The times required to solve the Scaled WT and Aggregated methods are minimal, since the latter are reduced to simple solution algebraic problems. On the other hand, the time required to solve the RPC problem using the detailed method depends on the tolerance value due to the absolute maximum voltage error at operation mode c (see section 3.3.2). For this chapter, the value of this tolerance is 1×10^{-4} . The percentage average voltage errors ($V_{i,c}^k - V_{i,c}^{k-1}$) for each active power production level by WT feeder Γ^{WT} is shown in Fig. 5.7. Experimentally, to obtain each value, 440 simulations on average were performed for each WPP system ($|\Gamma^{\text{WT}}| \times |\Gamma^{\text{SE}}| \times |\mathcal{C}| \times \text{Iterations-Average} = 11 \times 5 \times 2 \times 4 = 440$). Finally, in the proposed method, the required time depends on the computational complexity, this includes the number of WTs and branches of the collecting system, number of blocks of the piecewise linearization Y and the number specified of considered scenarios (5.1).

Table 5.7 – Time needed to solve the RPC estimation models for each test system.

System	Computational Time (s)			
	Scaled WT	Detailed	Aggregated	Proposed
Small WPP	0.002	30.40	0.002	0.2
Burbo Bank WPP	0.002	50.70	0.002	0.2

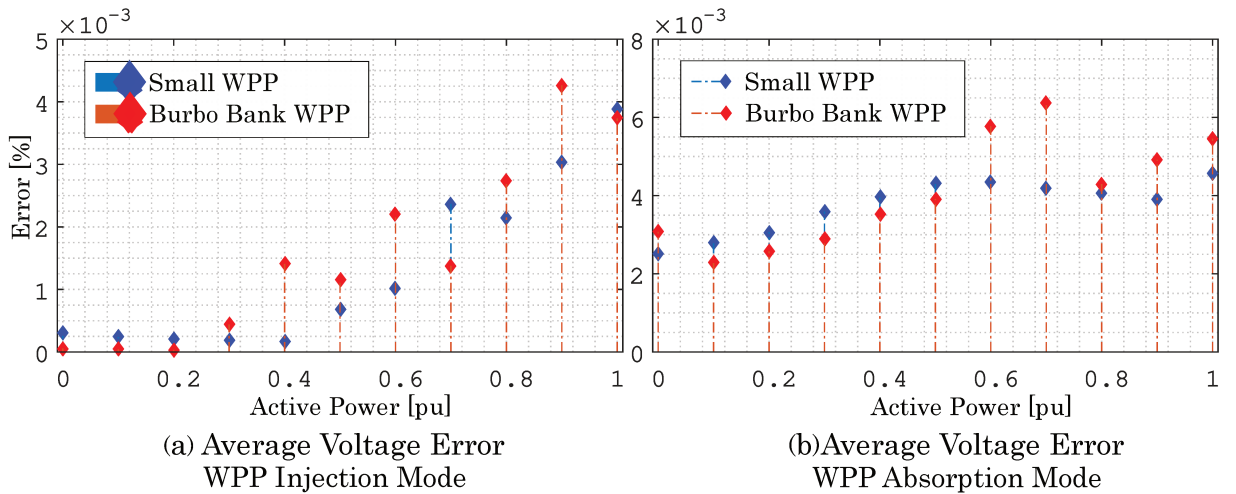


Figure 5.7 – Average voltage error percentage for each test system using the detailed model.

5.2.4 Discussion

The RPC in Type-4 based WPP for real-time operation is estimated by the proposed method (4.59). Achieving the following benefits: (a) The proposed method can be considered as the base method, since it includes operating and electrical limits in its formulation; (b) Convergence to optimality is guaranteed by LP commercial solvers; and, (c) It was verified that the proposed method is efficient, scalable, accurate and has less computation burden. Thus, it obtains the most realistic RPC estimation in two WPP systems with average RMSE of less than 4.5% for most cases, with computational times less than one second, being sufficient for real-time operation. Table 5.8 shows the rating of the methods used in the different features.

Table 5.8 – Methods comparison with rating

Features	Review			
	Scaled WT	Detailed	Aggregated	Proposed
Computational time*	1	4	1	2
Accuracy	4	-	2	1
Include limit constraints	4	4	4	1
Optimal RPC is obtained*	4	3	3	1

Rating notation: "1" is the best and "4" the worst

*For fixed tap changer value

5.3 Planning Stage

The definition of power system planning can be stated as: a process in which the aim is to decide on new as well as upgrading existing system elements to adequately satisfy the loads for a foreseen future (SEIFI; SEPASIAN, 2011).

In the present case, the system element is a generation facility (WPP), differently from operation, there are parameters that can only be set *a priori* in the planning stage. In case of the WPP, the tapping setting of all NLTC transformers must be chosen in the planning, because it cannot be changed in real time. Like any other planning study, the tapping setting of the NLTC transformers must be selected considering different probability scenarios that directly affect the size of the RPC of a particular WPP. These scenarios include the active power generation, voltage level at PCC node and operation mode.

In this section we explore the application of the proposed approach for the following test systems: Small WPP and Burbo Bank WPP systems from (Sarkar et al., 2019), adapted and used to demonstrate the efficiency of the proposed method, whose electrical data are presented in Appendix C. The proposed ORPC was implemented in the modeling language JuMP (version 0.65) (DUNNING; HUCHETTE; LUBIN, 2015) for mathematical optimization embedded in Julia (KWON, 2016) and solved using the commercial solver CPLEX (version 12.8.0.0, with default settings) (IBM ILOG, 2009). To analyze the precision of the results obtained with the proposed method, AC power flow was implemented on the same platform and solved using the non-commercial solver IPOPT (version 8.1.0.56, with default settings) (Yoshiaki Kawajir, 2015). The simulations were done in a notebook with a 2.20 GHz Intel Core i7-2670 processor and 8 GB of RAM. In addition, the number of blocks of the piecewise linearization was $Y = 30$. Scenarios used in this section for Γ^{WT} and Γ^{PCC} are shown in (5.5).

$$\Gamma^{\text{WT}} = \left\{ \begin{matrix} (\gamma^{\text{WT}} [\text{pu}], \phi^{\text{WT}}) \\ (0.0, 0.01) \\ (0.1, 0.01) \\ (0.2, 0.01) \\ (0.3, 0.01) \\ (0.4, 0.46) \\ (0.5, 0.45) \\ (0.6, 0.01) \\ (0.7, 0.01) \\ (0.8, 0.01) \\ (0.9, 0.01) \\ (1.0, 0.01) \end{matrix} \right\}; \quad \Gamma^{\text{PCC}} = \left\{ \begin{matrix} (\gamma^{\text{PCC}} [\text{pu}], \phi^{\text{PCC}}) \\ (0.95, 0.02) \\ (0.98, 0.92) \\ (1.00, 0.02) \\ (1.02, 0.02) \\ (1.05, 0.02) \end{matrix} \right\} \quad (5.5)$$

5.3.1 Case Studies

Three case studies are conducted in this section. They were chosen considering the typical operation and the tap-changer equipment of the transformers commonly installed in large WPP. Each case study is described below:

- Base case:** Nominal operation of all transformers, with a constant tap ratio given by $a_{ij} = 1$; It was considered as a base case, since until today the problem of obtaining the reactive power capability of a WPP is solved but is limited to considering the transformation relation as a parameter equal to 1.
- Case I:** Operation of all transformers as NLTC. In this case study, it is expected to obtain an increase in reactive power capability with respect to the base case with a unique combination of transformer tap changer regardless of any type of plausible scenario or operation mode.
- Case II:** Operation of all WTs transformers as NLTC and the main transformer as OLTC. Like case study I, it is expected to obtain an increase in reactive power capability compared to previous study cases. Unlike Case I, the main transformer is OLTC equipped. Consequently, a tap changer position will be determined for each plausible scenario and mode of operation.

5.3.2 Assessment Criterion

To compute the error of the proposed MILP model, the average root mean square error (RMSE) in Equation (5.6) is calculated. In this case, the reactive power flow at the PCC determined by an exact AC power flow $Q_{c,\gamma^{\text{WT}}_{\text{AC}}}^{\text{PCC}}$, and by the MILP model $Q_{c,\gamma^{\text{WT}}_{\text{MILP}}}^{\text{PCC}}$, at operation mode c , scenario γ^{WT} , are compared.

$$\text{RMSE} = \sqrt{\frac{\sum_{\gamma^{\text{WT}}} (Q_{c,\gamma^{\text{WT}}_{\text{AC}}}^{\text{PCC}} - Q_{c,\gamma^{\text{WT}}_{\text{MILP}}}^{\text{PCC}})^2}{|\Gamma^{\text{WT}}|}} \quad \forall c \in \mathcal{C}, \gamma^{\text{WT}} \in \Gamma^{\text{WT}} \quad (5.6)$$

To calculate the increase in reactive power capability, the difference between the capability curves obtained in Cases I and II, and the one obtained with the base case should be assessed via the percent area difference comparison (PADC) in Equation (5.7).

$$\text{PADC} = \frac{A_{\text{Case I/II}}^{c,\gamma^{\text{PCC}}} - A_{\text{Base case}}^{c,\gamma^{\text{PCC}}}}{A_{\text{Base case}}^{c,\gamma^{\text{PCC}}}} \times 100 \quad \forall c \in \mathcal{C}, \gamma^{\text{PCC}} \in \Gamma^{\text{PCC}}. \quad (5.7)$$

Where $A_{\text{Case I/II}}^{c,\gamma^{\text{PCC}}}$ and $A_{\text{Base case}}^{c,\gamma^{\text{PCC}}}$ are the capability curve areas obtained in the PCC at operation mode c , scenario γ^{PCC} , all of them are evaluated with an AC-PF. Note that the area of the capability curve is the space inside the boundary of the curve, being evaluated for each voltage magnitude level at PCC, as shown in Fig. 5.9.

5.3.3 A Small WPP with 7 WTs

The small WPP layout system is shown in Fig. 5.8, comprising 7 WT feeders in string, operating with nominal voltage magnitude 0.69 kV on the LV-side and 34.5 kV on the HV-side of the WT transformer, with a $\pm 10\%$ range around nominal voltage. The distances between the feeders is given by L_1 , and the distance from the WPP substation to the nearest WT feeder is given by L_2 . The WPP substation comprises a main transformer with a voltage ratio of 34.5/138 kV. The parameters of the WT feeders, the collector grid and the substation are presented in Appendix C.

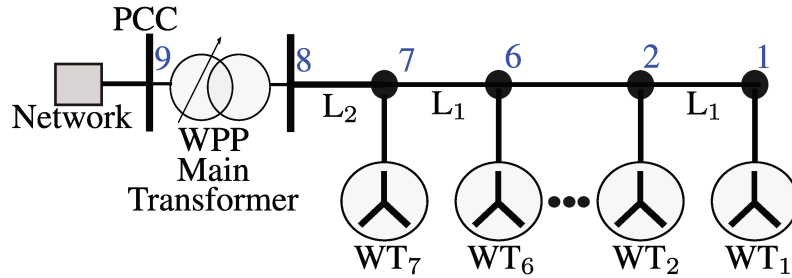


Figure 5.8 – Small WPP system layout with 7 WT feeders.

The reactive power capability curves obtained with the base/I/ II case studies considering different voltage levels γ^{PCC} at the PCC for the small WPP system are presented in Fig. 5.9–5.11. The dotted red line represents the results determined with the MILP model and the black line represents the capability curve obtained after running the exact AC-PF:

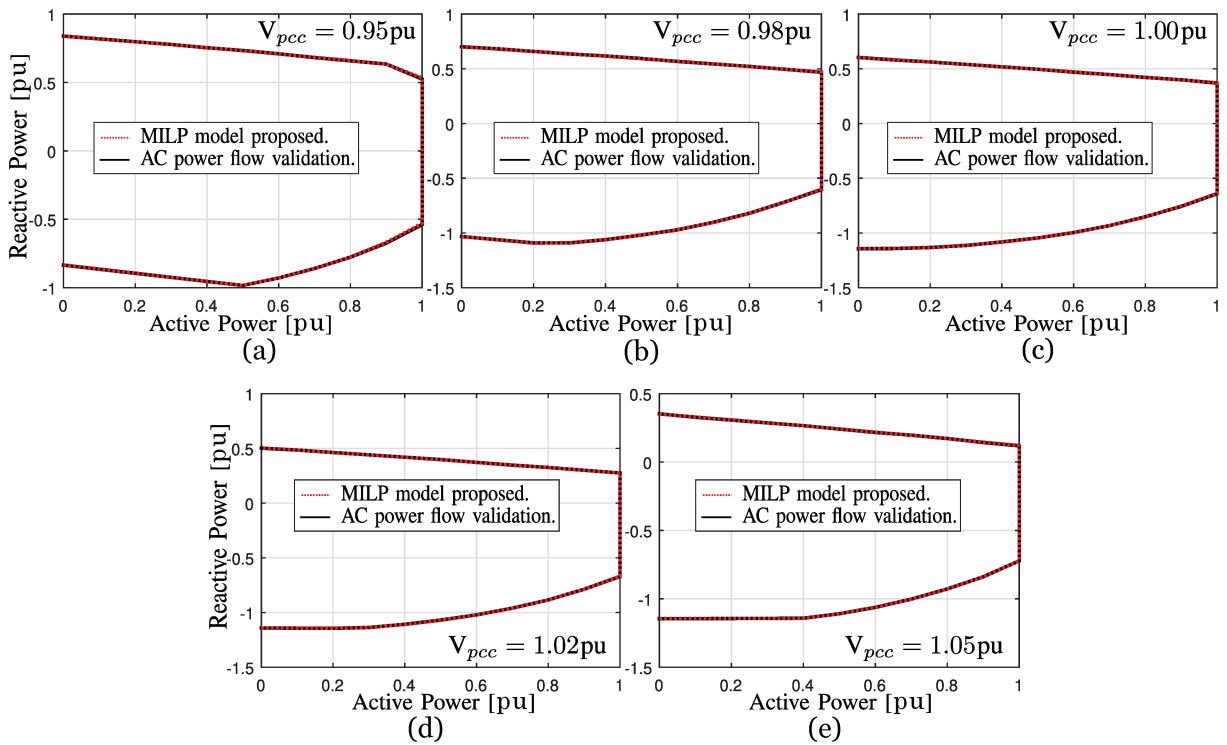


Figure 5.9 – Small WPP system reactive power capability using the MILP model and an exact AC-PF - Base case.

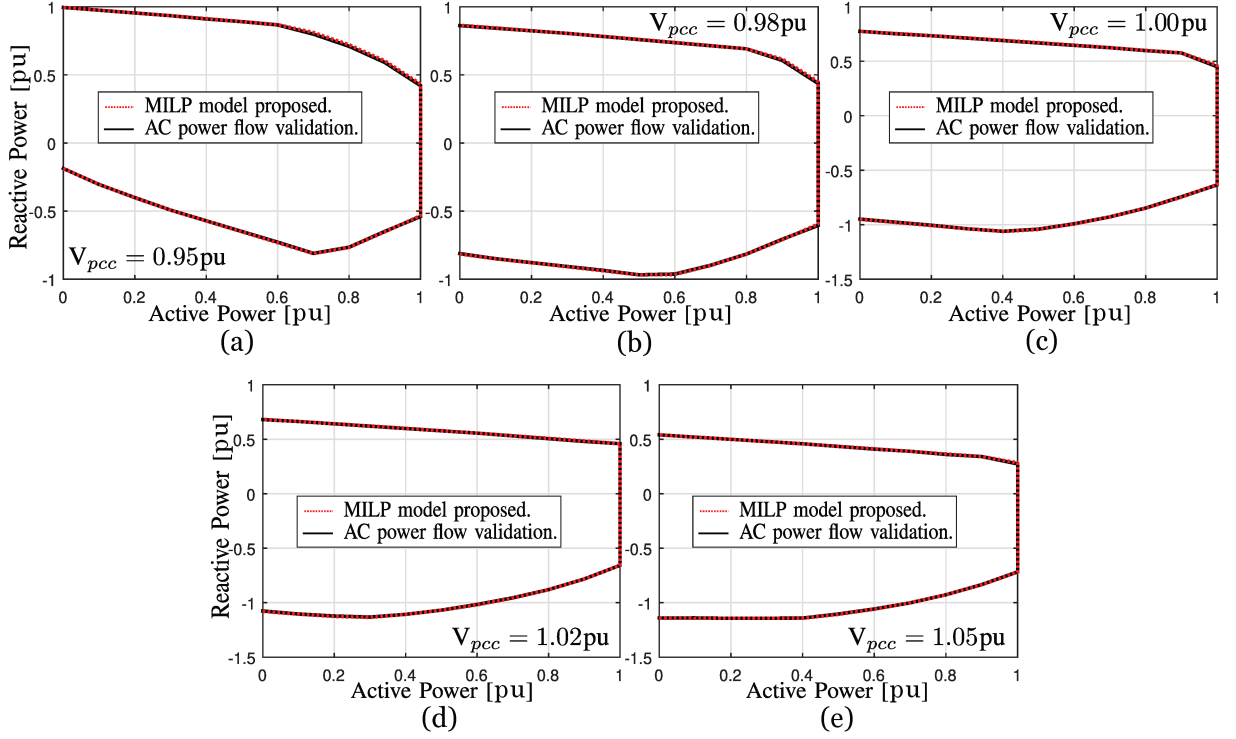


Figure 5.10 – Small WPP system reactive power capability using the MILP model and an exact AC-PF - Case I.

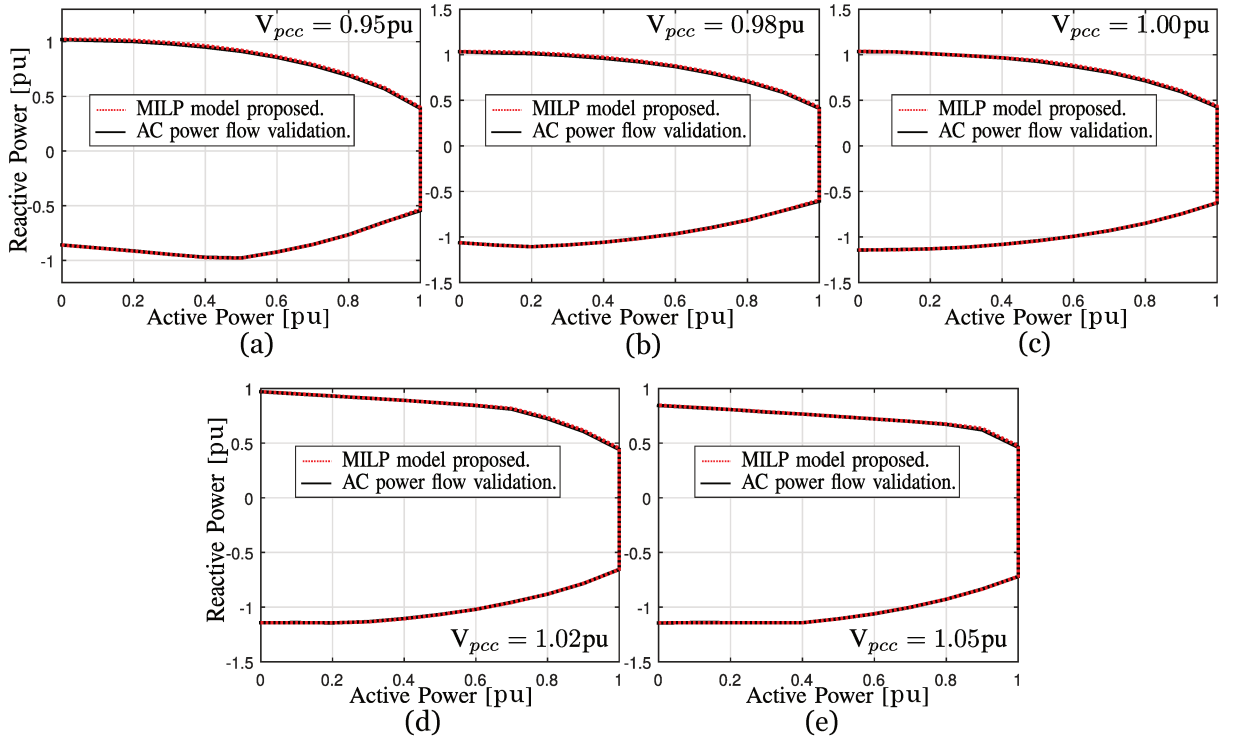


Figure 5.11 – Small WPP system reactive power capability using the MILP model and an exact AC-PF - Case II.

From Fig. 5.9–5.11, a great approximation of the proposed MILP model and the operating points obtained after running AC-PF can be observed. This demonstrates satisfactory accuracy of the MILP model, that is contrasted with the RMSE results in Table 5.9.

5.3.3.1 Accuracy Validation

In order to demonstrate the accuracy of the proposed MILP model (4.59), the RMSE in (5.6) is used for comparing the results between the capability curves obtained with the proposed MILP model and the results after deploying an exact AC power flow. The RMSE and average RMSE for the small WPP are shown in Table 5.9.

Table 5.9 – Accuracy assessment of the proposed MILP model for the small WPP.

Case		RMSE (Mvar)					Average	
		V = 0.95	V = 0.98	V = 1	V = 1.02	V = 1.05	Mvar	p.u.
Base	Inj.	0.046	0.031	0.027	0.019	0.017	0.028	2E-3
	Abs.	0.037	0.021	0.023	0.016	0.026	0.025	2E-3
I	Inj.	0.042	0.056	0.036	0.036	0.031	0.040	3E-3
	Abs.	0.101	0.071	0.060	0.032	0.051	0.063	5E-3
II	Inj.	0.052	0.049	0.021	0.022	0.022	0.032	3E-3
	Abs.	0.143	0.144	0.120	0.088	0.083	0.116	8E-3

The results in Table 5.9 show satisfactory accuracy of the proposed MILP model, with a maximum average RMSE of 0.8%.

5.3.3.2 Performance Validation

The RPC curves of the base case (orange), Case I (blue) and Case II (yellow) evaluated with different voltage levels γ^{PCC} at PCC are shown in Fig. 5.12.

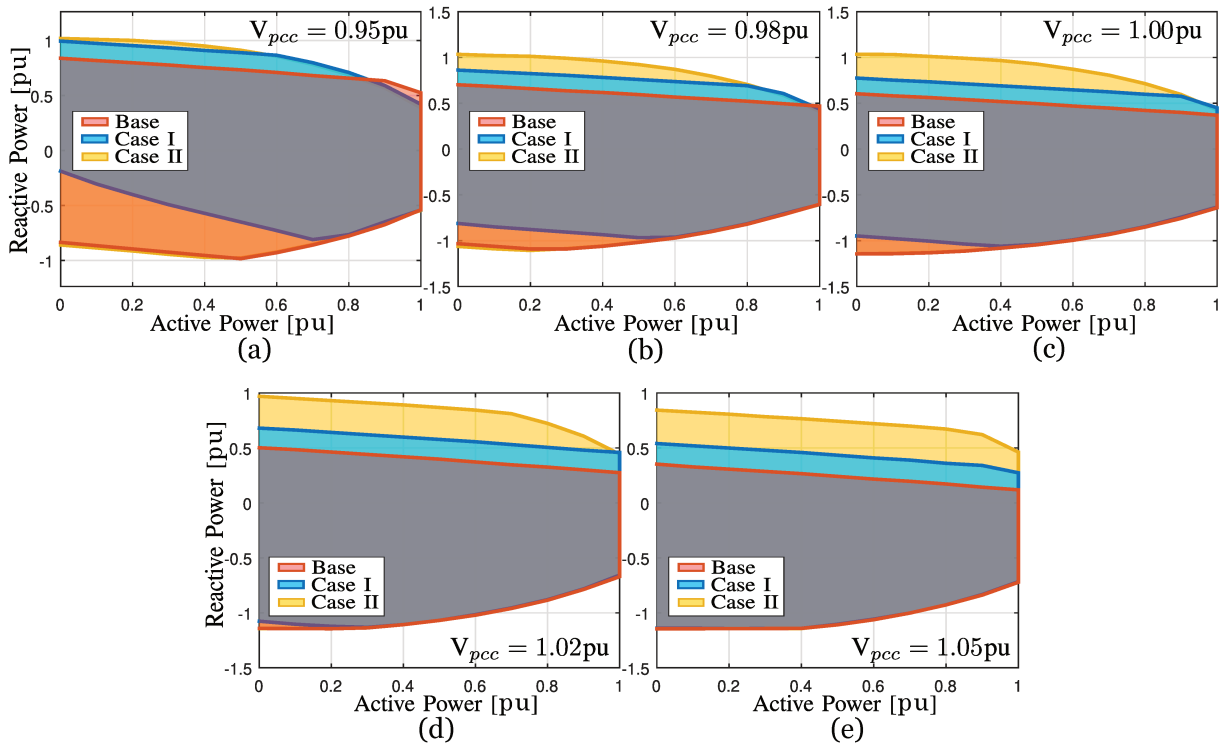


Figure 5.12 – Small WPP system reactive power capability obtained with the base case, Cases I and II.

From Fig. 5.12, the increase in reactive power capability in the injection mode can be observed in Cases I and II. However, in Case I, a decrease is observed in the absorption mode, notably when V_{pcc} is less than 1 p.u. The behavior of the latter is favorable, since, in a real operation, a greater injection of reactive power into the interconnected system is expected when V_{pcc} is less than 1 pu. This demonstrates a satisfactory performance, and an increase, in Cases I/II. This is contrasted with the PADC results in Table 5.10.

The PADC in (5.7) is used to compare the benefits of optimizing the tap-changer position of the transformers, instead of having them fixed in their nominal values (i.e., the base case). The PADC and average PADC for the small WPP are shown in Table 5.10.

Table 5.10 – Assessment of increased reactive power capability for the small WPP

Case		PADC (%)					Avg. (%)
		V = 0.95	V = 0.98	V = 1	V = 1.02	V = 1.05	
I	Inj.	15.0086	25.4944	34.3298	45.7636	79.6272	40.0447
	Abs.	-32.9205	-9.6652	-5.2932	-1.2460	-0.2642	-9.8778
II	Inj.	16.7365	45.4704	75.5939	109.2885	204.8410	90.3861
	Abs.	0.4390	0.3045	-0.4031	-0.2929	-0.1270	-0.0159

The results in Table 5.10 demonstrate that a significant increase in reactive power injection (capacitive behavior) is achieved, specially with Case II, having the largest increase with 90.386% of average PADC. Note that a decrease in reactive power absorption is attained in Case I, specially when the voltage magnitude at the PCC is below the nominal value. This is expected, because NLTC transformers in Case I cannot change their tap settings in real-time. Hence the proposed MILP model will give higher priority to the long-term voltage support when the voltage is below the nominal value, which is a case with the highest probability.

5.3.3.3 Obtained Tap Settings

The tap-changers obtained in Case studies I/II are shown in Tables 5.11–5.12.

Table 5.11 – Case I/II: Tap-changer positions of the NLTC transformers for the small WPP.

Case	TAP Position				
	[-2]	[-1]	[0]	[+1]	[+2]
Base	-	-	All	-	-
I	-	-	Main transformer	WT _(4–7)	WT _(1–3)
II	-	-	-	-	WT _(1–7)

*For the main transformer in *Case II*, see Table 5.12

Table 5.12 – Case II: Tap-changer positions of the main transformer equipped with OLTC for the small WPP.

γ^{wtg}	\leftarrow Q-Injection ($c = 1$) \rightarrow					\leftarrow Q-Absorption ($c = 2$) \rightarrow				
	0.95	0.98	1.0	1.02	1.05	0.95	0.98	1.0	1.02	1.05
0.0	+1	+2	+2	+2	+2	-2	-2	-2	-2	-2
0.1	+1	+2	+2	+2	+2	-2	-2	-2	-2	-2
0.2	+1	+2	+2	+2	+2	-2	-2	-2	-2	-2
0.3	+1	+2	+2	+2	+2	-2	-2	-2	-2	-2
0.4	+1	+2	+2	+2	+2	-2	-2	-2	-2	-2
0.5	+1	+2	+2	+2	+2	-2	-2	-2	-2	-2
0.6	+1	+2	+2	+2	+2	-2	-2	-2	-2	-2
0.7	+1	+2	+2	+2	+2	-2	-2	-2	-2	-2
0.8	+1	+2	+2	+2	+2	-2	-2	-2	-2	-2
0.9	+1	+2	+2	+2	+2	-2	-2	-2	-2	-1
1.0	+1	+2	+2	+2	+2	-2	-2	-2	-2	-1

Table 5.11 shows the tap-changer configuration chosen for transformers equipped with NLTC, observing that in this particular system with the considered scenarios, there is a combination of tap-changer where a greater reactive power capacity is obtained, as shown in Fig. 5.12. It is important to mention that the organization responsible for the coordination and operation control of the generation facilities is the one that requests the provide/absorb of reactive power to/from grid. In this way, the WPP operator can configure the tap-changer position according to Table 5.12.

5.3.4 Burbo bank WPP system

The Burbo Bank WPP system from (Sarkar et al., 2019) presents the topology shown in Fig. 5.13, comprising 25 WT feeders, each of 3.6 MW divided into three string.

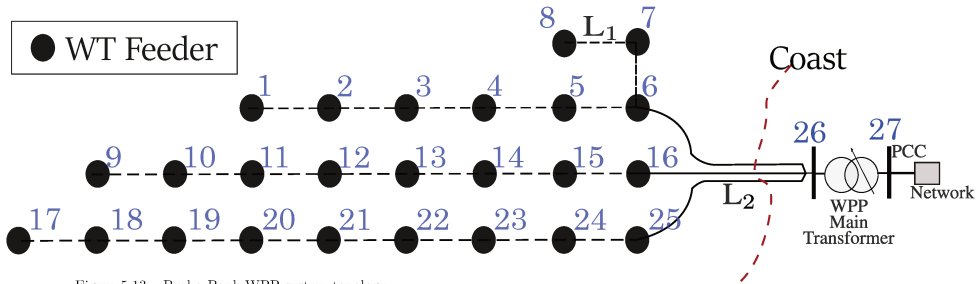


Figure 5.13 – Burbo Bank WPP system topology.

The reactive power capability curves obtained from base/I/ II case studies considering different voltage levels γ^{PCC} at the PCC for Burbo bank WPP system are presented in Fig. 5.14–5.16. Where the dotted red line represents the results determined with the MILP model and the black line represents the capability curve obtained after running the exact AC-PF.

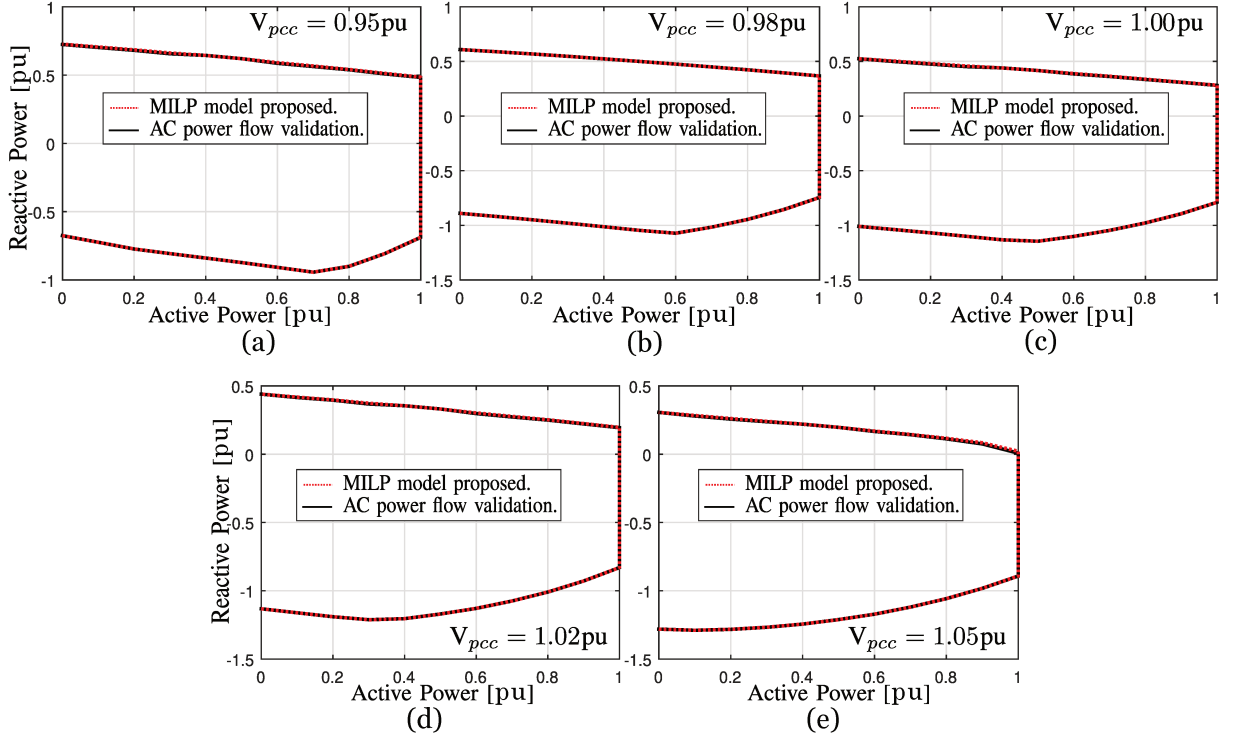


Figure 5.14 – Burbo bank WPP system reactive power capability using the MILP model and an exact AC-PF - Base case.

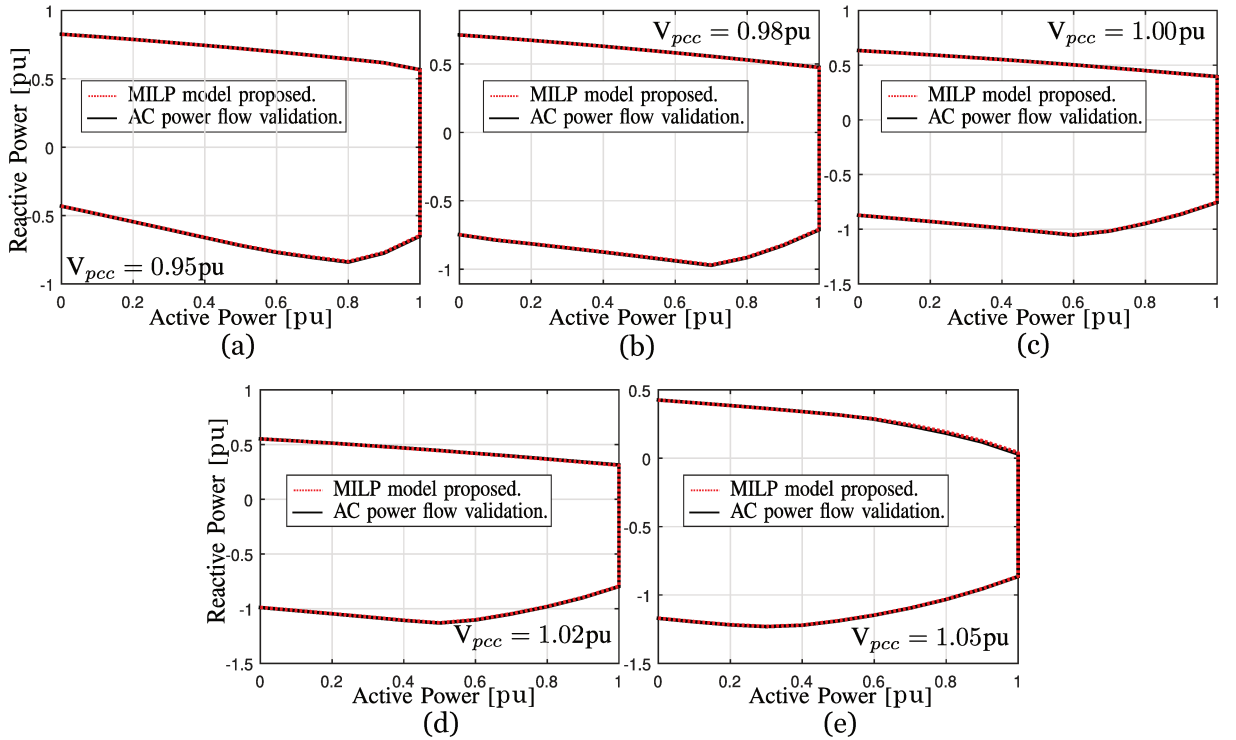


Figure 5.15 – Burbo bank WPP system reactive power capability using the MILP model and an exact AC-PF - Case I.

From Fig. 5.14–5.16, a great approximation of the proposed MILP model and the operating points obtained after running AC-PF can be observed. This demonstrates satisfactory accuracy of the MILP model and is contrasted with the RMSE results in Table 5.13.

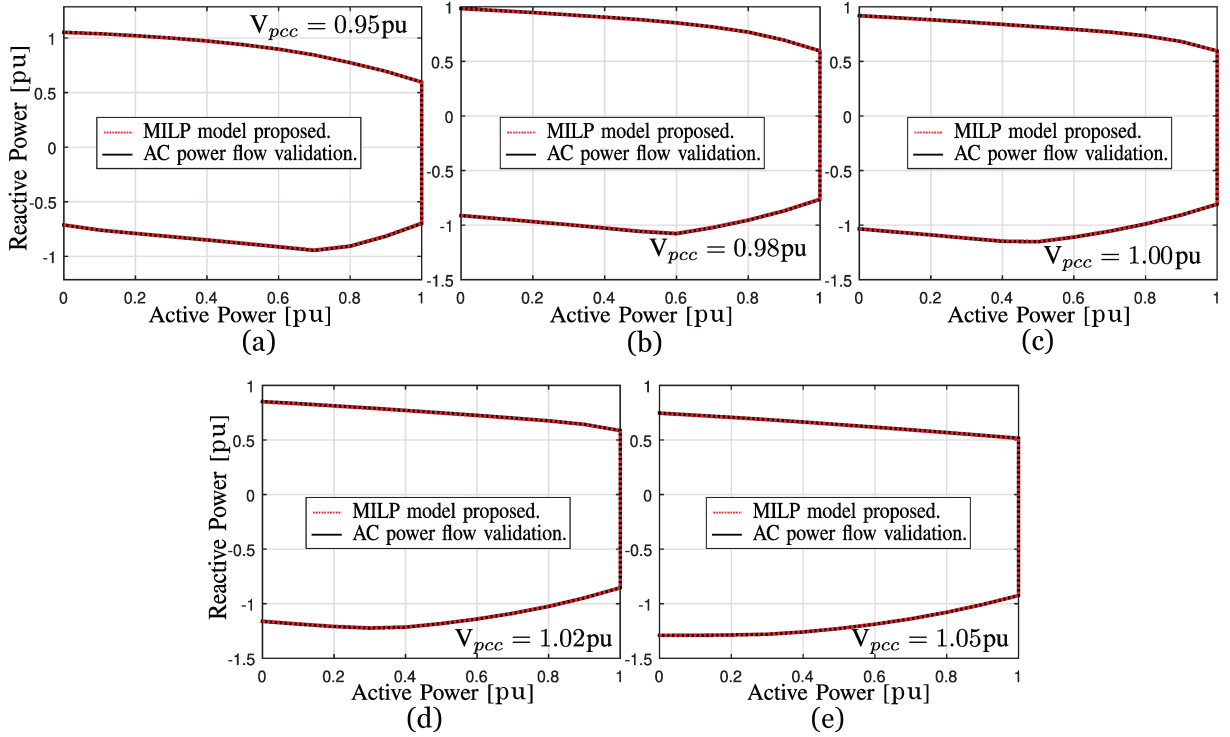


Figure 5.16 – Burbo bank WPP system reactive power capability using the MILP model and an exact AC-PF - Case II.

5.3.4.1 Accuracy Validation

In order to demonstrate the accuracy of the proposed MILP model (4.59), the RMSE in (5.6) is used for comparing the results between the capability curves obtained with the proposed MILP model and the results after deploying an exact AC power flow. The RMSE and average RMSE for the Burbo Bank WPP are shown in Table 5.13. The average RMSE represented in pu is calculated using the base power of 90 MVA.

Table 5.13 – Accuracy assessment of the proposed MILP model for Burbo Bank WPP.

Case		RMSE (Mvar)					Average	
		V = 0.95	V = 0.98	V = 1	V = 1.02	V = 1.05	Mvar	p.u.
Base	Inj.	0.042	0.039	0.042	0.041	0.052	0.043	5E-4
	Abs.	0.332	0.027	0.293	0.292	0.510	0.291	3E-3
I	Inj.	0.289	0.287	0.271	0.237	0.178	0.253	3E-3
	Abs.	0.090	0.110	0.149	0.169	0.551	0.248	2E-3
II	Inj.	0.242	0.233	0.229	0.170	0.095	0.193	2E-3
	Abs.	0.074	0.116	0.154	0.191	0.187	0.144	2E-3

The results in Table 5.13 show satisfactory accuracy of the proposed MILP model, with a maximum average RMSE of 0.2%.

5.3.4.2 Performance Validation

The RPC curves of the base case (orange), Case I (blue) and Case II (yellow) evaluated with different voltage levels γ^{PCC} at the PCC are shown in Fig. 5.17.

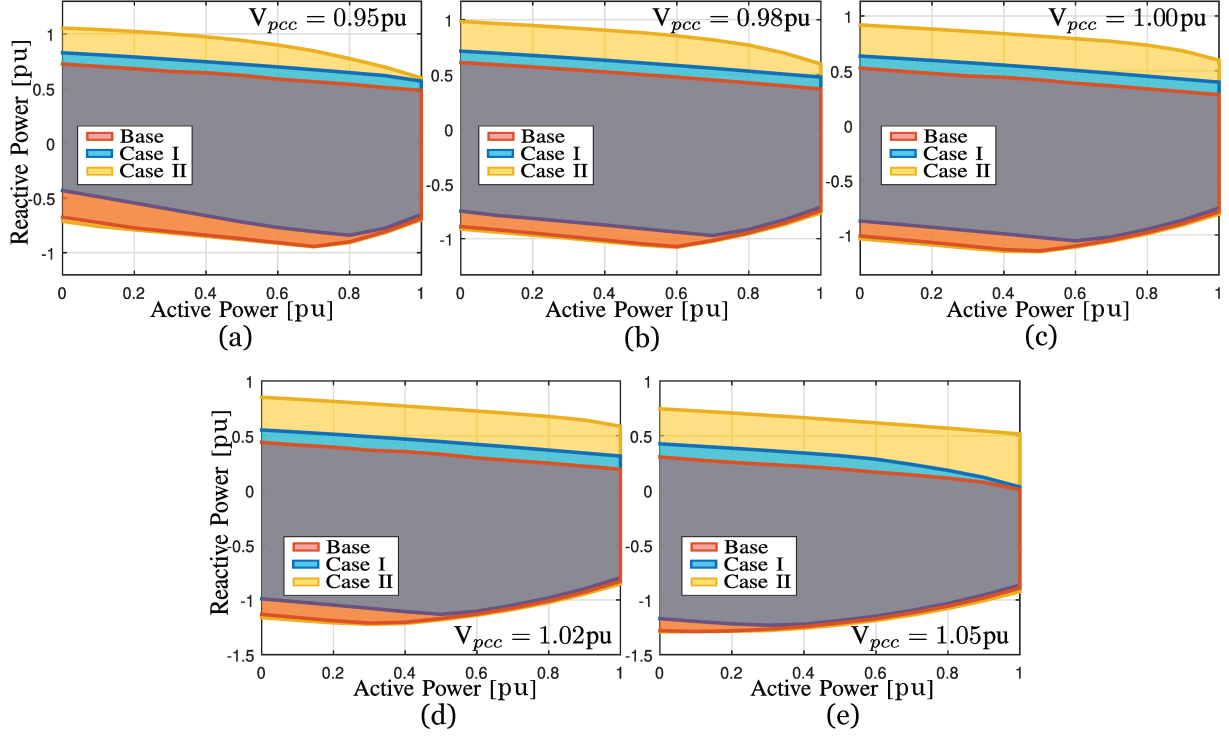


Figure 5.17 – Burbo bank WPP system reactive power capability obtained with the base case, Cases I and II.

From Fig. 5.17, the increase in reactive power capability in injection mode can be observed in Cases I and II. However, in Case I, a decrease is observed in absorption mode, notably when V_{pcc} is less than 1 p.u. This behavior of the latter is favorable, since, in a real operation, a greater injection of reactive power into the interconnected system is expected when V_{pcc} is less than 1 pu. This satisfactorily demonstrates a performance increase in Cases I/II, and is contrasted with the PADC results in Table 5.14.

The PADC in (5.7) is used to compare the benefits of optimizing the tap-changer position of the transformers, instead of having them fixed in their nominal values (i.e., the base case). The PADC and average PADC for the Burbo Bank WPP are shown in Table 5.14.

Table 5.14 – Assessment of increased reactive power capability for Burbo Bank WPP

Case		PADC (%)					Avg. (%)
		V = 0.95	V = 0.98	V = 1	V = 1.02	V = 1.05	
I	Inj.	17.2796	21.4365	28.2479	37.0206	55.7886	31.9546
	Abs.	-18.2258	-10.3850	-8.7165	-6.8089	-3.4461	-9.5164
II	Inj.	47.5578	72.3569	96.9520	130.4937	246.3442	118.7409
	Abs.	1.6505	1.5023	1.5091	1.4879	1.3012	1.4902

Results in Table 5.14, show a significant increase in reactive power injection (capacitive behavior) is achieved, specially with Case II having the largest increase with 118.741% of average PADG. Note that, a decrease in reactive power absorption is attained in Case I, specially when the voltage magnitude at the PCC is below the nominal value. This is expected, because NLTC transformers in Case I cannot change their tap settings in real time, hence, the proposed MILP model will give a higher priority to the long-term voltage support when the voltage is below the nominal value, which is a case with the highest probability.

5.3.4.3 Obtained Tap Settings

The tap-changers obtained in case studies I/II are shown in Tables 5.15–5.16.

Table 5.15 – Case I/II: Tap-changer positions of the NLTC transformers for Burbo Bank WPP system.

Case	TAP Position				
	[-2]	[-1]	[0]	[+1]	[+2]
Base	-	-	All	-	-
I	-	-	Main	WT _(1–25)	-
II	-	-	-	-	WT _(1–25)

*For the main transformer in *Case II*, see Table 5.16

Table 5.16 – Case II: Tap-changer positions of the main transformer equipped with OLTC for the Burbo Bank WPP system.

γ^{wtg}	← Q-Injection ($c = 1$) →					← Q-Absorption ($c = 2$) →				
	0.95	0.98	1.0	1.02	1.05	0.95	0.98	1.0	1.02	1.05
0.0	+2	+2	+2	+2	+2	-2	-2	-2	-2	-2
0.1	+2	+2	+2	+2	+2	-2	-2	-2	-2	-2
0.2	+2	+2	+2	+2	+2	-2	-2	-2	-2	-2
0.3	+2	+2	+2	+2	+2	-2	-2	-2	-2	-2
0.4	+2	+2	+2	+2	+2	-2	-2	-2	-2	-2
0.5	+2	+2	+2	+2	+2	-2	-2	-2	-2	-2
0.6	+2	+2	+2	+2	+2	-2	-2	-2	-2	-2
0.7	+2	+2	+2	+2	+2	-2	-2	-2	-2	-2
0.8	+2	+2	+2	+2	+2	-2	-2	-2	-2	-2
0.9	+2	+2	+2	+2	+2	-1	-2	-2	-2	-2
1.0	+2	+2	+2	+2	+2	0	-1	-2	-2	-2

Table 5.15 shows the tap-changer configuration chosen for transformers equipped with NLTC, observing that in this particular system with the considered scenarios, there is a combination of tap-changer where a greater reactive power capacity is obtained, as shown in Fig. 5.17. It is important to mention that the organization responsible for the coordination and control of the operations of the generation facilities is the one that requests the provide/absorb of reactive power to/from grid. In this way, the WPP operator can configure the tap-changer position according to Table 5.16.

5.3.5 Discussion

The ORPC problem for Type-4 based WPPs' planning stage is solved by the proposed MILP model (4.59), achieving the following benefits: (a) Obtain a tap-setting of the WT and main transformers for the operation of a WPP, according to the type of case study; (b) Convergence to optimality is guaranteed by MILP commercial solvers; and (c) A scalable, flexible and accurate MILP model. It was verified that the proposed model is efficient, obtaining an increase of the reactive power capability up to 118.75% (average PADC) for the tests in two WPP systems and with a low error in the linear approximation of less than 1.0% (average RMSE).

6 Conclusions and Future Works

6.1 Conclusions

This dissertation presented a novel methodology to enlarge the reactive power capability in a Type-4 based WPP, highlighting its usefulness in the planning stage, since this methodology allows to obtain an optimal WPP tap setting of the transformers, thus allowing to increase the RPC. Additionally, this methodology allows to generate the RPC curves in real-time operations. This methodology is based on a MILP model, which is easy to implement and adequately solved by commercial solvers. The conclusions of this dissertation are presented below:

- A linear model of the reactive power capacity of Type-4 WT was obtained using the Taylor decomposition. This solution strategy was presented in section 4.3.1, obtaining adequate results with an average RMSE of 0.0022 pu^2 (see Appendix D).
- A new formulation to solve the RPC/ORPC in a Type-4 based WPP was presented. It considered discrete controllers, scenarios, probability of each scenario, operation mode, electrical and operation limits, all in a unique integrated MILP model. This proposed MILP model can be solved using existing off-the-shelf convex optimization solvers, achieving the following benefits: (a) Obtain a tap-setting of the WT and main transformers for the operation of a WPP, according to the type of case study; (b) Convergence to optimality is guaranteed by MILP commercial solvers; and (c) A scalable, flexible and accurate MILP model with a low computational burden. It was verified that the proposed model is efficient, increasing the reactive power capability for the tests in two WPP systems and with a low error margin in the linear approximation, guaranteeing an optimal solution in a reasonable time, either for real-time operation or planning stage.
- The results obtained for the estimated RPC in a Type-4 based WPP, for real-time operation using the proposed methodology, present a suitable approximation to the base method without considering the collector system's limits. However, if these limits are considered, the estimated RPC will be affected. This is corroborated with the results in sections 5.2.1.2 and 5.2.2.2, thus demonstrating the importance of including them. These results contribute to an advance in the research for the adequate dimension of the components according to the RPC required of a WPP.
- The optimal tap-changer setting obtained from case studies I/II using the proposed methodology for the planning stage achieves an enlarged RPC, this is corroborated

with the results in sections 5.3.3.2 and 5.3.4.2. These results contribute to improve the reliability and ensure the active power production of the WPP due to voltage fluctuations in the transmission network.

6.2 Future Works

1. Adequate sizing of electrical components in a WPP, according to the amount of reactive power required using the proposed ORPC model.
2. Automatic control strategies for tap-changer transformers equipped with OLTC, in order to obtain an enlargement of the RPC using the results of case study II.
3. The proposed ORPC model can be extended to:
 - Any WT type based WPP.
 - Considering different levels of active power production for each individual WT.

Bibliography

- BYRD, R. H.; NOCEDAL, J.; WALTZ, R. A. *KNITRO: An integrad package for nonlinear optimization*. 1st. ed. [S.l.]: Springer, 2006. Cited 2 times on pages 30 and 54.
- Camm, E. H. et al. Reactive power compensation for wind power plants. *2009 IEEE Power Energy Society General Meeting*, v. 29, n. 3, p. 1–7, Jul. 2009. Cited on page 19.
- Das, K.; HANSEN, A. D.; Sørensen, P. Understanding IEC standard wind turbine models using SimPowerSystems. *Wind Engineering*, v. 40, p. 212–227, April 2016. Cited on page 37.
- de Almeida, R. G.; Castronuovo, E. D.; Lopes, J. A. P. Optimum generation control in wind parks when carrying out system operator requests. *IEEE Trans. Power Syst.*, v. 21, n. 2, p. 718–725, May 2006. Cited on page 19.
- DELGADO, M. A. D. J. *Otimização De Sistemas De Distribuição De Energia Elétrica Radiais Usando Programação Cônica De Segunda Ordem Inteira Mista*. Dissertação (Mestrado) — Universidade Estadual Paulista Júlio de Mesquita Filho, Faculdade de Engenharia de Ilha Solteira, Brasil, 2015. Cited 3 times on pages 28, 33, and 34.
- DUNNING, I.; HUCHETTE, J.; LUBIN, M. *JuMP: A modeling language for mathematical optimization*. [S.l.: s.n.], 2015. Cited on page 74.
- Ellis, A.; Muljadi, E. Wind power plant representation in large-scale power flow simulations in wecc. *2008 IEEE Power and Energy Society General Meeting - Conversion and Delivery of Electrical Energy in the 21st Century*, p. 1–6, Jul. 2008. Cited 2 times on pages 10 and 20.
- GLOVER, J.; SARMA, M.; OVERBYE, T. *Power System Analysis & Design, SI version*. 5th. ed. [S.l.]: Cengage Learning, 2012. Cited on page 37.
- GONÇALVES, R. d. R. *Modelos de programação linear inteira mista para resolver problemas de otimização de sistemas de distribuição de energia elétrica radiais*. Tese (Doutorado) — Universidade Estadual Paulista Júlio de Mesquita Filho, Faculdade de Engenharia de Ilha Solteira, Brasil, 2013. Cited 2 times on pages 26 and 28.
- IBM ILOG. *User's Manual for CPLEX v12.1*. [S.l.], 2009. Cited 5 times on pages 32, 33, 59, 64, and 74.
- IRENA. *Wind Energy*. 2019. [Online; accessed 30-March-2020]. Disponível em: <<https://www.irena.org/wind>>. Cited on page 18.
- Kanna, B.; Singh, S. N. Towards reactive power dispatch within a wind farm using hybrid PSO. *International Journal of Electrical Power & Energy Systems*, v. 69, p. 232–240, Jul. 2015. Cited on page 19.
- Karbouj, H.; Rather, Z. H. Voltage control ancillary service from wind power plant. *IEEE Trans. Sustainable Energy*, v. 10, n. 2, p. 759–767, Apr. 2018. Cited 3 times on pages 19, 37, and 45.

- Kim, J. et al. Adaptive hierarchical voltage control of a DFIG-based wind power plant for a grid fault. *IEEE Trans. Smart Grid*, v. 7, n. 6, p. 2980–2990, Nov. 2016. Cited 3 times on pages 19, 37, and 45.
- Konopinski, R. J.; Vijayan, P.; Ajjarapu, V. Extended reactive capability of DFIG wind parks for enhanced system performance. *IEEE Trans. Power Syst.*, v. 24, n. 3, p. 1346–1355, Aug. 2009. Cited 3 times on pages 19, 37, and 41.
- Kundur, P. et al. Definition and classification of power system stability iee/cigre joint task force on stability terms and definitions. *IEEE Trans. Power Syst.*, v. 19, n. 3, p. 1387–1401, Aug. 2004. Cited on page 20.
- KWON, C. *Julia Programming for Operations Research: A Primer on Computing*. 3rd. ed. [S.l.: s.n.], 2016. Cited 7 times on pages 30, 32, 33, 54, 59, 64, and 74.
- Lin, M. H. et al. A review of piecewise linearization methods. *Mathematical Problems in Engineering*, p. 1–7, Jun. 2013. Cited 2 times on pages 31 and 58.
- Low, M.; Farivar. Branch flow model: relaxations and convexification - Part I. *IEEE Trans. Power Syst.*, v. 28, n. 3, p. 2554–2564, Aug. 2013. Cited 2 times on pages 52 and 53.
- Macedo, L. H. et al. Optimal operation of distribution networks considering energy storage devices. *IEEE Trans. Smart Grid*, v. 6, n. 6, p. 2825–2836, Nov. 2015. Cited on page 56.
- Martin, B. et al. Loss reduction in a windfarm participating in primary voltage control using an extension of the convex distflow OPF. *2018 Power Systems Computation Conference (PSCC)*, p. 1–8, Jun. 2018. Cited 3 times on pages 10, 19, and 26.
- Martinez, M. et al. Reactive power dispatch in wind farms using particle swarm optimization technique and feasible solutions search. *Applied Energy*, v. 88, n. 12, p. 4678–4686, Dec. 2011. Cited on page 19.
- Martínez, J. et al. Var reserve concept applied to a wind power plant. In: *2011 IEEE/PES Power Systems Conference and Exposition*. Phoenix, AZ, USA: [s.n.], 2011. Cited on page 19.
- Meegahapola, L.; Littler, T.; Pereraa, S. Capability curve based enhanced reactive power control strategy for stability enhancement and network voltage management. *International Journal of Electrical Power & Energy Systems*, v. 52, p. 96–106, Nov. 2013. Cited 3 times on pages 19, 37, and 41.
- Mhanna, S.; Verbič, G.; Chapman, A. C. Tight LP approximations for the optimal power flow problem. *2016 Power Systems Computation Conference (PSCC)*, p. 1–7, Jun. 2016. Cited on page 61.
- MICHAEL, G. *Advanced Engineering Mathematics*. 3nd. ed. [S.l.]: Prentice Hall, 1998. Cited on page 107.
- Muljadi, E. et al. Equivalencing the collector system of a large wind power plant. p. 9 pp.–, June 2006. Cited 6 times on pages 11, 42, 99, 101, 102, and 104.
- NERC. Bps-connected inverter-based resource performance. p. 45, Sep. 2018. Cited on page 18.

R. Fourer and D. M. Gay and B. W. Kernighan. *AMPL: A modeling language for mathematical programming*. [S.l.], 2003. Cited 4 times on pages 30, 32, 54, and 59.

Sarkar, M. et al. Reactive power capability model of wind power plant using aggregated wind power collection system. *Energies*, v. 12, n. 9, Apr. 2019. Cited 14 times on pages 10, 19, 37, 38, 40, 41, 42, 45, 46, 63, 64, 68, 74, and 80.

SEIFI, H.; SEPASIAN, M. S. Power system planning, basic principles. In: _____. *Electric Power System Planning: Issues, Algorithms and Solutions*. Berlin, Heidelberg: Springer Berlin Heidelberg, 2011. p. 1–14. ISBN 978-3-642-17989-1. Disponible em: <https://doi.org/10.1007/978-3-642-17989-1_1>. Cited on page 74.

Tapia, A.; Tapia, G.; Ostolaza, J. X. Reactive power control of wind farms for voltage control applications. *Renewable Energy*, v. 29, n. 3, p. 377–392, Mar. 2004. Cited on page 19.

Ullah, N. R.; Bhattacharya, K.; Thiringer, T. Wind farms as reactive power ancillary service providers—technical and economic issues. *IEEE Trans. Energy Conv.*, v. 24, n. 3, p. 661–672, Sep. 2009. Cited 3 times on pages 19, 37, and 45.

Yoshiaki Kawajir. *Introduction to IPOPT*. [S.l.], 2015. Cited 5 times on pages 30, 32, 33, 64, and 74.

Zhang, B. et al. A reactive power dispatch strategy with loss minimization for a DFIG-based wind farm. *IEEE Transactions on Sustainable Energy*, v. 7, n. 3, p. 914–923, Jul. 2016. Cited on page 19.

ZHANG, B. et al. Review of reactive power dispatch strategies for loss minimization in a DFIG-based wind farm. *Energies*, v. 10, n. 856, 2017. Cited on page 19.

Appendices

A Electrical Data From Radial Distribution Systems

A.1 136-Bus Radial Distribution System

Table A.1 – Bus Data 136-Bus Radial Distribution System

Bus	β_i^T	$P_i^d[\text{kW}]$	$Q_i^d[\text{kVar}]$	$B_i^{sh}[\Omega]$	Bus	β_i^T	$P_i^d[\text{kW}]$	$Q_i^d[\text{kVar}]$	$B_i^{sh}[\Omega]$
1	3	0	0	0	69	0	176.41	70.184	0
2	0	0	0	0	70	0	83.015	33.028	0
3	0	47.78	19.009	0	71	0	217.92	86.698	0
4	0	42.551	16.929	0	72	0	23.294	9.267	0
5	0	87.022	34.622	0	73	0	5.075	2.019	0
6	0	311.31	123.86	0	74	0	72.638	28.899	0
7	0	148.87	59.228	0	75	0	405.99	161.52	0
8	0	238.67	94.956	0	76	0	0	0	0
9	0	62.299	24.786	0	77	0	100.18	42.468	0
10	0	124.59	49.571	0	78	0	142.52	60.417	0
11	0	140.16	55.768	0	79	0	96.042	40.713	0
12	0	116.81	46.474	0	80	0	300.45	127.37	0
13	0	249.2	99.145	0	81	0	141.24	59.873	0
14	0	291.45	115.59	0	82	0	279.85	118.63	0
15	0	303.72	120.84	0	83	0	87.312	37.013	0
16	0	215.39	85.695	0	84	0	243.85	103.37	0
17	0	198.59	79.007	0	85	0	247.75	105.03	0
18	0	0	0	0	86	0	0	0	0
19	0	0	0	0	87	0	89.878	38.101	0
20	0	0	0	0	88	2	1137.3	482.11	0
21	0	30.127	14.729	0	89	0	458.34	194.3	0
22	0	230.97	112.92	0	90	0	385.2	163.29	0
23	0	60.256	29.459	0	91	0	0	0	0
24	0	230.97	112.92	0	92	0	79.608	33.747	0
25	0	120.51	58.915	0	93	0	87.312	37.013	0
26	0	0	0	0	94	0	0	0	0
27	0	56.981	27.857	0	95	0	74.001	31.37	0
28	0	364.67	178.28	0	96	0	232.05	98.369	0

Table A.1 continued from previous page

Bus	\mathcal{B}_i^T	$P_i^d[\text{kW}]$	$Q_i^d[\text{kVar}]$	$B_i^{sh}[\Omega]$	Bus	\mathcal{B}_i^T	$P_i^d[\text{kW}]$	$Q_i^d[\text{kVar}]$	$B_i^{sh}[\Omega]$
29	0	0	0	0	97	0	141.82	60.119	0
30	0	124.65	60.939	0	98	0	0	0	0
31	0	56.981	27.857	0	99	0	76.449	32.408	0
32	0	0	0	0	100	0	0	0	0
33	0	85.473	41.787	0	101	0	51.322	21.756	0
34	0	0	0	0	102	0	59.874	25.381	0
35	0	396.74	193.96	0	103	0	9.065	3.843	0
36	0	0	0	0	104	0	2.092	0.887	0
37	0	181.15	88.563	0	105	0	16.735	7.094	0
38	0	242.17	118.39	0	106	2	1506.5	638.63	0
39	0	75.316	36.821	0	107	0	313.02	132.69	0
40	0	0	0	0	108	0	79.831	33.842	0
41	0	1.254	0.531	0	109	0	51.322	21.756	0
42	0	6.274	2.66	0	110	0	0	0	0
43	0	0	0	0	111	0	202.44	85.815	0
44	0	117.88	49.971	0	112	0	60.823	25.874	0
45	0	62.668	25.566	0	113	0	45.618	19.338	0
46	0	172.29	73.034	0	114	0	0	0	0
47	0	458.56	194.39	0	115	0	157.07	66.584	0
48	0	262.96	111.47	0	116	0	0	0	0
49	0	235.76	99.942	0	117	0	250.15	106.04	0
50	0	0	0	0	118	0	0	0	0
51	0	109.22	46.298	0	119	0	68.809	28.593	0
52	0	0	0	0	120	0	32.072	13.596	0
53	0	72.809	30.865	0	121	0	61.084	25.894	0
54	0	258.47	109.57	0	122	0	0	0	0
55	0	69.169	29.322	0	123	0	94.622	46.26	0
56	0	21.843	9.26	0	124	0	49.858	24.375	0
57	0	0	0	0	125	0	123.16	60.214	0
58	0	20.527	8.702	0	126	0	78.35	38.304	0
59	0	150.55	63.819	0	127	0	145.48	71.121	0
60	0	220.69	93.552	0	128	0	21.369	10.447	0
61	0	92.384	39.163	0	129	0	74.789	36.564	0
62	0	0	0	0	130	0	227.93	111.43	0
63	0	226.69	96.098	0	131	0	35.614	17.411	0
64	0	0	0	0	132	0	249.29	121.88	0
65	0	294.02	116.97	0	133	0	316.72	154.84	0

Table A.1 continued from previous page

Bus	\mathcal{B}_i^T	$P_i^d[\text{kW}]$	$Q_i^d[\text{kVar}]$	$B_i^{sh}[\Omega]$	Bus	\mathcal{B}_i^T	$P_i^d[\text{kW}]$	$Q_i^d[\text{kVar}]$	$B_i^{sh}[\Omega]$
66	0	83.015	33.028	0	134	0	333.82	163.2	0
67	0	83.015	33.028	0	135	0	249.29	121.88	0
68	0	103.77	41.285	0	136	0	0	0	0

Table A.2 – Generation Data 136-Bus Radial Distribution System

Bus	$\overline{P}_i^g [\text{kW}]$	$\underline{Q}_i^g [\text{kVar}]$	$\overline{Q}_i^g [\text{kVar}]$
1	99999	-99999	99999
88	500	-250	250
106	500	-250	250

Table A.3 – Branch Data 136-Bus Radial Distribution System

Item	Branch $[i-j]$	$R_{ij} [\Omega]$	$X_{ij} [\Omega]$	$B_{ij}^{shl} [\Omega]$	a_{ij}	$\bar{I}_{ij} [\text{A}]$
1	1-2	3.32E-01	7.67E-01	0	0	381
2	2-3	1.88E-03	4.33E-03	0	0	369
3	3-4	2.23E-01	5.15E-01	0	0	363
4	4-5	9.94E-02	2.30E-01	0	0	350
5	5-6	1.56E-01	3.59E-01	0	0	335
6	6-7	1.63E-01	3.77E-01	0	0	288
7	7-8	1.14E-01	2.64E-01	0	0	32
8	7-9	5.68E-02	5.67E-02	0	0	232
9	9-10	5.21E-01	2.74E-01	0	0	17
10	9-11	0.10877	0.1086	0	0	206
11	11-12	0.39803	0.20937	0	0	16
12	11-13	0.91744	0.31469	0	0	34
13	11-14	0.11823	0.11805	0	0	137
14	14-15	0.50228	0.26421	0	0	41
15	14-16	0.05675	0.05666	0	0	56
16	16-17	0.29379	0.15454	0	0	27
17	1-18	0.33205	0.76653	0	0	342
18	18-19	0.00188	0.00433	0	0	333
19	19-20	0.22324	0.51535	0	0	332
20	20-21	0.10881	0.25118	0	0	326
21	21-22	0.71078	0.37388	0	0	32

Table A.3 continued from previous page

Item	Branch $[i-j]$	R_{ij} [Ω]	X_{ij} [Ω]	B_{ij}^{shl} [Ω]	a_{ij}	\bar{I}_{ij} [A]
22	21-23	0.18197	0.42008	0	0	286
23	23-24	0.30326	0.15952	0	0	32
24	23-25	0.02439	0.0563	0	0	242
25	25-26	0.04502	0.10394	0	0	224
26	26-27	0.01876	0.04331	0	0	224
27	27-28	0.11823	0.1123	0	0	216
28	28-29	0.02365	0.02361	0	0	163
29	29-30	0.18954	0.0997	0	0	25
30	30-31	0.39803	0.20937	0	0	8
31	29-32	0.05675	0.05666	0	0	138
32	32-33	0.09477	0.04985	0	0	68
33	33-34	0.41699	0.21934	0	0	56
34	34-35	0.11372	0.05982	0	0	55
35	32-36	0.07566	0.07555	0	0	70
36	36-37	0.3696	0.19442	0	0	59
37	37-38	0.26536	0.13958	0	0	34
38	36-39	0.05675	0.0566	0	0	11
39	1-40	0.33205	0.76653	0	0	374
40	40-41	0.11819	0.27283	0	0	363
41	41-42	2.96288	1.01628	0	0	1
42	41-43	0.00188	0.00433	0	0	358
43	43-44	0.06941	0.16024	0	0	358
44	44-45	0.81502	0.42872	0	0	9
45	44-46	0.06378	0.14724	0	0	331
46	46-47	0.13132	0.30315	0	0	306
47	47-48	0.06191	0.14291	0	0	240
48	48-49	0.11444	0.26417	0	0	173
49	49-50	0.28374	0.28331	0	0	15
50	50-51	0.28374	0.28321	0	0	15
51	49-52	0.04502	0.10394	0	0	125
52	52-53	0.02626	0.06063	0	0	125
53	53-54	0.06003	0.13858	0	0	48
54	54-55	0.03002	0.06929	0	0	12
55	55-56	0.02064	0.04764	0	0	3
56	53-57	0.10881	0.25118	0	0	67
57	57-58	0.25588	0.1346	0	0	67
58	58-59	0.41699	0.21934	0	0	64

Table A.3 continued from previous page

Item	Branch $[i-j]$	R_{ij} $[\Omega]$	X_{ij} $[\Omega]$	B_{ij}^{shl} $[\Omega]$	a_{ij}	\bar{I}_{ij} $[A]$
59	59-60	0.50228	0.26421	0	0	43
60	60-61	0.3317	0.17448	0	0	13
61	61-62	0.20849	0.10967	0	0	1
62	48-63	0.13882	0.32047	0	0	31
63	1-64	0.0075	0.01732	0	0	221
64	64-65	0.27014	0.62362	0	0	221
65	65-66	0.3827	0.88346	0	0	178
66	66-67	0.33018	0.7622	0	0	164
67	67-68	0.3283	0.75787	0	0	150
68	68-69	0.17072	0.39409	0	0	135
69	69-70	0.55914	0.29412	0	0	11
70	69-71	0.05816	0.13425	0	0	99
71	71-72	0.7013	0.3689	0	0	4
72	72-73	1.02352	0.53839	0	0	1
73	71-74	0.06754	0.15591	0	0	65
74	74-75	1.32352	0.45397	0	0	55
75	1-76	0.01126	0.02598	0	0	242
76	76-77	0.72976	1.68464	0	0	242
77	77-78	0.22512	0.51968	0	0	219
78	78-79	0.20824	0.48071	0	0	196
79	79-80	0.0469	0.10827	0	0	181
80	80-81	0.6195	0.61857	0	0	140
81	81-82	0.34049	0.33998	0	0	118
82	82-83	0.56862	0.29911	0	0	12
83	82-84	0.10877	0.1086	0	0	67
84	84-85	0.56862	0.29911	0	0	34
85	1-86	0.01126	0.02598	0	0	400
86	86-87	0.41835	0.96575	0	0	400
87	87-88	0.10499	0.13641	0	0	156
88	87-89	0.43898	1.01338	0	0	216
89	89-90	0.0752	0.02579	0	0	149
90	90-91	0.07692	0.17756	0	0	96
91	91-92	0.33205	0.76653	0	0	96
92	92-93	0.08442	0.19488	0	0	84
93	93-94	0.1332	0.30748	0	0	72
94	94-95	0.2932	0.29276	0	0	61
95	95-96	0.21753	0.21721	0	0	51

Table A.3 continued from previous page

Item	Branch [$i-j$]	R_{ij} [Ω]	X_{ij} [Ω]	B_{ij}^{shl} [Ω]	a_{ij}	\bar{I}_{ij} [A]
96	96-97	0.26482	0.26443	0	0	19
97	94-98	0.10318	0.23819	0	0	10
98	98-99	0.13507	0.31181	0	0	10
99	1-100	0.00938	0.02165	0	0	535
100	100-101	0.16884	0.38976	0	0	534
101	101-102	0.11819	0.27283	0	0	514
102	102-103	2.28608	0.78414	0	0	1
103	102-104	0.45587	1.05236	0	0	496
104	104-105	0.696	1.60669	0	0	464
105	105-106	0.45774	1.05669	0	0	393
106	106-107	0.20298	0.26373	0	0	162
107	107-108	0.21348	0.27737	0	0	118
108	108-109	0.54967	0.28914	0	0	64
109	109-110	0.54019	0.28415	0	0	35
110	108-111	0.0455	0.05911	0	0	42
111	111-112	0.47385	0.24926	0	0	15
112	112-113	0.86241	0.45364	0	0	6
113	113-114	0.56862	0.29911	0	0	1
114	109-115	0.77711	0.40878	0	0	21
115	115-116	1.08038	0.5683	0	0	1
116	110-117	1.06633	0.57827	0	0	34
117	117-118	0.47385	0.24926	0	0	1
118	105-119	0.32267	0.74488	0	0	22
119	119-120	0.14633	0.33779	0	0	13
120	120-121	0.12382	0.28583	0	0	8
121	1-122	0.01126	0.02598	0	0	301
122	122-123	0.6491	1.49842	0	0	300
123	123-124	0.04502	0.10394	0	0	273
124	124-125	0.5264	0.18056	0	0	17
125	124-126	0.02064	0.04764	0	0	248
126	126-127	0.53071	0.27917	0	0	20
127	126-128	0.09755	0.2252	0	0	216
128	128-129	0.11819	0.27283	0	0	10
129	128-130	0.13882	0.32047	0	0	201
130	130-131	0.04315	0.09961	0	0	168
131	131-132	0.09192	0.2122	0	0	163
132	132-133	0.16134	0.37244	0	0	127

Table A.3 continued from previous page

Item	Branch $[i-j]$	R_{ij} $[\Omega]$	X_{ij} $[\Omega]$	B_{ij}^{shl} $[\Omega]$	a_{ij}	\bar{I}_{ij} [A]
133	133-134	0.37832	0.37775	0	0	82
134	134-135	0.39724	0.39664	0	0	35
135	135-136	0.2932	0.29276	0	0	1

B Equivalent Collector System for a WPP

This appendix describes the steps used to determine the equivalent of the collecting system of a wind power plant (WPP) proposed by (Muljadi et al., 2006), as shown in Fig. B.1. This method is based on power losses of the collecting grid, considering the following assumptions: The current output from all wind turbines (WTs) is assumed to be identical (magnitude and angle); and reactive power generated by the line capacitive shunts is based on the assumption that the voltage at the buses is one per unit.

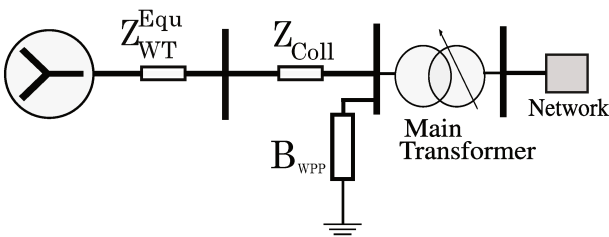


Fig. B.1 – Equivalent diagram of the collector system of a typical WPP. [Source: adapted from (Muljadi et al., 2006)]

First Step: *Connection at the trunk*

The procedure to determine the equivalent impedance of the collecting system for a ring or daisy-chain configuration, as shown in Fig. B.2, is as follows. The transformer is considered to be part of the generator its equivalent circuit. The collector system is determined excluding the WTs.



$$\begin{aligned}\vec{I}_s &= \vec{I}_1 + \vec{I}_2 + \vec{I}_3 + \vec{I}_4 \\ \text{supposing that: } \vec{I}_1 &= \vec{I}_2 = \vec{I}_3 = \vec{I}_4 = \vec{I} \\ \text{obtaining: } \vec{I}_s &= 4 \times \vec{I}\end{aligned}$$

Therefore, the total current in the equivalent representation is given by $\vec{I}_s = n \times \vec{I}$, where n is the number of WTs connected to their respective string.

The voltage drop across each impedance, can be expressed by the following equations::

$$\begin{aligned}\Delta \vec{V}_{Z_1} &= \vec{I}_1 Z_1 = \vec{I} Z_1 \\ \Delta \vec{V}_{Z_2} &= (\vec{I}_1 + \vec{I}_2) Z_2 = 2 \vec{I} Z_2 \\ \Delta \vec{V}_{Z_3} &= (\vec{I}_1 + \vec{I}_2 + \vec{I}_3) Z_3 = 3 \vec{I} Z_3 \\ \Delta \vec{V}_{Z_4} &= (\vec{I}_1 + \vec{I}_2 + \vec{I}_3 + \vec{I}_4) Z_4 = 4 \vec{I} Z_4\end{aligned}$$

The power loss at each impedance, can be computed as:

$$\begin{aligned}S_{Z_1}^{\text{Loss}} &= \Delta \vec{V}_{Z_1} \vec{I}_1^* = \vec{I} \vec{I}^* Z_1 = I^2 Z_1 \\ S_{Z_2}^{\text{Loss}} &= \Delta \vec{V}_{Z_2} (\vec{I}_1 + \vec{I}_2)^* = 2 \vec{I} Z_2 (2 \vec{I})^* = 4 I^2 Z_2 \\ S_{Z_3}^{\text{Loss}} &= \Delta \vec{V}_{Z_3} (\vec{I}_1 + \vec{I}_2 + \vec{I}_3)^* = 3 \vec{I} Z_3 (3 \vec{I})^* = 9 I^2 Z_3 \\ S_{Z_4}^{\text{Loss}} &= \Delta \vec{V}_{Z_4} (\vec{I}_1 + \vec{I}_2 + \vec{I}_3 + \vec{I}_4)^* = 4 \vec{I} Z_4 (4 \vec{I})^* = 16 I^2 Z_4\end{aligned}$$

Using the simplification of $\Delta \vec{V}_{Z_m}$ and \vec{I} , the power loss equation can be simplified as follows:

$$\begin{aligned}S_{\text{Serie}}^{\text{Loss}} &= I^2 (Z_1 + 2^2 Z_2 + 3^2 Z_3 + 4^2 Z_4) \\ S_{\text{Serie}}^{\text{Loss}} &= I^2 \sum_{m=1}^n m^2 Z_m\end{aligned}\tag{B.1}$$

Where, I represents the output magnitude current of WTs, n is the number of WTs in the string, Z_m represents the individual series impedances. On the other hand, the total loss equation can also be written as follows:

$$S_{\text{Serie}}^{\text{Loss}} = I_s^2 Z_s\tag{B.2}$$

Therefore from Equation (B.1) and (B.2), it is possible to determine the equivalent impedance like this:

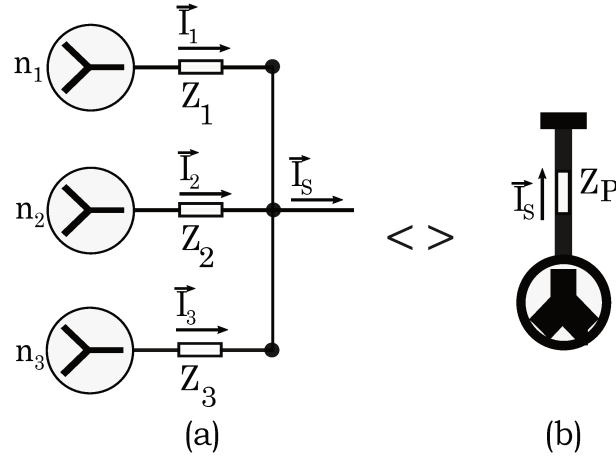
$$Z_s = \frac{\sum_{m=1}^n m^2 Z_m}{n^2}\tag{B.3}$$

B.2 Second Step *Connection at the feeder level*

Procedure to determine the equivalent impedance of parallel branches (multiple WTs groups) connected to the same node, as shown in Fig. B.3(a). Each branch has a

unique impedance and is connected to equivalent circuit of a group of WTs seen in previous section. Let us consider a simple three-branch configuration connected to the same node. For this configuration, is made the following assumptions:

- Equivalent circuits for three circuits have been found following the methodology described in the previous section.
- Each parallel circuit consists of n_1 , n_2 and n_3 WTs respectively.
- All WTs produce identical output current (magnitude and angle).
- The impedance from each group to the point of interconnection is Z_1 , Z_2 , Z_3 respectively.



expression is obtained:

$$S_P^{\text{Loss}} = I_P^2 Z_P = n_1^2 I^2 Z_1 + n_2^2 I^2 Z_2 + n_3^2 I^2 Z_3$$

$$\text{then: } Z_P = \frac{n_1^2 I^2 Z_1 + n_2^2 I^2 Z_2 + n_3^2 I^2 Z_3}{n_1 + n_2 + n_3}$$

Therefore, the generalized expression can be represented with the following equation:

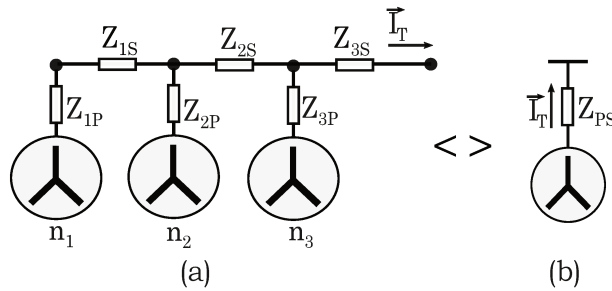
$$Z_P = \frac{\sum_{m=1}^n n_m^2 Z_m}{(\sum_{m=1}^n n_m)^2} \quad (\text{B.4})$$

Where, Z_m represents the equivalent impedance of the individual WTs group.

B.3 Third Step: *Connection to the Low-Voltage Side of the Main Transformer*

Procedure to determine the equivalent impedance of a combination of several feeders in topology in series connected to the low-voltage (LV) side of the main transformer, as shown in Fig. B.4(a). For this configuration, is made the following assumptions:

- All WTs produce identical output current (magnitude and angle).
- There impedances between circuits inter-connected in series, as Z_{1S} , Z_{2S} and Z_{3S} .
- Each group of WTs has series impedance Z_{1P} , Z_{2P} , Z_{3P} .
- There is a unique impedance for each branch and is connected to a group of WTs.
- Each trunk circuit consists of n_1 , n_2 and n_3 WTs respectively



The voltage drop across each impedance, can be expressed by the following equations::

$$\begin{aligned}\Delta \overrightarrow{V_{Z_{1P}}} &= \overrightarrow{I_1} Z_{1P} = n_1 \overrightarrow{I} Z_{1P} & \Delta \overrightarrow{V_{Z_{1S}}} &= \overrightarrow{I_1} Z_{1S} = n_1 \overrightarrow{I} Z_{1S} \\ \Delta \overrightarrow{V_{Z_{2P}}} &= \overrightarrow{I_2} Z_{2P} = n_2 \overrightarrow{I} Z_{2P} & \Delta \overrightarrow{V_{Z_{2S}}} &= (\overrightarrow{I_1} + \overrightarrow{I_2}) Z_{2S} = (n_1 \overrightarrow{I} + n_2 \overrightarrow{I}) Z_{2S} \\ \Delta \overrightarrow{V_{Z_{3P}}} &= \overrightarrow{I_3} Z_{3P} = n_3 \overrightarrow{I} Z_{3P} & \Delta \overrightarrow{V_{Z_{3S}}} &= (\overrightarrow{I_1} + \overrightarrow{I_2} + \overrightarrow{I_3}) Z_{3S} = (n_1 \overrightarrow{I} + n_2 \overrightarrow{I} + n_3 \overrightarrow{I}) Z_{3S}\end{aligned}$$

Based on losses across each impedance, these loss can be computed as:

$$\begin{aligned}S_{Z_{1P}}^{\text{Loss}} &= \Delta \overrightarrow{V_{Z_{1P}}} \overrightarrow{I_1}^* = \overrightarrow{I_1} \overrightarrow{I_1}^* Z_{21} = n_1^2 I^2 Z_{1P} \\ S_{Z_{2P}}^{\text{Loss}} &= \Delta \overrightarrow{V_{Z_{2P}}} \overrightarrow{I_2}^* = \overrightarrow{I_2} \overrightarrow{I_2}^* Z_{22} = n_2^2 I^2 Z_{2P} \\ S_{Z_{3P}}^{\text{Loss}} &= \Delta \overrightarrow{V_{Z_{3P}}} \overrightarrow{I_3}^* = \overrightarrow{I_3} \overrightarrow{I_3}^* Z_{23} = n_3^2 I^2 Z_{3P} \\ S_{Z_{1S}}^{\text{Loss}} &= \Delta \overrightarrow{V_{Z_{1S}}} \overrightarrow{I_1}^* = n_1^2 I^2 Z_{1S} \\ S_{Z_{2S}}^{\text{Loss}} &= \Delta \overrightarrow{V_{Z_{2S}}} (\overrightarrow{I_1} + \overrightarrow{I_2})^* = (n_1 + n_2)^2 I^2 Z_{2S} \\ S_{Z_{3S}}^{\text{Loss}} &= \Delta \overrightarrow{V_{Z_{3S}}} (\overrightarrow{I_1} + \overrightarrow{I_2} + \overrightarrow{I_3})^* = (n_1 + n_2 + n_3)^2 I^2 Z_{3S}\end{aligned}$$

From the Fig. B.4(b), the total loss is $S_{ZT}^{\text{Loss}} = I_T^2 Z_T$, this being equal to the sum of the apparent power losses of impedance in a series-parallel circuit. Then, by substitution, the following expression is obtained:

$$\begin{aligned}I_T^2 Z_T &= I^2 \left[(n_1^2 Z_{1P} + n_2^2 Z_{2P} + n_3^2 Z_{3P}) + (n_1^2 Z_{1S} + (n_1 + n_2)^2 Z_{2S} + (n_1 + n_2 + n_3)^2 Z_{3S}) \right] \\ Z_T &= \frac{[(n_1^2 Z_{1P} + n_2^2 Z_{2P} + n_3^2 Z_{3P}) + (n_1^2 Z_{1S} + (n_1 + n_2)^2 Z_{2S} + (n_1 + n_2 + n_3)^2 Z_{3S})]}{(n_1 + n_2 + n_3)^2}\end{aligned}$$

Therefore, the generalized expression can be represented with the following equation:

$$Z_T = \frac{\sum_{i=1}^{np} n_i^2 Z_{iP} + \sum_{i=1}^{ns} \left(\sum_{j=1}^{ns} n_j^2 \right)^2 Z_{iS}}{(\sum_{m=1}^n n_m)^2} \quad (\text{B.5})$$

Where, Z_{iS} and Z_{iP} represents the equivalent impedances in a series-parallel circuit.

B.4 Fourth Step: *Shunt Representation*

Procedure to determine the equivalent of the shunt line capacitance of the collector grid in a WPP, whose equivalent circuit of the branches is shown in Fig. B.5. Since, the nature of the capacitance generates reactive power that is proportional to the square of the voltage across them, and considering that the bus voltage is close to unity under normal conditions, the representation of the line shunt $B_{\text{WPP}}^{\text{shl}}$ can be considered as the sum of all the shunts of the collector grid.

With the assumption presented above, the total shunt capacitance is computed as follows:

$$B_{\text{Total}}^{\text{sh}} = \sum_{i=1}^n B_i^{\text{sh}} \quad (\text{B.6})$$

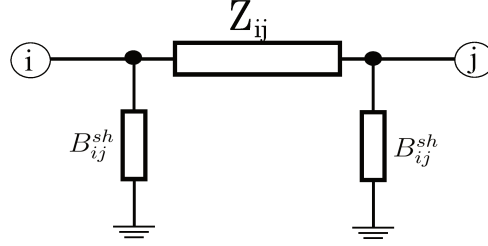


Figure B.5 – Representing the shunt line capacitance of the collector grid within the WPP. [Source: adapted from (Muljadi et al., 2006)]

B.5 Fifth Step: WT Transformer Representation

Procedure to determine the WT transformer equivalent to process the entire wind power plant. The equivalent circuit can be scaled so that the resulting voltage drop across the (leakage) impedances and the power losses are equal to the sum of individual power losses of each WT transformer.

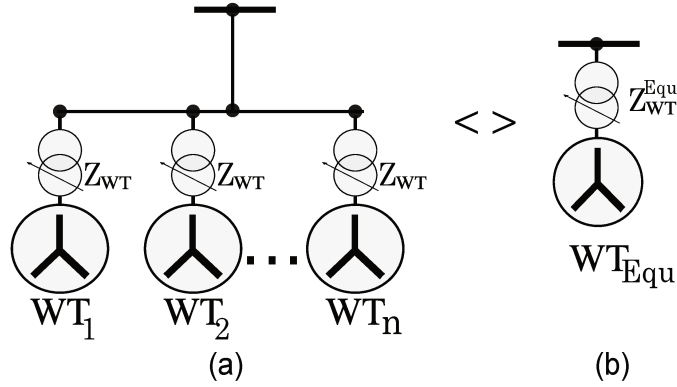


Figure B.6 – a) WT transformer representation within the WPP, b) equivalent representation of circuit (a). [Source: adapted from (Muljadi et al., 2006)]

The equivalent representation for the entire WPP can be computed as the impedance of a single WT transformer divided by the number of the WTs.

$$Z_{WT}^{Equ} = \frac{Z_{WT}}{n} \quad (B.7)$$

C Electrical Data From WPPs

C.1 General Information

Table C.1 – Parameter of the Type-4 WT Feeder

Parameter	WPP System	
	<i>Small WPP</i>	<i>Burbo Bank WPP</i>
\bar{P}^{WT} [MW]	2.0	3.6
V^{nom} [kV]	0.69	0.69
R_{WT} [m Ω]	2.0	1.11
X_{WT} [m Ω]	32.1	17.9
\bar{I}_c [Amp]	2.09	3.77
\bar{V}_c [kV]	0.552	0.552
\underline{V}_c [kV]	0.759	0.759
$R_{\text{WT}}^{\%}$ [%]	5	5
\bar{n}_{WT}	2	2
Ratio	0.69/34.5	0.69/33

Table C.2 – Parameter of Main Transformer

Parameter	WPP System	
	<i>Small WPP</i>	<i>Burbo Bank WPP</i>
Branch [ij]	8-9	26-27
\bar{S}_{ij} [MVA]	16.0	144.0
X_{ij} [%]	8.0	8.0
$R^{\%}$ [%]	5	5
\bar{n}	2	2
Ratio	34.5/138	33/220

C.2 WPP Systems Information

Table C.3 – Branch Data of the small WPP System

Item	Branch [$i-j$]	R_{ij} [Ω]	X_{ij} [Ω]	B_{ij}^{shl} [Ω]	a_{ij}	\bar{S}_{ij} [MVA]
1	1-2	1.45E-02	1.12E-02	2.70E-02	0	10
2	2-3	1.45E-02	1.12E-02	2.70E-02	0	10
3	3-4	1.45E-02	1.12E-02	2.70E-02	0	10
4	4-5	1.45E-02	1.12E-02	2.70E-02	0	10

Table C.3 continued from previous page

Item	Branch $[i-j]$	R_{ij} [Ω]	X_{ij} [Ω]	B_{ij}^{shl} [Ω]	a_{ij}	\bar{S}_{ij} [MVA]
5	5-6	1.45E-02	1.12E-02	2.70E-02	0	12
6	6-7	1.45E-02	1.12E-02	2.70E-02	0	14
7	7-8	2.34E-02	2.12E-02	5.70E-02	0	16

Table C.4 – Branch Data of Burbo Bank WPP System

Item	Branch $[i-j]$	R_{ij} [Ω]	X_{ij} [Ω]	B_{ij}^{shl} [Ω]	a_{ij}	\bar{S}_{ij} [MVA]
1	1-2	1.42E-02	1.09E-02	2.64E-03	0	23.4
2	2-3	1.42E-02	1.09E-02	2.64E-03	0	23.4
3	3-4	1.42E-02	1.09E-02	2.64E-03	0	23.4
4	4-5	1.42E-02	1.09E-02	2.64E-03	0	23.4
5	5-6	1.42E-02	1.09E-02	2.64E-03	0	27.0
6	6-7	1.42E-02	1.09E-02	2.64E-03	0	30.6
7	7-8	1.42E-02	1.09E-02	2.64E-03	0	30.6
8	9-10	1.42E-02	1.09E-02	2.64E-03	0	23.4
9	10-11	1.42E-02	1.09E-02	2.64E-03	0	23.4
10	11-12	1.42E-02	1.09E-02	2.64E-03	0	23.4
11	12-13	1.42E-02	1.09E-02	2.64E-03	0	23.4
12	13-14	1.42E-02	1.09E-02	2.64E-03	0	27.0
13	14-15	1.42E-02	1.09E-02	2.64E-03	0	30.6
14	15-16	1.42E-02	1.09E-02	2.64E-03	0	30.6
15	17-18	1.42E-02	1.09E-02	2.64E-03	0	23.4
16	18-19	1.42E-02	1.09E-02	2.64E-03	0	23.4
17	19-20	1.42E-02	1.09E-02	2.64E-03	0	23.4
18	20-21	1.42E-02	1.09E-02	2.64E-03	0	23.4
19	21-22	1.42E-02	1.09E-02	2.64E-03	0	27.0
20	22-23	1.42E-02	1.09E-02	2.64E-03	0	30.6
21	23-24	1.42E-02	1.09E-02	2.64E-03	0	30.6
22	24-25	1.42E-02	1.09E-02	2.64E-03	0	23.4
23	6-26	2.29E-02	2.07E-02	5.56E-03	0	37.8
24	16-26	2.29E-02	2.07E-02	5.56E-03	0	37.8
25	24-26	2.29E-02	2.07E-02	5.56E-03	0	45.0

D Taylor polynomials

Taylor polynomials (MICHAEL, 1998) are denoted by (D.1):

$$\mathbf{f}(x) = \sum_n^{\infty} \frac{\mathbf{f}^n(a)(x-a)^n}{n!} \quad (\text{D.1})$$

where n is a polynomial order, $n!$ denotes the factorial of n , and $\mathbf{f}^n(a)$ denotes the n^{th} derivative of \mathbf{f} evaluated at point a . Since functions (3.2)–(3.11) must be linearized with respect to the variable $V_{\text{LV}}^{\text{sqr}}$, which is limited by the interval of \bar{V} and \underline{V} in (4.8) being close to the unit, then the function (D.1) is evaluated with $a = 1.0$. In addition, these terms are divided by the term $n!$. Second order terms and onward are disregarded. Thus, the Taylor polynomials of (3.2)–(3.11) are represented by the functions (D.2)–(D.5).

$$\underline{h}_{\gamma^{\text{WT}}}^I(V_{\text{LV}}^{\text{sqr}}) = (\underline{Q}_{\gamma^{\text{WT}}}^I(1, \gamma^{\text{WT}}) - \underline{Q}_{\gamma^{\text{WT}}}^{\prime I}(1, \gamma^{\text{WT}})) + \underline{Q}_{\gamma^{\text{WT}}}^{\prime I}(1, \gamma^{\text{WT}})V_{\text{LV}}^{\text{sqr}} \quad (\text{D.2})$$

$$\bar{h}_{\gamma^{\text{WT}}}^I(V_{\text{LV}}^{\text{sqr}}) = (\bar{Q}_{\gamma^{\text{WT}}}^I(1, \gamma^{\text{WT}}) - \bar{Q}_{\gamma^{\text{WT}}}^{\prime I}(1, \gamma^{\text{WT}})) + \bar{Q}_{\gamma^{\text{WT}}}^{\prime I}(1, \gamma^{\text{WT}})V_{\text{LV}}^{\text{sqr}} \quad (\text{D.3})$$

$$\underline{h}_{\gamma^{\text{WT}}}^V(V_{\text{LV}}^{\text{sqr}}) = (\underline{Q}_{\gamma^{\text{WT}}}^V(1, \gamma^{\text{WT}}) - \underline{Q}_{\gamma^{\text{WT}}}^{\prime V}(1, \gamma^{\text{WT}})) + \underline{Q}_{\gamma^{\text{WT}}}^{\prime V}(1, \gamma^{\text{WT}})V_{\text{LV}}^{\text{sqr}} \quad (\text{D.4})$$

$$\bar{h}_{\gamma^{\text{WT}}}^V(V_{\text{LV}}^{\text{sqr}}) = (\bar{Q}_{\gamma^{\text{WT}}}^V(1, \gamma^{\text{WT}}) - \bar{Q}_{\gamma^{\text{WT}}}^{\prime V}(1, \gamma^{\text{WT}})) + \bar{Q}_{\gamma^{\text{WT}}}^{\prime V}(1, \gamma^{\text{WT}})V_{\text{LV}}^{\text{sqr}} \quad (\text{D.5})$$

Results in Table D.1 show the coefficients of the degree one polynomial of the functions: $\bar{h}_{\gamma^{\text{WT}}}^I$, $\underline{h}_{\gamma^{\text{WT}}}^I$, $\bar{h}_{\gamma^{\text{WT}}}^V$ and $\underline{h}_{\gamma^{\text{WT}}}^V$. For $P^{\text{WT}} = \{0.0, 0.1, \dots, 0.9, 1.0\}$ pu. Where x^0 and x^1 are the coefficients of degree zero and one respectively. Obtaining an average RMSE of 0.22% between the projected areas of the nonlinear equations (3.2)–(3.11) and linear equations (D.2)–(D.5) (see section 4.3.1).

Table D.1 – Coefficients of linear functions calculated using Taylor polynomials.

Item	γ^{WT}	$\bar{h}_{\gamma^{\text{WT}}}^I$		$\underline{h}_{\gamma^{\text{WT}}}^I$		$\bar{h}_{\gamma^{\text{WT}}}^V$		$\underline{h}_{\gamma^{\text{WT}}}^V$		RMSE
		x^0	x^1	x^0	x^1	x^0	x^1	x^0	x^1	
1	0.0	-0.593	-0.658	0.593	0.658	2.799	-4.276	3.854	-3.106	0.0023
2	0.1	-0.587	-0.660	0.587	0.660	2.785	-4.271	3.844	-3.103	0.0024
3	0.2	-0.568	-0.667	0.568	0.667	2.772	-4.266	3.834	-3.099	0.0024
4	0.3	-0.535	-0.680	0.535	0.680	2.758	-4.261	3.825	-3.095	0.0024
5	0.4	-0.487	-0.699	0.487	0.699	2.745	-4.256	3.815	-3.092	0.0022
6	0.5	-0.422	-0.725	0.422	0.725	2.731	-4.251	3.805	-3.088	0.0020
7	0.6	-0.336	-0.762	0.336	0.762	2.718	-4.246	3.795	-3.085	0.0017
8	0.7	-0.223	-0.815	0.223	0.815	2.704	-4.241	3.785	-3.081	0.0013
9	0.8	-0.072	-0.891	0.072	0.891	2.690	-4.236	3.776	-3.077	0.0006
10	0.9	0.140	-1.011	-0.140	1.011	2.677	-4.230	3.766	-3.074	0.0030
11	1.0	0.472	-1.228	-0.472	1.228	2.663	-4.225	3.756	-3.070	0.0040